

PU/NE-03-04

**NUCLEAR-COUPLED FLOW INSTABILITIES
AND
THEIR EFFECTS ON DRYOUT**

**By
M. Ishii, X. Sun, and S. Kuran**

**2002-2003 Annual Progress Report
submitted to**

**U.S. Department of Energy
Nuclear Engineering Education and Research Program**



June 2003

**PURDUE UNIVERSITY
SCHOOL OF NUCLEAR ENGINEERING**

PURDUE UNIVERSITY
SCHOOL OF NUCLEAR ENGINEERING

NUCLEAR-COUPLED FLOW INSTABILITIES
AND
THEIR EFFECTS ON DRYOUT

By
M. Ishii, X. Sun, and S. Kuran

Purdue University
School of Nuclear Engineering

June 2003

Prepared for
U.S. Department of Energy
Nuclear Engineering Education and Research Program

School of Nuclear Engineering, Purdue University, 400 Central Drive
West Lafayette, IN 47907-2017, USA

ACKNOWLEDGMENTS

The research project is supported by U.S. Department of Energy, Nuclear Engineering Education Research Program with grant number 01ID14120.

TABLE OF CONTENTS

	Page
LIST OF TABLES	vii
LIST OF FIGURES	viii
NOMENCLATURE	x
EXECUTIVE SUMMARY	xiii
1. INTRODUCTION	1-1
2. STATE-OF-THE-ART REVIEW	2-1
2.1 Classification of Flow Instabilities	2-1
2.1.1 Static Instabilities	2-2
2.1.2 Dynamic Instabilities	2-5
2.2 Stability Problem in Current BWRs	2-9
2.3 Stability Problem in Natural Circulation BWRs	2-17
I Analytical Modeling	2-19
3. FLOW FIELD FORMULATION	3-1
3.1 Description of the Flow Systems	3-2
3.2 One Dimensional Drift Flux Model	3-5
3.2.1 Field Equations	3-7
3.2.2 Constitutive Equations for Drift Flux Parameters	3-10
3.3 Subcooled Boiling	3-11
3.3.1 Departure Enthalpy	3-12
3.3.2 Model for Volumetric Vapor Generation Rate	3-13
3.4 Governing Equations	3-16
3.4.1 Single Phase Flow	3-17
3.4.2 Two-Phase Mixture Flow	3-17

3.5	Dimensional Analysis and Scaling	3-19
3.5.1	Dimensionless Governing Equations	3-20
3.5.2	Dimensionless Numbers	3-23
4.	FUEL HEAT CONDUCTION MODELING	4-1
4.1	Heat Conduction in Fuel Element	4-3
4.2	Steady-state Temperature Distribution and Thermal Resistances . . .	4-7
4.2.1	Pellet Region	4-8
4.2.2	Gap and Cladding Regions	4-11
4.2.3	Convective Resistance of the Coolant	4-13
4.3	Simplified Models for Fuel Heat Conduction	4-15
4.3.1	Double-Node Lumped Model	4-16
4.3.2	Single-Node Lumped Model	4-17
4.4	Fuel Heat Conduction Time Constant	4-18
4.5	Dimensional Analysis and Transfer Functions for Fuel Heat Conduction	4-20
4.5.1	Scaling Variables and Dimensionless Conduction Equations . .	4-20
4.5.2	Frequency Domain Analysis: Transfer Functions	4-24
4.5.2.1	Single Phase Flow	4-26
4.5.2.2	Two-phase Flow	4-27
4.6	RC-circuit Analogy	4-28
5.	NEUTRON KINETICS MODELING	5-1
5.1	Introduction	5-1
5.2	Point Kinetic Model	5-3
5.3	Void Reactivity Coefficient for SBWR	5-6
5.4	Calculation of Reactivities for Point Kinetic Model	5-8
5.4.1	Feedback Reactivities	5-11
6.	FLOW EXCURSION MODELING VIA SUBCOOLED BOILING	6-1
6.1	Stability Criterion for Flow Excursion	6-1
6.2	Characteristic Equation for Flow Excursion	6-2
6.2.1	Single-Phase Heated Section	6-3

6.2.2	Two-Phase Mixture Heated Section	6-3
6.2.3	Two-Phase Mixture Unheated Section	6-5
6.3	Pressure Drop vs. Flow Rate Curve Characteristics	6-7
6.3.1	Effect of Heat Flux	6-8
6.3.2	Effect of Inlet Subcooling	6-10
6.3.3	Effect of Localized Flow Resistances	6-10
6.3.4	Effect of Channel Orientation	6-13
6.4	Stability Maps for Flow Excursion	6-13
6.4.1	Subcooling Number versus Zuber Number Plane	6-14
6.4.2	Zuber Number versus Inverse of Froude Number	6-15
6.5	Forced Circulation versus Natural Circulation	6-19
7.	NONLINEAR ANALYSIS OF NUCLEAR-COUPLED DWO	7-1
7.1	Galarkin Weighted Residual Method	7-1
7.2	Flow Field Formulation	7-3
7.2.1	Boiling Boundary Dynamics	7-4
7.2.2	Mixture Density and Velocity in Two-phase Mixture Regions	7-5
7.2.3	Flow Dynamics	7-8
7.3	Fuel Heat Conduction Equations	7-8
7.4	Neutron Kinetics	7-9
7.5	ODE Set for the Nonlinear Dynamics	7-10

II Experimental Study 7-13

8.	EXPERIMENTAL FACILITY	8-1
8.1	Experimental Loop Layout	8-1
8.2	Test Section	8-4
8.3	Experimental Loop Instrumentation	8-7
8.3.1	Impedance Void Meter	8-8
8.3.1.1	Impedance Probe Design	8-8
8.3.1.2	Theoretical Basis	8-11

8.3.2	Thermistor Probe	8-13
8.3.3	Magnetic Flowmeter	8-13
8.3.4	Differential Pressure Transducer	8-15
8.3.5	Absolute Pressure Transducer	8-15
8.3.6	Thermocouples	8-16
8.4	Data Acquisition System	8-16
9.	EXPERIMENTAL RESULTS	9-1
9.1	Air-Water Tests	9-1
9.2	Flow Instability Tests	9-4
9.2.1	Experimental Procedure	9-4
9.3	Void-Reactivity Feedback Simulation	9-14
10.	CONCLUSIONS	10-1
	LIST OF REFERENCES	11-1
A.	SINGLE AND TWO-PHASE EULER NUMBERS	A-1
B.	BOILING BOUNDARY DYNAMICS EQUATIONS	B-1
C.	PRESSURE DROP COMPONENTS	C-1

LIST OF TABLES

Table		Page
2.1	Classification of Flow Instabilities	2-10
3.1	Scaling Variables in Dimensionless Analysis	3-20
4.1	Coefficient of Eq. (4.27) for Different Correlations	4-14
6.1	Typical BWR Fuel Bundle Geometrical Data	6-14
6.2	SBWR Geometrical Data	6-17
9.1	Test Conditions for the Flow Excursion	9-5
9.2	Test Conditions for Flow Oscillations at High Inlet Temperature . . .	9-11

LIST OF FIGURES

Figure	Page
2.1 Physical Processes Involved in BWR Stability	2-14
3.1 Typical Geometrical Arrangement for a Forced Circulation System . .	3-3
3.2 Typical Flow Arrangement for a Natural Circulation System	3-4
3.3 Typical Void Development and Volumetric Vapor Generation Rate in a Heated Channel including the Subcooled Boiling Region	3-15
4.1 Typical BWR Fuel Element	4-4
4.2 Heat Conduction Network for the Fuel Element based on Averaged Temperatures	4-8
4.3 Thermal Conductivity of UO ₂ Pellet	4-9
4.4 Thermal Conductivity of Zr ₂ Cladding	4-12
4.5 High Pass and Low Pass RC Circuits	4-29
5.1 Change in Bundle Reactivity with the Void Fraction at Different Pres- sures	5-7
5.2 Void-Reactivity Coefficient as a Function of the Void Fraction	5-9
5.3 Average Void-Reactivity Coefficient over a $\alpha = 0$ to 0.3 as a Function of Pressure	5-10
6.1 The Pressure Drop versus Flow Rate Curve	6-8
6.2 Pressure Drop Components for a Typical BWR Fuel Bundle	6-9
6.3 Effect of Heat Flux on $\Delta P-\dot{m}$ Curve	6-10
6.4 Effect of Inlet Subcooling on $\Delta P-\dot{m}$ Curve	6-11
6.5 Effect of Localized Flow Resistances on $\Delta P-\dot{m}$ Curve	6-12
6.6 Effect of Gravity Field on $\Delta P-\dot{m}$ Curve	6-13
6.7 Stability on Subcooling Number –Zuber Number	6-15
6.8 Effect of Subcooled Boiling on Flow Excursion Boundary	6-16

6.9	Stability on the Zuber Number – the Inverse of the Froude Number . . .	6-17
6.10	Stability on the Zuber Number – the Inverse of the Froude Number for Different Values of the Subcooling Number	6-18
6.11	Flow Excursion Boundary in BWR and SBWR	6-19
7.1	Neutron Flux Oscillations inside the Linearly Unstable Region	7-11
7.2	Limit-cycle Oscillation in a Phase Plane	7-12
8.1	Experimental Loop Layout	8-2
8.2	Test Section Layout	8-5
8.3	Impedance Probe with Ring Type Electrodes	8-10
8.4	Thermistor Probe	8-14
9.1	Typical Impedance Signal for Different Flow Regimes	9-2
9.2	Cross-Calibration Curve for the Void Measurement with the DP Cell and the Impedance Probe	9-3
9.3	Comparison of the Experimental Data and the Model Prediction	9-6
9.4	Transient Path during the Flow Excursion observed during the Tests . .	9-7
9.5	Transient in the Channel Inlet Velocity during the Flow Excursion . . .	9-8
9.6	Transient in the Channel Void Fraction during the Flow Excursion . . .	9-9
9.7	Constant Amplitude Oscillations following the Flow Excursion	9-10
9.8	Self-sustained Flow Oscillations at Test No:14	9-12
9.9	Change in the Oscillation Magnitude with the Heater Power	9-13
9.10	Data Flow for Void-reactivity Simulation Experiment	9-15

NOMENCLATURE

A	Area [m ²]
a	Diffusivity [m ² /s]
c_p	Specific Heat [J/(kg K)]
C_o	Distribution Parameter
C_g	Coefficient for Subcooled Boiling defined by Eq. (3.33)
C_m	Multiplier for Two-phase Frictional Pressure Drop
$f_{1\phi}$	Single Phase Friction Factor
g	Gravitational Acceleration [m/s ²]
D	Diameter [m]
h	Heat Transfer Coefficient [W/m ² K]
K	Flow Loss Coefficient
K_α	Void Reactivity Coefficient [\$/% Void]
K_D	Doppler Coefficient [\$/K]
k	Thermal Conductivity [W/(mK)]
m	Wall Superheat Exponent in Two-Phase Flow Heat Transfer Coefficient [W/(m ² K)]
n	Neutron Amplitude Function
N_{Fo}	Fourier Number
N_{Bi}	Biot Number
N_{Re}	Reynold Number
N_{Pr}	Prandtl Number
N_{Zu}	Zuber Number
N_ρ	Density Ratio Number
N_f	Friction Number

N_{sub}	Subcooling Number
P	Pressure [Pa]
r	Radial Coordinate [m]
\dot{Q}	Total Reactor Power [W]
Q'	Linear Heat Rate [W/m]
Q'''	Volumetric Heat Generation [W/m ³]
T	Temperature [K]
U	Overall Heat Conductance [W/(mK)]
z	Axial Coordinate [m]

Greek Letter

α	Void Fraction
β	Delayed Neutron Fraction
Γ	Volumetric Vapor Generation Rate [kg/(m ³ s)]
γ	Fraction Heat directly deposited into the coolant
Δ	Difference Operator (i.e. Pressure Drop)
δ	Small Perturbation around Steady State
ξ_h	Heated Perimeter
ξ	Reduced Precursor Concentration [s]
Φ	Radial Shape Function in the Fuel Pellet
λ	Nonboiling Height [m], Precursor Decay Constant [s ⁻¹]
Ω	Reaction Frequency [1/s]
ω	Frequency [1/s]
ν	Kinematic Viscosity [m ² /s]
μ	Viscosity [N.s/m ²]
σ	Surface Tension [N/m]
ρ	Density [kg/m ³], Reactivity[\$]
θ	Dimensionless Temperature

θ_1	Boiling Length [m]]
v	Velocity [m/s]

Subscript

1ϕ	Single Phase
2ϕ	Two-Phase
c	Cladding
g	GasPhase, Gap Region
h	Heated Section
in	Inlet
e	Exit, Equivalent
ext	External
fe	Fuel Element
m	Mixture
sub	Subcooling
s	Saturation
o	Steady State
p	Fuel Pellet
uh	Unheated Section
∞	Convective Side

Symbols

$\langle \rangle$	Area Averaging Operator
$\langle \langle \rangle \rangle$	Power Profile-weighted Area Averaging Operator
$(,)$	Inner Product Operator

EXECUTIVE SUMMARY

Nuclear-coupled flow/power oscillations are one of the major operational problems in current operating Boiling Water Reactors (BWRs). After the instability events in LaSalle-II in U.S. and some other European BWRs such as Coarsa plant, a series of experimental and analytical research efforts have been initiated to investigate the nuclear-coupled Density Wave Oscillations (DWOs). However, the stability is still a major issue in BWRs especially in next generation designs such as natural circulation BWRs and high conversion BWRs. The problem in natural circulation BWRs such as Simplified Boiling Water Reactor (SBWR) is more pronounced at low pressure, low flow conditions during the startup. In view of the lack of sufficient experimental data aforementioned operating conditions, there is still further research need for low pressure, low flow instabilities. The problem of instability is further complicated due to existence of void-reactivity and Doppler reactivity feedbacks which creates the link between flow and neutron fields. Since there is no reactor data for the nuclear-coupled flow/power oscillations at low pressure, the void-reactivity simulation in a well-scaled experimental facility is indispensable. The present research in this project aims to investigate the nuclear-coupled instabilities in BWRs both experimentally and analytically.

As the second-year tasks of the project, the followings have been accomplished:

1. A detailed literature review has been performed to understand the recent activities and examine the available database. The problem is addressed for both conventional BWRs and next generation BWRs such as natural circulation BWRs. It has been concluded that the available database is insufficient to address the problem of nuclear-coupled flow instabilities. Moreover, the void-reactivity simulation experiments are rather new in the experimental two-phase

flow field. The solid strategy for simulating the void-reactivity feedback is still under development.

2. The analytical modeling for the flow instabilities in BWRs has been performed based on physical processes governing the system. In view of the physical leading mechanisms of the instabilities, the modeling strategy has been concentrated into the following three processes:

- (a) Flow Field
- (b) Fuel Heat Conduction
- (c) Neutron Kinetics

One-dimensional drift-flux formulation has been used to model the flow field. In order to keep the problem formulation general, three regions in a two-phase flow system are considered:

- (a) Single Phase Heated Region
- (b) Two-phase Mixture Heated Region
- (c) Two-phase Mixture Unheated Region

By means of one-dimensional drift-flux formulation and subcooled boiling, mechanical and thermal non-equilibrium between liquid and gas phases are considered. The dimensional analysis for the flow field formulation provides the dimensionless groups that should be conserved in an experimental facility to simulate and investigate the instabilities.

A detailed analysis has been performed to investigate the fuel heat conduction process. The heat conduction creates the link between heat generation inside the fuel and heat transferred to the coolant. The amount of time-lag inherent to the heat conduction is one of the important parameters in the nuclear-coupled instabilities. The analysis on a typical BWR fuel pin and an electrical heater used in an experimental facility resulted in strategy to simulate the wall heat

flux response. The detailed dimensional analysis provides the important dimensionless groups for the fuel heat conduction considering the effect of flux depression factor, temperature-dependent thermal conductivity of the fuel.

For the neutron kinetics, the point kinetic model has been used to determine the time rate of change in the volumetric heat generation inside the fuel. The power level which is a strong function of the void fraction in the flow channel can be determined by solving the neutron kinetics model. Void-reactivity coefficient is another important parameter for the nuclear-coupled instabilities. For a typical BWR fuel bundle, the void-reactivity coefficient as a function of the void fraction and the operating pressure has been generated by means of a two-dimensional neutron transport code.

3. A simple nonlinear dynamics model has been derived for a generic polynomial approximation for simulating the single phase enthalpy and two-phase mixture density waves based on Galarkin Weighted Residual Method. It has been shown that limit-cycle oscillations are observed inside the unstable region which is predicted by linear frequency domain tools.
4. The experimental facility based on the scaling determined from flow-field formulation has been designed and built as a part of first-year tasks. The heater power-control program has been developed to adjust the heater power based on the instantaneous area-averaged void-fraction measurements at three axial locations along the test section simulating a typical BWR channel. The program incorporates the void-reactivity feedback calculated from the measured void-fractions and artificial time delay determined from the fuel heat conduction process scaling to simulate wall heat flux response in a typical BWR fuel pin.

1. INTRODUCTION

It has been known that two-phase flow systems are vulnerable to different types of instabilities. Existence of two different density materials (liquid-steam) alters the transport and other fluid-flow related properties such as disturbance propagation, pressure drop. In addition, nucleation phenomenon and different flow regimes with different characteristics yield complex dynamic and static behavior.

Flow instabilities are undesirable in any engineering equipment since unstable flow behavior may yield forced mechanical vibrations, system control problems, and premature burnout of the heating element. In boiling water reactor (BWR) systems, the issue is more important and causes severe operational problems when flow oscillations are coupled to power oscillations due to several neutronic feedbacks such as the void reactivity and the fuel temperature-reactivity (Doppler) feedback.

The instabilities at low pressure and low flow conditions are important for the next generation BWRs using natural circulation for both normal and accidental core cooling. Especially, the startup transient in these reactors is vulnerable to different types of flow instabilities. In addition to the complexity of the problem at aforementioned conditions, the existence of nuclear coupling via reactivity feedbacks such as the void-reactivity and Doppler reactivity further complicates the problem. At low pressure conditions, different forms of power/flow oscillations can be observed. The detailed review on available database has been shown that there is still a need to investigate the nuclear-coupled instabilities in both conventional and next generation BWRs. Especially, the lack of the reactor data regarding the low pressure, flow flow nuclear-coupled instabilities necessitates the void-reactivity feedback simulation in a well-scaled experimental facility to investigate the problem and generate a reliable database for benchmarking the available analytical models.

In this study, the fundamentals of the nuclear-coupled flow instabilities are discussed along with the scaling of the experimental facility that has been built to simulate the instabilities. The report is divided into two main parts. In the first part, the analytical modeling strategy is discussed by emphasizing the important physical processes. Three important physical processes are taken into account:

1. Flow Field
2. Fuel Heat Conduction
3. Neutron Kinetics

Chapter 3 discusses the general formulation of the flow field based on one-dimensional drift-flux model. The flow field is analyzed by considering the following three separate regions:

1. Single Phase Heated Section
2. Two-phase Heated Section
3. Two-phase Unheated Section

The scaling analysis is performed to derive the dimensionless groups that scale the fluid flow in a general two-phase flow system composing of aforementioned sections. In the formulation, the subcooled boiling as a thermal non-equilibrium is considered by means of Saha-Zuber [1] departure enthalpy model.

Heat conduction in a typical BWR fuel pin plays an important role in the instabilities. The conduction inside the fuel rod bridges the heat generation and heat transferred to coolant. The process generally is accompanied with a certain time-lag, the amount of the delay and the associated physics need to be understood to simulate the void-reactivity in the experimental facility. The detailed analysis of the fuel heat conduction is discussed in Chapter 4. The dimensional analysis is carried out to determine the governing dimensionless groups for the void-reactivity simulation.

In Chapter 5, the neutron kinetics modeling is discussed. The point kinetic model for describing the time rate of change in neutron flux is introduced. The methodology used to generate the void-reactivity coefficient which is required for the void-reactivity feedback simulation is given.

The flow field formulation including the subcooled boiling and one-dimensional drift flux model is applied to investigate the flow excursion phenomenon which is one of the important static instabilities. The importance of subcooled boiling is emphasized to determine the stability boundary for the flow excursion in both forced and natural circulation systems.

Chapter 7 describes a simple analytical model which is derived to investigate the nonlinear aspects of the nuclear-coupled density wave oscillations (DWOs). The field equations describing the flow field, fuel heat conduction, and neutron kinetics are written as a system of nonlinear ordinary differential equations which can be integrated in time to determine the transient response of the system.

In the second part of the report, the experimental study related to the simulation of the void-reactivity feedback is discussed. The detailed description of the experimental facility is introduced along with the instrumentation in Chapter 8. The experimental data regarding the flow excursion and DWO without nuclear-coupling is presented in Chapter 9. In this chapter, the detailed strategy for simulating the void-reactivity feedback and wall heat flux response is discussed based on the scaling study performed in the first part of the report.

In the following chapter, the state-of-the-art review on BWR instabilities is presented.

2. STATE-OF-THE-ART REVIEW

Flow instabilities are most common operating problem in two-phase flow systems such as conventional boilers, steam generator and nuclear reactors. They are undesirable since they can degrade the system performance and cause serious control problems. Several experimental and analytical studies had been performed over past decades. Different analytical models had been proposed for different types of flow instabilities. However, there are still issues to be resolved for a general stability problem. Especially, flow instabilities that may occur at low-pressure and low-flow conditions need to be clearly understood based on experimental data and reliable analytical models, since under these conditions, the instabilities can be most commonly encountered.

In this chapter, the state-of-the-art of the stability issue in two-phase flow systems is highlighted by emphasizing the importance of the problem in BWR systems. Because of the strong coupling between the flow-temperature or void-fraction field and neutron field, instabilities in BWR systems accompany with oscillation in both flow and power. The void-reactivity is the most significant component of the feedback loop and it creates the additional link between the oscillations in the flow and power.

2.1 Classification of Flow Instabilities

Identification and classification of physical mechanisms that lead to unstable conditions in two-phase flow systems are important not only for proper design but also for taking the necessary precautions for mitigating the instabilities. The flow instabilities, in general, cause forced mechanical vibration on system components, thermal oscillations, control problems and may even lead to the premature burnout

of the heated surface. Combining all these effects, proper operation of the equipment is difficult once unstable behavior occurs.

The instability issue is more complicated in BWRs. Because of strong coupling of thermal-hydraulics and neutron field which are interrelated by means of neutronic feedbacks such as void-reactivity and fuel temperature or Doppler feedback, coupled flow-power oscillations can be potentially encountered in these reactors.

Instabilities in general are classified into two main categories, namely static and dynamic instabilities. There are many review studies on instabilities [2, 3, 4]. The classification based on physical mechanisms is more appropriate since each type has a similar methodology for analysis. Before proceeding further on different types of flow instabilities, it is worthwhile to introduce some definitions:

Steady Flow: Flow is said to be steady if the system parameters are functions of spatial variables only. However, normally flow shows some small fluctuations due to turbulent two-phase flow or nucleation process.

Stable Flow: Flow is said to be stable if, when it is momentarily disturbed, its new operating conditions tend asymptotically towards the initial ones.

2.1.1 Static Instabilities

Static instabilities are governed by the steady-state characteristic of the system. Pressure drop characteristics of a flow channel, nucleation properties, and flow regime transitions play important roles on characterization of these type of flow instabilities. The important static flow instabilities can be listed as follows:

1. Flow Excursion (Ledinegg Instability)
2. Critical Heat Flux (CHF) or Boiling Crisis
3. Flow Regime Transition Instability
4. Geysering, Chugging, and Vapor Burst

Among these instabilities, the flow excursion is the most important flow instability of significant consequences. Ledinegg [5] first identified and analyzed the problem. The instability is also called Ledinegg Instability. The flow excursion involves a sudden change in the flow rate, normally from high flow to a very low flow. It occurs when the slope of the channel demand pressure drop vs flow rate curve becomes algebraically smaller than the slope of the loop supply pressure drop vs flow rate curve. The criterion for this instability can be written as

$$\frac{\partial \Delta P_{int}}{\partial v_{in}} < \frac{\partial \Delta P_{ext}}{\partial v_{in}} \quad (2.1)$$

where ΔP_{int} is the steady-state pressure drop along the flow channel, which is the internal characteristic of the channel, and ΔP_{ext} is the supply pressure drop which drives the flow. The channel inlet velocity is denoted by v_{in} .

This behavior requires that the channel characteristics exhibit a region where the pressure drop decreases with increasing flow. In two-phase flow, the friction and convective acceleration terms in the total pressure drop may increase with decreasing flow. For most of the systems of interest, the supply pressure drop for a channel is nearly constant. This applied to a parallel channel system and channel accompanied with a large bypass. Maulbetsch and Griffith [6] tested a low-pressure, subcooled boiling system for flow excursion by paralleling the heated channel with a large bypass. They observed that CHF occurs well below the values calculated by using conventional CHF correlations. They also concluded that excursions leading to CHF were observed near the minima in the pressure drop versus mass flow rate curve.

CHF is another important instability associated with the change in heat transfer mechanism and sudden rise in wall temperature but it is not a flow instability. However, flow instabilities are one of the phenomena that may lead to CHF. Flow excursion induced CHF has been analyzed and its implication in fast reactor safety has been discussed [7]. Mathisen [8] observed that boiling crisis occurred simultaneously with flow oscillations in a boiling water channel at pressure higher than 6 MPa.

The third static instability is the flow regime transition instability. It is a relaxation instability caused by different pressure drop characteristics of different flow patterns. As it is well known that bubbly and churn-turbulent flows have a larger pressure drop compared to annular and annular-mist flow. One may consider a two-phase flow channel subjected to a constant pressure drop boundary condition and assume that churn-turbulent flow regime exists at the channel exit, and the flow at the channel inlet is decreased for a while. At the reduced flow condition, annular flow regime occurs at the channel exit where pressure drop is smaller. Since the imposed pressure drop is constant, it causes the flow to accelerate. At the new flow conditions, annular flow regime cannot be sustained. The cyclic flow regime pattern change results in flow oscillations. Even though the instability is oscillatory in nature, its basic characteristics lie on the steady state pressure drop of different flow patterns. Jeglic and Grace [9] observed cyclic flow pattern transition with oscillatory behavior, however it is not clear whether the flow pattern transition is the cause or the consequence of density wave propagation.

Geysering, chugging and vapor burst are important static flow instabilities, which may occur in natural circulation boiling water reactors and some liquid metal cooled reactors. Especially, geysering is a phenomenon which may be encountered during the startup of Simplified Boiling Water Reactor (SBWR). Geysering has been observed in a variety of closed end, vertical columns of liquid, which are heated at the base [10, 11]. When the heat flux is high and flow is low, boiling is initiated at the base. In low-pressure systems, this results in a suddenly increased bubble size due to reduction in hydrostatic head, and usually an expulsion of vapor from the channel. The liquid then returns and subcooled non-boiling conditions are restored, and cycle starts over again. The cyclic void appearance and disappearance may lead to an operational problem during the startup of natural circulation BWRs at very low pressure. This phenomenon depends on the nucleation characteristics of the channel wall, system geometry and operational conditions.

2.1.2 Dynamic Instabilities

Most of the practical flow instability problems are dynamic in nature. The process is governed by inertia and feedback effects and by the whole system response rather than by the local thermal-hydraulic conditions. Therefore, the transient form of the governing equations for the system of interest should be solved for the analysis.

In the analysis of dynamic flow instabilities, two important aspects should be taken into account:

1. Any disturbance needs some time to propagate and induce other disturbances with a certain time lag.
2. System has several feedback mechanisms.

In the first aspect, the important phenomenon is the wave type by which disturbances are propagated. In two-phase flow systems, the disturbances are mostly propagated by two different waves:

1. Pressure or Acoustic Wave
2. Kinematic Wave or Density (Void) Wave

These two types of waves are always present in the system of consideration. The pressure wave is characterized by sonic speed inside the two-phase mixture. Kinematic waves or density waves are characterized by kinematic wave velocity, which is close to the vapor velocity. Therefore, the kinematic waves have much lower speed than the acoustic waves. Basic characteristics of the dynamic flow instabilities are explained in terms of these waves. Oscillation frequency of the dynamic instabilities is related to the dominant wave velocity in the system and the residence time of the wave. For instance, oscillations governed by the pressure waves have higher frequencies. Important dynamic instabilities can be listed as follows:

- Density Wave Oscillations (DWO)
- Acoustic Oscillations

- Pressure Drop Oscillations
- Thermal Oscillations

Most common dynamic instability encountered in two-phase flow systems is DWO. One may consider a boiling channel with a constant pressure drop boundary condition. A temporary reduction in the inlet flow in a heated channel increases the rate of enthalpy rise, thereby reducing the non-boiling length. In the single phase region, the enthalpy wave is propagated with the liquid velocity, thus there is a time lag due to this propagation. The perturbation is translated to the void or density perturbation in the two-phase region. Since there is time needed for the propagation of the density wave in the two-phase region, time lag appears between the channel inlet flow and the two-phase pressure drop. For certain combinations of geometrical arrangement, operating conditions, and boundary conditions, the perturbations may acquire 180° out-of-phase pressure drop fluctuations at the exit. The perturbations are then transmitted to the inlet flow rate and become self-sustained. In this instability, the phase-shift occurs because of the delay introduced by the propagation of the enthalpy and void or density waves. The period of the oscillations is on the order of the residence time of the coolant inside the channel. These are low-frequency oscillations and the compressibility of the phases is not important parameter in the physical mechanism. This is the most common instability mode in the current operating BWRs and extensive experimental and analytical studies have been carried out to eliminate this instability.

The formulation of the problem by using one-dimensional drift-flux model has been performed by Ishii [12, 13]. The formulation of the problem was general in the sense that it accounts for the dynamics of the flow in single phase heated, two-phase heated and two-phase unheated sections of a flow loop. The formulation neglects the thermodynamic non-equilibrium and accounts for the mechanical non-equilibrium between the phases with a given constitutive relation for the drift velocity. The governing equations are perturbed around the steady state and the characteristic

equation is obtained by integrating the mass, energy, and momentum equations for the single phase and the two-phase regions. The characteristic equation is written in terms of dimensionless numbers that govern the system static and dynamic conditions. These dimensionless numbers are important not only for understanding the physical phenomenon for low frequency oscillations but also for scaling an experimental facility that can be used for the simulation of the flow instabilities and other transients such as LOCAs in the prototype systems. In that study, the dimensionless stability plane has been proposed for presenting stability boundary of a two-phase flow system. The stability plane which has the axes of Zuber Number and Subcooling Number became a standard for the stability map. The comparison with experimental data showed good agreement as far as stability boundary and oscillation frequency are concerned. This study has been extended by Saha [1] by accounting for the thermal non-equilibrium effects between the phases. The stability boundary has been presented on the same plane, and it has been shown that it gives very similar results especially at high subcooling. The detailed discussion of the problem in BWR systems can be found in [14, 15].

In contrast to the low frequency density wave oscillations, acoustic instabilities governed by the propagation of the acoustic waves are high frequency oscillations and the compressibility effects are important. Even though it has little importance in practical nuclear engineering problems, there has been research on these oscillations in relation to the rocket engine stability problems. Several authors [16, 17] have reported that pressure oscillations of relatively high frequency are observed when the systems are operated under high subcooling conditions. As a rule of thumb, the acoustic oscillations need to be considered when a system has Mach number greater than 0.1.

Another important dynamic instability is the pressure drop oscillations. This type of instability is observed in systems which are operated on the negative slope portion of the pressure drop versus flow rate curve and are associated with a compressible volume. This instability is a compound instability which is the result of the

combination of the flow excursion and the density wave oscillations.

The thermal oscillations are associated with the thermal response of the heating wall after dryout as identified by Stenning and Veziroglu [18]. It was suggested that flow could oscillate between film boiling and transition boiling at a given point, thus producing large amplitude temperature oscillations on the channel wall. The thermal oscillations have been found to have periods of approximately 80 sec in their experiments.

The instabilities mentioned here are based on classification of leading physical mechanisms. The boundary conditions introduced in the problem and geometrical arrangement of the system are also important and might yield different oscillation modes. The boundary conditions of the problem can be also important for identifying feedback mechanisms. In pure thermal-hydraulic instabilities, there are two common types of boundary conditions considered:

1. *Hydrodynamic Boundary Conditions* are given as the pressure drop across the channel or the inlet flow rate and pressure. The geometry of the problem is important in determining the suitable boundary conditions. For example, in natural circulation systems, if flow is governed by a constant gravity head, the constant pressure drop boundary condition is applicable. This type of boundary condition is appropriate when a typical single channel is considered with a large number of parallel channels where the average of the majority channels give the stable pressure drop.
2. *Thermal Boundary Conditions* are given at the boiling channel inlet as the inlet subcooling or the heated wall temperature, which is the solution of heat conduction problem in the wall. The inlet subcooling given in the problem might be oscillatory in nature. In general, thermal boundary condition at the channel inlet is the solution of the thermal-hydraulic problem in other part of the system.

The detailed review of the problem can be found in Ref. [2]. Table 2.1 summa-

rizes many instability types encountered in practical engineering applications. However, the instability issue in BWRs requires much more detailed attention because of its complexity. In the following sections, the flow instabilities in BWR systems are highlighted.

2.2 Stability Problem in Current BWRs

As described in the previous sections, two-phase flow systems are vulnerable to different types of flow instabilities either static or dynamic in nature. The problem in BWRs is much more complex because different considerations come into play. First, BWR systems have strong coupling between the thermal-hydraulics and the neutronics via the void reactivity and the fuel temperature feedbacks. The most important feedback is due to the void since the coolant in BWRs also serves as the moderator. Any change in the moderator density via change in the void fraction affects thermal neutron population (via neutron moderation). This changes the heat generation rate inside the fuel and feedbacks to core thermal-hydraulics. The problem in BWRs becomes more complicated since the balance of the plant part should also be considered to account for the feedbacks from feedwater temperature and reactor dome pressure.

BWR plants have been designed since 1950s and put into operation starting from early 1960s [14]. The stability had been the major concern during the design development stage of BWRs and extensive experimental and analytical studies had been performed [19]. Starting from 1960s, different BWR types had been designed and some of them had been built. The ones that had been built and operated are

- Natural Circulation BWR (DODEWARD)
- External Recirculation with Jet Pump BWR (GE)
- Internal Recirculation-Pump BWR (Japan, Sweden)

Table 2.1. Classification of Flow Instabilities

Class:	Type:	Mechanism:	Characteristics:
Static Instabilities	Flow Excursion	Negative Slope of ΔP vs. \dot{m} curve	Flow undergoes sudden, large amplitude excursion to a new, stable operating condition
	Boiling Crisis	Ineffective removal of heat from heated surface	Wall temperature excursion and flow oscillations
	Flow Pattern Transition Instability	Churn-Turbulent flow has higher ΔP than that of annular flow	Cyclic flow pattern transitions and flow rate variations
	Bumping, geysering or chugging	Periodic adjustment of meta-stable condition, usually due to lack of nucleation sites	Periodic process of superheat and violent evaporation with possible expulsion and refilling
Dynamic Instabilities	Acoustic Oscillations	Resonance of Pressure Waves	High frequencies (10-100 Hz) related to time required for pressure wave propagation in the system
	Density Wave Oscillations	Delay and feedback effects in relationship between flow rate, density and pressure drop	Low frequencies (1 Hz) related to transit time of a continuity wave
	Pressure Drop Oscillation	Flow excursion initiates dynamic interaction between channel and compressible volume	Very low frequency (0.1 Hz) process
	Thermal Oscillations	Interaction of variable heat transfer coefficient with flow dynamics	It occurs in film boiling

All BWR types listed above have quite similar internal characteristics. The typical BWR vessel internals are

- Upper and Lower Downcomer
- Recirculation Pumps (internal or jet pumps)
- Lower Plenum
- Reactor Core
- Upper Plenum and Chimney
- Separator Assemblies
- Steam Dryer
- Steam Dome

For complete analysis of a BWR instability problem, all internal component of the reactor pressure vessel (RPV) should be modeled. However, the unstable flow behavior is most important inside the core region. For proper modeling and calculation of core boundary conditions, ex-core systems should be taken into account. Some of the ex-core related parameters are listed below:

1. Pressure drop caused by geometrical discontinuities (especially at the core and steam separator inlet)
2. Length and volume of the chimney section
3. Subcooling at the core inlet and the amount that can be changed by recirculation flow
4. Downcomer water level
5. Flow distribution in lower plenum towards fuel bundles

The BWR core is composed of several bundles supported by lower core support plate and separated from the downcomer by a shroud. Each fuel bundle has a number of fuel rods arranged in square lattice and contained by a square zircaloy box. The region between the fuel bundles is occupied by single-phase bypass coolant. Cruciform control blades and in-core flux detectors are inserted in this region. The function of the fuel boxes or fuel cans is

- To ensure sufficient moderation at the upper part of the core
- To prevent transversal mixing of mass flow of coolant
- To properly control the void distribution and flow

Depending on the fuel design, some of the fuel rods are replaced by water rods to enhance moderation. A small part of the total power in the reactor core ($\approx 5\%$) is generated in non-fuel regions (bypass coolant) because of the neutron moderation and the attenuation of γ -rays. In addition, some of the heat is transferred from the inside of the fuel bundles in which warmer coolant flows. Direct generation of heat in the bypass and coolant region is also called “Direct Heating” and can be important in stability problem.

For the stability problem, some of the important core-related parameters are listed as follows:

1. Axial power distribution (single-channel or core-wide oscillations)
2. Radial (global) power distribution (regional oscillations)
3. Fuel material and geometry (fuel conductance and its response time)
4. Reactivity coefficients (void and Doppler)
5. Core bypass flow area or fraction of bypass flow
6. Fuel bundle type and fuel burnup distribution
7. Control blade insertion pattern

As mentioned before, the balance-of-the-plant part of a BWR system is important for supplying boundary conditions for RPV. Balance-of-the-plant is defined as components and systems, which are necessary to convert thermal energy to electricity with efficiency (including turbine, condenser, feedwater heaters, moisture separators, relevant control systems, etc.). The parameters relevant to the instability issue in BWRs are

1. Feedwater flow rate and temperature
2. Steam dome pressure (controlled by turbine and turbine bypass valve)
3. Recirculation pump velocity (mainly controlled by turbine shaft load)
4. Feedwater preheaters' dynamics (affecting feedwater temperature)

Because of dynamic interaction of different physical processes, the proper modeling strategy of a BWR system is important not only for instability but also for the understanding of the static and dynamic characteristics of the plant. In order to clarify the phenomenon, Figure 2.1 demonstrates the basic physical processes involved in a BWR plant by showing the interactions in the processes. The accurate description of the reactor behavior during an instability event requires the modeling of each process. The analysis performed for a BWR instability problem has the following components:

1. Determining the stability margin during both normal and off-normal operating conditions
2. Predicting the transient behavior of the reactor parameters during unstable conditions such as the amplitude of oscillations
3. Designing and assessing the effectiveness of countermeasures adopted to prevent and mitigate the consequences of instabilities

In order to achieve these, it is necessary to establish realistic models for the physical phenomena and mechanisms that lead to unstable flow conditions. It is known that

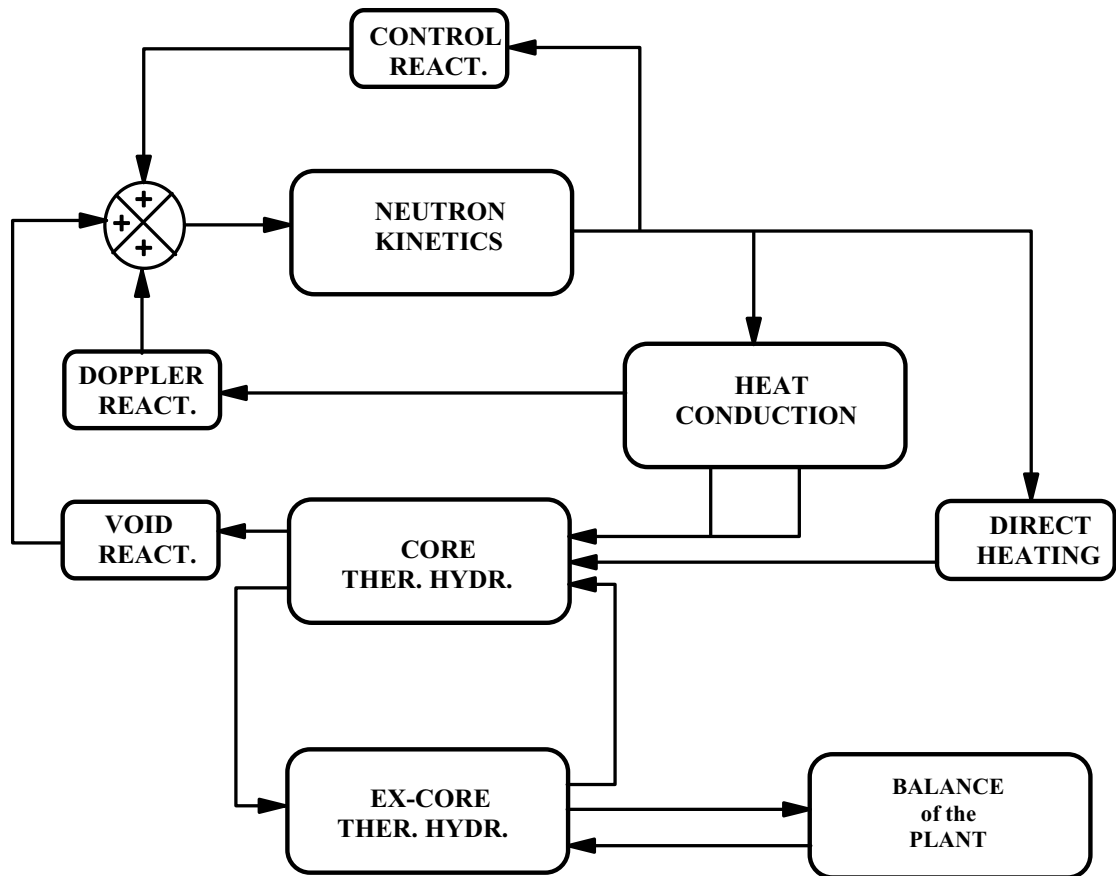


Figure 2.1. Physical Processes Involved in BWR Stability

the BWR stability problem is a result of complex interactions of thermal-hydraulics and neutronics, therefore models developed for the problem should account for both phenomena.

In a BWR core, different oscillation patterns might exist [20]. Each oscillation pattern requires different analysis approach. The oscillation patterns are

- Single-channel oscillations
- Core-wide oscillations
- Core-regional oscillations

In core-wide oscillations, similar to single-channel oscillations, all channels in the core behaves as if they are one single channel, while in core regional oscillations (also called out-of-phase oscillations) modeling of parallel channels, in which flow oscillates with certain phase shift, is necessary. In any case, boiling boundary dynamics, calculation of pressure drop components along the channel, heat conduction dynamics, heat transfer and flow regime determination are all necessary to address the issue properly. The implementation of neutronic feedbacks is also important and modeling can be done by either point kinetic model or three-dimensional kinetic model depending on the mode of oscillations that are being studied.

Recirculation loop dynamics is important for determining the core boundary conditions. In general, flow instabilities in a conventional BWR core can be analyzed by considering the core section only with appropriate boundary conditions. However, more accurate treatment of the problem requires the modeling of recirculation flow path including the phenomena of liquid-steam separation, recirculation, downcomer water mixing, lower plenum velocity field, etc. Exact treatment of core boundary conditions also requires the consideration of the balance-of-the-plant, since the dome pressure and the feedwater temperature are determined from the turbine-side dynamics.

The stability of a system can be quantified by analyzing the response of the system to a given perturbation. The stability, in absolute sense, can be derived by

analyzing the system response, i.e., whether it diverges from or converges to the initial state. The detailed analysis mostly depends on the level of the modeling and the main focus of the analysis. There are two most common tools for instability analysis:

1. Frequency Domain Analysis (linear)
2. Time Domain Analysis (nonlinear)

In frequency domain method, governing equations are linearized assuming small perturbation around steady state. By taking the Laplace transform, the problem can be converted into frequency domain and a transfer function for each process can be derived. By combining the transfer functions, overall characteristic equation can be derived and the stability of the system can be analyzed based on basic properties of the equation. There are many computer codes that have been developed for BWR stability issue. Lahey et al. [21] developed the computer code NUFREQ for nuclear-coupled oscillations in BWRs. The program was then updated by Park [22]. These methods are good for generating stability maps and analyzing parametric effects. However, it is impossible to observe the nonlinear effects on the phenomenon such as the amplitude.

In the time domain analysis method, the complete transient form of the equations is solved by using a wide variety of numerical methods. For the purpose of analysis, system analysis codes, such as RAMONA-4B, TRACE, and RELAP5, may be used, however the user should be careful about the code capability limit due to the numerical method and the model. There are also small scale computer codes used for stability analysis. For instance, Yokomizo [23] has developed a computer code which accounts for the non-equilibrium effects in two-phase flow, multi-channel core arrangement and neutron kinetics for oscillations in BWRs. The program has been adopted to commercial size BWRs and it has been concluded that the current design with frequency domain analysis is valid for finite disturbances.

2.3 Stability Problem in Natural Circulation BWRs

Natural circulation as a passive heat removal mechanism in both normal operations and accidental conditions has been studied extensively since 1950s. The early studies focused on steady natural circulation for both single-phase and two-phase flows. Through the early work, the utilization of natural circulation flow as a passively safe method to cool down the nuclear reactor under different scenarios has become increasingly practical for many types of reactors. Since the two-phase mixture has considerably smaller density compared to the single-phase liquid, two-phase natural circulation might produce much larger flow and provide better cooling capability. This is particularly true for water reactors where the coolant has a large latent heat, thus two-phase boiling heat transfer is also efficient. However, two-phase flow instabilities can accompany the natural circulation flow. This is a concern in next generation BWRs, which use natural circulation to drive the core flow, e.g., SBWR and ESBWR. Especially, the startup phase of these reactors is vulnerable to instabilities due to low pressure and low flow conditions. Geysering and flashing induced instabilities are most probable instability types and may impose a serious problem when flow oscillations are coupled to the core power via neutronic feedbacks.

Aritomi et al. [10, 11] and Chiang et al. [24] conducted fundamental studies of geysering in a parallel-channel natural circulation loop with the aim of establishing a rational startup procedure. They pointed out that in-phase natural circulation oscillation was induced by hydrostatic head fluctuations in a non-heated channel due to insufficient vapor generation. The effect of superheated liquid and flashing at the chimney section on the instabilities were not addressed in their work.

Inada et al. [25] investigated flow instabilities in a boiling natural circulation loop with a chimney. Their work revealed that adiabatic flashing due to decrease in gravity head in the chimney plays an important role in the two-phase instability. The type of instability that occurred in their experiments was suggested to be density wave oscillations due to flashing in the chimney. In relation to the Three-Mile Accident (TMI), Lee and Ishii [26] performed a two-phase natural circulation instability study

in a simulated B&W light water reactor geometry. Here they found that the flashing in the riser section induced large amplitude cyclic instability. Other instabilities which can occur has been found to be DWO and manometric oscillations. Babelli [27] incorporated the effect of void generation due to flashing in the chimney section into his model for the stability boundary of a low-flow and low-pressure natural circulation system.

Paniagua et al. [28] also emphasized the pressure dependency of the local thermal-hydraulic parameters in the prediction of possible startup instabilities. In their model, the local parameters were calculated based on local pressure estimated using the steady-state distribution. The model was validated with the experimental data obtained in a low-pressure natural circulation loop at high subcooling.

Part I

Analytical Modeling

3. FLOW FIELD FORMULATION

The formulation of the problem is kept general such that it considers DWOs are discussed in this chapter. The objective is to develop a model for these two instability types to understand the leading physical phenomena in the dimensionless space. The solution of the steady state form of the governing field equations for the flow excursion and the frequency domain representation for the DWOs as described by Ishii [12] are used to investigate the problem.

The problem formulation is kept general in such a way that the model considers the single-phase heated section, the two-phase heated and unheated sections of a typical two-phase flow system. Based on this arrangement of the flow, the modeling results are applied for the analysis of the flow excursion and DWOS in a single heated channel and a natural circulation loop.

One dimensional drift flux model is used for the two-phase flow and the subcooled boiling is taken into account by introducing Saha-Zuber [29] departure enthalpy model for the point of net vapor generation (PNVG) and Levy [30] profile fit model for the volumetric vapor generation in the subcooled boiling.

The model equations are introduced for each region (single-phase and two-phase) based on some simplifying assumptions. With given scaling variables, the dimensional analysis is carried out to derive the dimensionless groups for the problem of consideration.

As briefly described in Chapter 2, the flow excursion stability criterion can be derived based on the steady state solution of the field equations. However, for the DWOs, the solution of the transient field equations is needed to describe the phenomena. Linear stability provides a basic tool for understanding the dynamics instability in the frequency domain by means of the Laplace Transform of the linearized equa-

tions.

3.1 Description of the Flow Systems

Two different flow systems are considered in the present analysis. The first system demonstrates a typical BWR flow channel in the form of a bundle. The schematic is demonstrated in Figure 3.1. In most of the practical problems, constant pressure drop boundary condition for a single channel is valid especially for parallel channel systems. As shown in Figure 3.1, a bypass channel is associated to the heated channel as a parallel channel. When most of the flow is through the bypass section, which is the single phase flow, the pressure drop across the heated channel is determined by the stable bypass flow. The bypass channel also simulates the stable channel in a BWR core when few channel oscillates with certain frequency while the flow in the other channels is stable. In either case, the heated section can be characterized with a single heated channel. The inlet and the outlet plenum in Figure 3.1 represent constant pressure reservoirs. The pressure difference between two plenums drives the flow. Single-phase coolant enters the heated section with a certain amount of subcooling. As it is heated inside the channel, it reaches to the saturation (or PNVG) and the two-phase flow appears in the channel. The flow leaves the channel with a certain void fraction. Therefore, two different regions (single-phase heated and two-phase heated) describes the channel thermal hydraulics for the system shown in Figure 3.1.

The second system shown in Figure 3.2 is a simplified version of the typical two-phase natural circulation loop, which can be applied to the SBWR design. The gravity head in the downcomer section drives the flow and it can be assumed constant. Therefore, the constant pressure drop boundary condition from the heated section inlet to the unheated section outlet is valid. The two-phase unheated section, which is characterized as a riser is considered adiabatic. The flow area is considerably larger than the heated section and the gravitational pressure drop is dominant in the total pressure drop in the riser section. The two-phase mixture is separated in the separator/dryer section and the separated steam leaves the loop. The separated

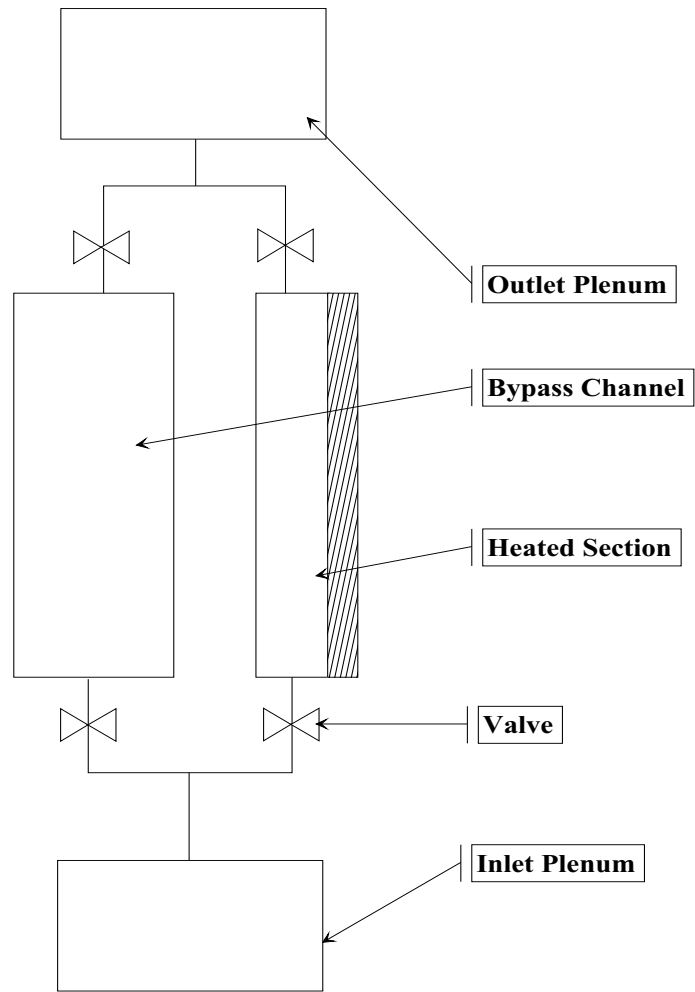


Figure 3.1. Typical Geometrical Arrangement for a Forced Circulation System

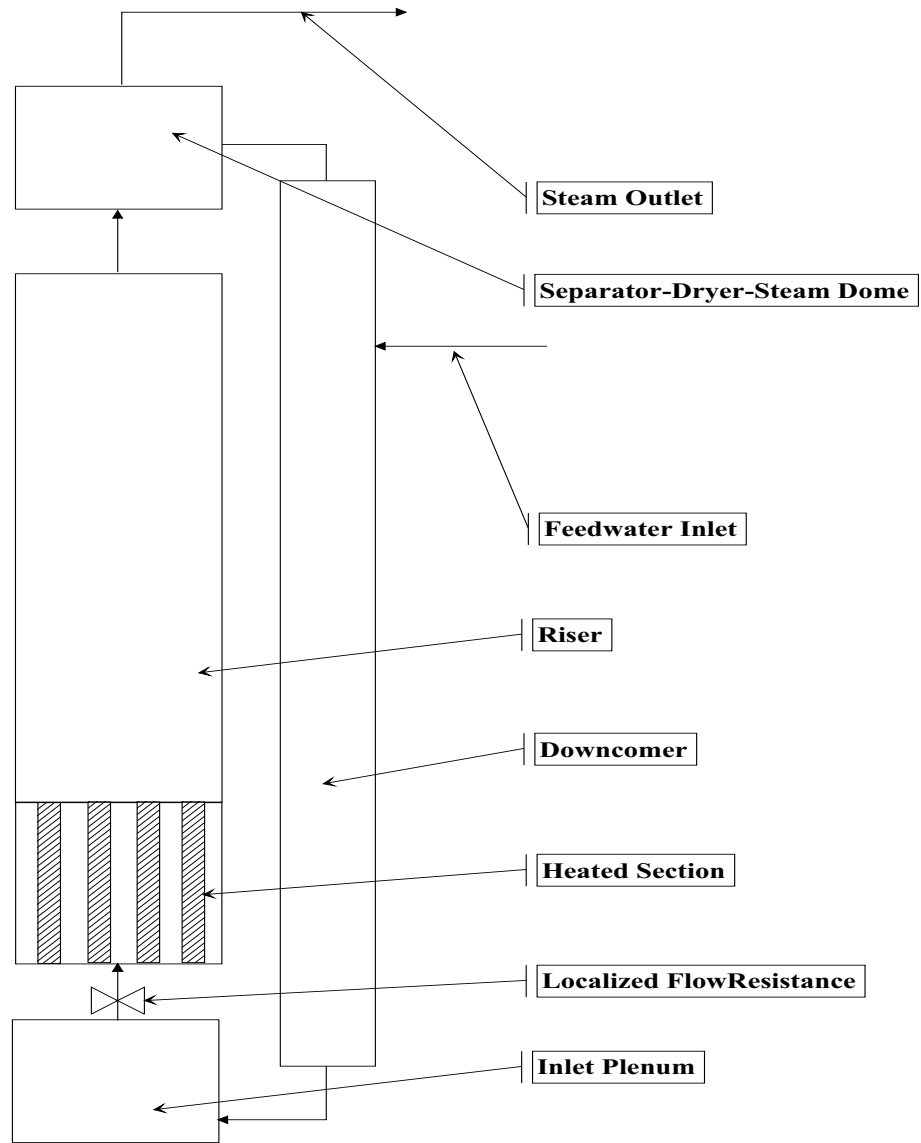


Figure 3.2. Typical Flow Arrangment for a Natural Circulation System

liquid is mixed with cold feedwater and flows downward inside the downcomer and completes the circulation loop. The frictional loss is also negligible in the downcomer and can be considered adiabatic similar to the riser section.

3.2 One Dimensional Drift Flux Model

Drift Flux Model is a valuable tool in two-phase flow problems. Especially for the steady state analysis or the mild transients in BWRs, Drift Flux Model can be used to overcome the difficulties associated with the two-fluid Model [31]. In the Drift Flux Model, the velocity field is expressed in terms of the mixture center-of-mass velocity and the drift velocity of the vapor phase. The most important assumption in the model is that the dynamics of the phases can be expressed by the mixture momentum equation with the kinematic constitutive equations specifying the relative motion between the phases. The detailed discussion on the Drift Flux Model and the derivation of the three-dimensional form of the field equations resulting from the time or the statistical averaging can be found in Ref. [32].

One dimensional form of the Drift Flux Model can be obtained by applying the area-averaging to the three-dimensional form of the field equations as described in Ref. [33]. A simple area averaging of a variable Ψ over the cross sectional area A is defined as

$$\langle \Psi \rangle = \frac{1}{A} \int_A \Psi dA \quad (3.1)$$

The area averaging can also be performed over the phase area. For instance, the area-averaged k^{th} phase (either liquid, f , or vapor, g) variable Ψ_k is defined as:

$$\langle \langle \Psi_k \rangle \rangle = \frac{\langle \Psi_k \alpha_k \rangle}{\langle \alpha_k \rangle} \quad (3.2)$$

In the formulation, it can be assumed that phase density within each phase is uniform ($\langle \langle \rho_k \rangle \rangle = \rho_k$). This assumption is reasonable when the transverse pressure gradient is relatively small compared to the axial one. Therefore, the area-averaged mixture

density can be defined as

$$\langle \rho_m \rangle = \rho_f - \langle \alpha \rangle \Delta \rho \quad (3.3)$$

where $\Delta \rho = \rho_f - \rho_g$ is the density difference between liquid and vapor. The area-averaged phasic velocities can be given as

$$\langle \langle v_k \rangle \rangle = \frac{\langle v_k \alpha_k \rangle}{\langle \alpha_k \rangle} = \frac{\langle j_k \rangle}{\langle \alpha_k \rangle} \quad (3.4)$$

where $\langle j_k \rangle$ is the superficial velocity or the volumetric flux of the phase k . Based on the definitions given by Eqs. (3.3), and (3.4), the mixture velocity and the enthalpy are defined by weighting with the mixture density

$$\bar{v}_m = \frac{\langle \rho_m v_m \rangle}{\langle \rho_m \rangle} = \frac{\langle \alpha \rangle \rho_g \langle \langle v_g \rangle \rangle + (1 - \langle \alpha \rangle) \rho_f \langle \langle v_f \rangle \rangle}{\langle \rho_m \rangle} \quad (3.5a)$$

$$\bar{i}_m = \frac{\langle \rho_m i_m \rangle}{\langle \rho_m \rangle} = \frac{\langle \alpha \rangle \rho_g \langle \langle i_g \rangle \rangle + (1 - \langle \alpha \rangle) \rho_f \langle \langle i_f \rangle \rangle}{\langle \rho_m \rangle} \quad (3.5b)$$

where i_k is the enthalpy of the phase k . In general, the vapor phase can be assumed at saturation ($i_g = i_{gs}$) while the liquid phase can be subcooled, saturated or superheated.

The mean drift velocity, \bar{v}_{gj} is one of the important parameter for the closure in drift flux model since it determines the kinematics of the flow with given area-averaged mixture volumetric flux, $\langle j \rangle$.

$$\bar{v}_{gj} = \langle \langle v_g \rangle \rangle - \langle j \rangle = (C_o - 1) \langle j \rangle + \langle \langle v_{gj} \rangle \rangle \quad (3.6)$$

where C_o is the distribution parameter, which represents the covariance between the mixture volumetric flux, j , and void fraction, α . The definition of the distribution parameter, C_o , is given as follows:

$$C_o = \frac{\langle \alpha j \rangle}{\langle \alpha \rangle \langle j \rangle} \quad (3.7)$$

The first term on the right-hand-side of Eq. (3.6) represents the global drift while the second term represents the local drift of the vapor phase respect to the mixture. The phasic velocities defined in Eq. (3.4) can be related to the mixture volumetric flux, $\langle j \rangle$, as a function of the two important drift flux parameters, namely the distribution parameter, C_o , and the mean drift velocity, $\langle \langle v_{gj} \rangle \rangle$,:

$$\langle \langle v_g \rangle \rangle = C_o \langle j \rangle + \langle \langle v_{gj} \rangle \rangle \quad (3.8a)$$

$$\langle \langle v_f \rangle \rangle = \frac{1 - \langle \alpha \rangle C_o}{1 - \langle \alpha \rangle} \langle j \rangle - \frac{\langle \alpha \rangle}{1 - \langle \alpha \rangle} \langle \langle v_{gj} \rangle \rangle \quad (3.8b)$$

3.2.1 Field Equations

In the drift flux model, different forms of continuity equations can be written in terms of different velocity fields. In the following equation, the mixture continuity equation is introduced:

$$\frac{\partial \langle \rho_m \rangle}{\partial t} + \frac{\partial \langle \rho_m \rangle \bar{v}_m}{\partial z} = 0 \quad (3.9)$$

By using the phasic velocities given by Eq. (3.4), the mixture velocity can be related to the mixture volumetric flux as

$$\bar{v}_m = \left(\frac{\rho_f - C_o \langle \alpha \rangle \Delta \rho}{\langle \rho_m \rangle} \right) \langle j \rangle - \frac{\langle \alpha \rangle \Delta \rho}{\langle \rho_m \rangle} \quad (3.10)$$

Another continuity equation is written for the vapor phase by considering the compressibility of the phase as follows:

$$\frac{\partial \langle \alpha \rangle}{\partial t} + \frac{\partial \langle \alpha \rangle \langle \langle v_g \rangle \rangle}{\partial t} = \frac{\langle \Gamma_g \rangle}{\rho_g} - \langle \alpha \rangle \eta_g \frac{D_g P}{Dt} \quad (3.11)$$

where $\eta_g = \frac{1}{\rho_g} \frac{\partial \rho_g}{\partial P}$ is the compressibility of gas phase, and $\langle \Gamma_g \rangle$ is the area-averaged volumetric vapor generation rate. $\frac{D_k}{Dt}$ is the material derivative for the k^{th} phase

defined in terms of the k^{th} phase velocity:

$$\frac{D_k(\quad)}{Dt} = \frac{\partial(\quad)}{\partial t} + \langle\langle v_k \rangle\rangle \frac{\partial(\quad)}{\partial z} \quad (3.12)$$

The equation for the mixture volumetric flux can be obtained from the vapor and liquid continuity equations as,

$$\frac{\partial\langle j \rangle}{\partial z} = \langle\Gamma_g\rangle \frac{\Delta\rho}{\rho_f\rho_g} - \langle\alpha\rangle\eta_g \frac{D_g P}{Dt} - \langle 1 - \alpha \rangle\eta_f \frac{D_f P}{Dt} \quad (3.13)$$

where $\eta_f = \frac{1}{\rho_f} \frac{\partial\rho_f}{\partial P}$ is the compressibility of the liquid phase. By means of Eqs. (3.13) and (3.11), the void propagation equation is obtained as follows:

$$\begin{aligned} \frac{\partial\langle\alpha\rangle}{\partial t} + \langle C_k \rangle \frac{\partial\langle\alpha\rangle}{\partial z} = & \langle\Gamma_g\rangle \left(\frac{\rho_f - C_o\langle\alpha\rangle\Delta\rho}{\rho_f\rho_g} \right) \\ & + \langle\alpha\rangle \left(\eta_g \frac{D_g P}{Dt} \left(\langle\alpha\rangle C_o - 1 \right) + \eta_f \frac{D_f P}{Dt} C_o \left(1 - \langle\alpha\rangle \right) \right) \end{aligned} \quad (3.14)$$

where $\langle C_k \rangle$ is the kinematic wave velocity, which is given as

$$\langle C_k \rangle = \left(C_o + \langle\alpha\rangle \frac{\partial C_o}{\partial\langle\alpha\rangle} \right) \langle j \rangle + \langle\langle v_{gj} \rangle\rangle + \langle\alpha\rangle \frac{\partial\langle\langle v_{gj} \rangle\rangle}{\partial\langle\alpha\rangle} \quad (3.15)$$

When the void fraction dependency on the drift flux parameters is ignored, the kinematic wave velocity reduces to the vapor velocity. This is particularly valid in the churn-turbulent flow, where C_o and $\langle\langle v_{gj} \rangle\rangle$ are independent of the void fraction. The first term on the right-hand-side of Eq. (3.14) is the source term due to heat transfer or flashing, the second term represents the bubble sink/source due to compressibility of the phases. Generally, the liquid can be considered as incompressible. The second term in Eq. 3.14 becomes the source when the pressure gradient is negative. This term may become significant in the chimney section at low pressure conditions.

The momentum equation for the mixture is given by the following equation:

$$\begin{aligned}
\frac{\partial \langle \rho_m \rangle \bar{v}_m}{\partial t} + \frac{\langle \rho_m \rangle \bar{v}_m^2}{\partial z} = & -\frac{\partial P}{\partial z} + \frac{\partial(\tau_{zz} + \tau_{zz}^T)}{\partial z} - \langle \rho_m \rangle g_z \\
& - \frac{f_m}{2D_h} \langle \rho_m \rangle \bar{v}_m |\bar{v}_m| - \frac{\partial}{\partial z} \left(\frac{\langle \alpha \rangle \rho_f \rho_g}{(1 - \langle \alpha \rangle) \langle \rho_m \rangle} \bar{v}_{gj}^2 \right) \\
& - \frac{\partial}{\partial z} \sum_k COV(\alpha_k \rho_k v_k v_k)
\end{aligned} \tag{3.16}$$

Since the problem is formulated in terms of the center-of-mass velocity of the mixture, the mixture momentum equation in terms of the mixture velocity needs to be solved. In the mixture momentum equation given by Eq. (3.16), $\tau_{zz} + \tau_{zz}^T$ denotes the normal component of the stress tensor in the axial direction. The third and the fourth term on the right-hand-side of the equation represent the gravitational pressure gradient and the two-phase frictional pressure gradient with two-phase friction factor f_m , respectively. The fifth term is for the pressure drop due to the drift. The last term denotes the covariance which shows the difference between product of averages and average of products.

The mixture enthalpy equation for One Dimensional Drift Flux Model is written as

$$\begin{aligned}
\frac{\partial \langle \rho_m \rangle \bar{i}_m}{\partial t} + \frac{\partial \langle \rho_m \rangle \bar{v}_m \bar{i}_m}{\partial z} = & -\frac{\partial(q'' + q''^T)}{\partial z} + \frac{q_w'' \xi_h}{A} \\
& - \frac{\partial}{\partial z} \left(\frac{\langle \alpha \rangle \rho_g \rho_f}{\langle \rho_m \rangle} \Delta i_{fg} \bar{v}_{gj} \right) + \frac{D_j P}{Dt} + \langle \Phi_m \rangle^\mu \\
& - \frac{\partial}{\partial z} \sum_k COV(\alpha_k \rho_k i_k v_k)
\end{aligned} \tag{3.17}$$

where the substantial derivative, $\frac{D_j}{Dt}$, is defined in terms of the mixture volumetric flux. The first term on the right-hand-side of Eq. (3.17) represents the axial conduction heat flux, the second term is for the wall heat flux. The last term denotes the energy dissipation, which can be neglected in most cases.

In the Drift Flux Formulation, the problem is solved for $\langle \alpha \rangle$ and $\langle j \rangle$ with the

given constitutive relation for \bar{v}_{gj} . The velocity field can be recovered by using Eq. (3.8). Another important parameter to be supplied is area-averaged volumetric vapor generation rate, $\langle\Gamma_g\rangle$, which also accounts the thermodynamic nonequilibrium between the phases.

3.2.2 Constitutive Equations for Drift Flux Parameters

As described in Section 3.2, the distribution parameter, C_o , and the void-weighted mean drift velocity, $\langle\langle v_{gj} \rangle\rangle$, should be supplied via constitutive relations to close the system for the velocity field. There are several correlations and models suggested for these two parameters based on extensive experimental database. Ishii [33] derived constitutive equations for the drift flux parameters by taking into account the interfacial geometry, the body force field, the shear stresses, and the interfacial momentum transfer. The details of the equations are not reproduced here. However, three different flow regimes are emphasized; i. Bubbly Flow, ii. Churn-Turbulent Flow, iii. Annular Flow. In general, the distribution parameter has the following limits,

$$\begin{aligned} \lim_{\langle\alpha\rangle\rightarrow 0} C_o &= 0 \quad , \quad \lim_{\langle\alpha\rangle\rightarrow 1} C_o = 1 \\ \lim_{\rho_g/\rho_f\rightarrow 1} C_o &= 1 \end{aligned} \quad (3.18)$$

The bubbly flow generally appears below % 30 void fraction. The distribution parameter and the void-weighted mean drift velocity for the bubbly flow are given by the following equations,

$$C_o = \left(1.2 - 0.2\sqrt{\frac{\rho_g}{\rho_f}}\right) \left(1 - e^{-18\langle\alpha\rangle}\right) \quad (3.19a)$$

$$\langle\langle v_{gj} \rangle\rangle = \sqrt{2}(1 - \alpha)^{1.75} \left(\frac{\sigma g \Delta \rho}{\rho_f^2}\right)^{0.25} \quad (3.19b)$$

where σ is the surface tension. Eq. (3.19a) is also valid in the churn-turbulent regime. However, the exponential term approaches zero when void fraction increases. The following two equations represents the distribution parameter, C_o , and void fraction

weighted drift velocity, $\langle\langle v_{gj} \rangle\rangle$, in the churn-turbulent regime:

$$C_o = \left(1.2 - 0.2 \sqrt{\frac{\rho_g}{\rho_f}} \right) \quad (3.20a)$$

$$\langle\langle v_{gj} \rangle\rangle = \sqrt{2} \left(\frac{\sigma g \Delta \rho}{\rho_f^2} \right)^{0.25} \quad (3.20b)$$

For the annular flow, the expressions are given as

$$C_o = 1 + \frac{1 - \alpha}{\alpha + 4 \sqrt{\frac{\rho_g}{\rho_f}}} \quad (3.21a)$$

$$\langle\langle v_{gj} \rangle\rangle = \frac{1 - \alpha}{\alpha + 4 \sqrt{\frac{\rho_g}{\rho_f}}} \sqrt{g D \Delta \rho \frac{(1 - \alpha)}{0.015 \rho_f}} \quad (3.21b)$$

Equations (3.21a) and (3.21b) are simplified based on the assumption that $\rho_g \ll \rho_f$, which is valid especially at low pressure.

3.3 Subcooled Boiling

In the flow systems shown in Figure 3.1 and 3.2, the flow enters the heated section of the channel as subcooled ($T_{in} < T_{sat}$) and its temperature rises due to heat addition from the wall. At certain axial location in the channel, the fluid near the wall becomes superheated and can nucleate a vapor bubble while the bulk liquid temperature may still be lesser than the saturation temperature. When the subcooled boiling starts, some part of the heat goes to the vapor formation and the other part goes to increase the liquid temperature. During initial stage of the process, the wall voidage occurs and void fraction value is very low. Because of the thermal boundary layer developed over the bubble region, bubbles detached from the wall condenses in subcooled liquid. After the bulk liquid temperature reaches certain value, bubbles merge from the wall and increases the void fraction significantly. The point where significant bubble departure occurs is called “Point of Net Vapor Generation”(PNVG). This point separated the single phase flow from the two-phase mixture flow in the

heated section. The general approach for specifying this point is to specify the bulk liquid temperature or the enthalpy at which significant bubble departure occurs is called “departure enthalpy”.

3.3.1 Departure Enthalpy

There are many proposed correlations to calculate the departure enthalpy [34, 35, 36]. However, Saha et al. [29] developed a very simple and elegant correlation for the departure enthalpy. The developed correlation simply states that PNVG is either controlled thermally or hydrodynamically depending on the value of the Peclet number. At high inlet subcoolings, it has been stated that PNVG is independent of the subcooling. This demonstrates that the PNVG is determined by the thermal conditions on the wall. When the mass flow rate is low, the local Nusselt number becomes the scaling parameter. The nusselt number is defined as

$$N_{Nu} = \frac{q'' D_e c_{pf}}{k_f (i_{fs} - i_d)} \quad (3.22)$$

where i_d is the void departure enthalpy, k_f is the liquid thermal conductivity, c_{pf} is the specific heat of the liquid, i_{fs} is the saturated liquid enthalpy, and D_e is the equivalent hydraulic diameter. q'' in Eq. (3.22) is the wall heat flux. It has been also shown that the PNVG becomes independent from the hydrodynamics when the mass flow rate is sufficiently high. Saha et al. [29] stated that the bubbles attached to the surface enhance the surface roughness and therefore the conditions should correspond to a scale of roughness. From Reynold analogy, the stanton number becomes a scaling parameter which is defined as follows:

$$N_{St} = \frac{q''}{G(i_{fs} - i_d)} \quad (3.23)$$

where G is the mass flux.

In the Saha-Zuber model, the Peclet number, which is the ratio of the stanton number and the nusselt number, is used to determine the division between thermally

and hydrodynamically controlled regions for the net vapor generation point. The peclet number is defined as

$$N_{Pe} = \frac{G c_{pf}}{k_f} \quad (3.24)$$

Saha and Zuber [29] experimentally determined that the dividing line between the regions is a peclet number of about 70,000. If the peclet number is lesser than 70,000 then the PNVG is thermally controlled. Otherwise, it is controlled hydrodynamically. In each region, the stanton number and the nusselt number have been determined experimentally. It has been found that nusselt number is constant around 455 in the thermally controlled region. The correlation for the departure enthalpy is given by the following equation;

$$i_{ds} = i_{fs} - \begin{cases} 0.0022 \frac{q'' D_e c_{pf}}{k_f} & N_{Pe} < 70000 \\ 154 \frac{q''}{G} & N_{Pe} > 70000 \end{cases} \quad (3.25)$$

3.3.2 Model for Volumetric Vapor Generation Rate

In this section, the modeling details for the volumetric vapor generation rate, $\langle \Gamma_g \rangle$,¹ accounting the subcooled boiling region are introduced. The derivation is based on profile-fit-model. The idea of the model is given by the relation between the flow quality and the thermodynamic equilibrium quality, proposed by Levy [30]. The relation is given by

$$x(z) = x_e(z) - x_{ed} \exp \left[\frac{x_e(z)}{x_{ed}} - 1 \right] \quad (3.26)$$

where x_e is the thermodynamic quality, which can be determined from the mixture enthalpy assuming thermodynamic equilibrium between the phases. $\langle x_{ed} \rangle$ is the thermodynamic equilibrium quality at PNVG, which is determined via the departure entalpy. The equilibrium quality can be related to volumetric vapor generation rate

¹For simplicity, the averaging symbol is removed from the two-phase flow parameters throughout the chapter

in thermal equilibrium conditions from the energy equation

$$G \frac{dx_e}{dz} = \Gamma_s \quad (3.27)$$

where $\Gamma_s = \frac{q'' \xi_h}{A \Delta i_{fg}}$ is the volumetric vapor generation at saturated boiling which assumes that all heat from the wall goes to vaporize the saturated liquid. Δi_{fg} is the latent heat. A_h is the heated section flow area and ξ_h is the heated perimeter. It can also shown that under the steady state conditions, the flow quality is related to volumetric vapor generation rate as

$$G \frac{dx}{dz} = \Gamma_g \quad (3.28)$$

By using Eq. (3.26), the volumetric vapor generation rate distribution along the channel after PNVG is written as

$$\frac{\Gamma}{\Gamma_s} = 1 - \exp \left[- \frac{z - \lambda}{\lambda_s - \lambda} \right] \quad (3.29)$$

where λ is the PNVG and λ_s is the point where bulk liquid reaches the saturation temperature. Figure 3.3 shows a typical void profile indicating the region of subcooled boiling. As demonstrated in the figure, the volumetric vapor generation rate starts from zero at the PNVG. Even though the wall voidage exists before the PNVG, the void fraction is still very low and can be neglected hydrodynamically. The profile given with Eq. (3.29) converges to Γ_s . However, the dimensionless profile given by Eq. (3.29) approaches to one at infinity mathematically. This is rather simplified model and gives reasonably accurate results under the steady state conditions [30].

Based on the model presented here, the void profile in a heated channel can be written by solving the steady-state void continuity and the mixture volumetric flux equations (Eqs. (3.11) and (3.13)). Neglecting the compressibility effects and using the constant drift flux parameters, the steady state void fraction can be written as

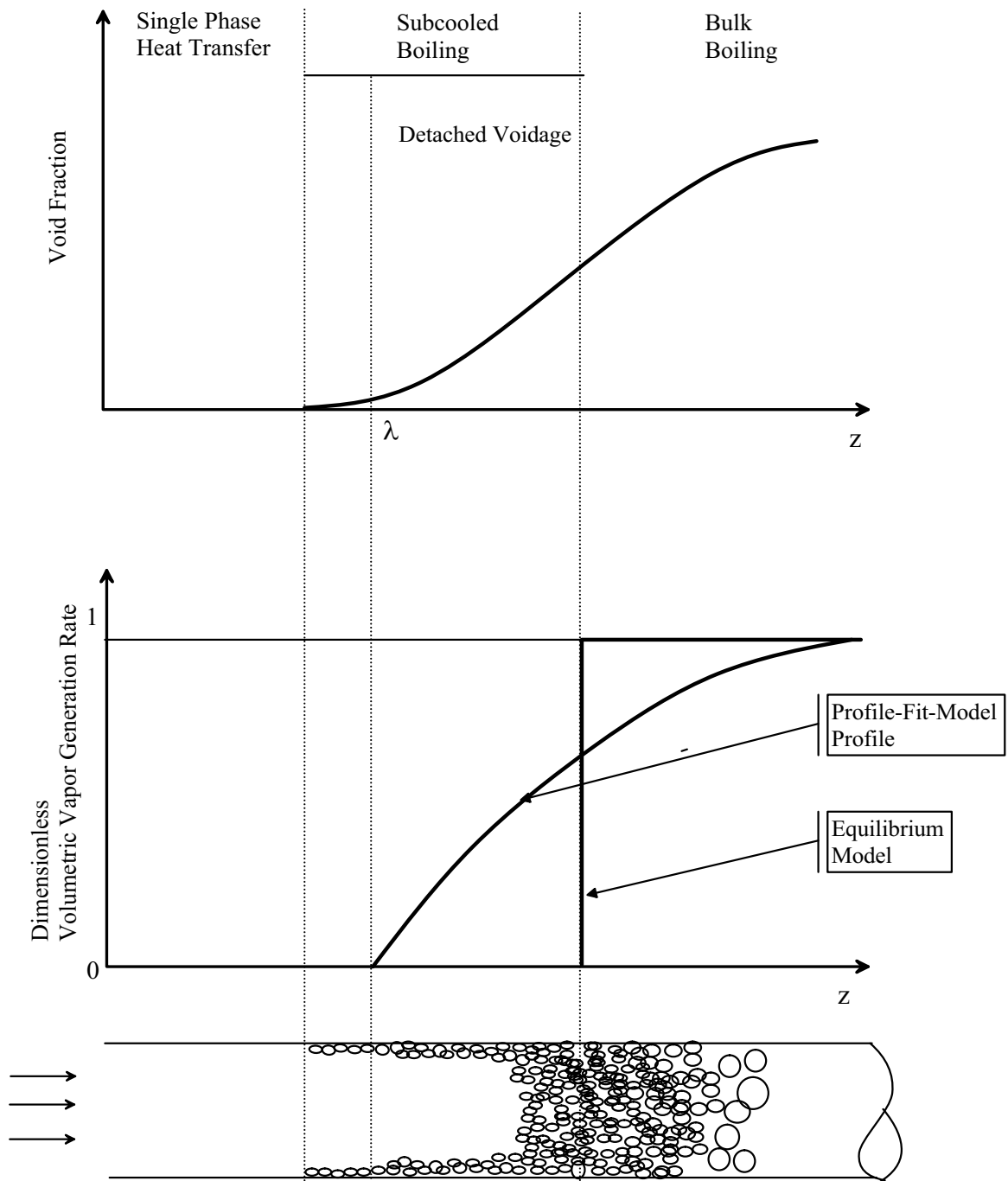


Figure 3.3. Typical Void Development and Volumetric Vapor Generation Rate in a Heated Channel including the Subcooled Boiling Region

follows:

$$\alpha(z) = \frac{\frac{\Gamma_s}{\rho_g}(\lambda_s - \lambda) \left[\frac{z - \lambda}{\lambda_s - \lambda} + \exp \left\{ -\frac{z - \lambda}{\lambda_s - \lambda} \right\} \right]}{C_o j + \langle \langle v_{gj} \rangle \rangle} \quad (3.30)$$

where the area-averaged mixture volumetric flux, $j(z)$ can be written as

$$j(z) = v_f + \frac{\Gamma_s \Delta \rho}{\rho_f \rho_g} (\lambda_s - \lambda) \left[\frac{z - \lambda}{\lambda_s - \lambda} + \exp \left\{ -\frac{z - \lambda}{\lambda_s - \lambda} \right\} \right] \quad (3.31)$$

For the modeling of the flow excursion, the momentum equation needs to be integrated and the profile given by Eq. (3.30) makes the analytical integration difficult. Therefore, the axial-averaged value for Γ_g can be used in the modeling by conserving the total area under the $\Gamma(z)$ curve to get simplified expression for the pressure drop components:

$$\langle \Gamma \rangle = C_g \Gamma_s \quad (3.32)$$

where the multiplier, C_g is defined as

$$C_g = 1 - \frac{\lambda_s - \lambda}{l_h - \lambda} \left[1 - \exp \left\{ -\frac{l_h - \lambda}{\lambda_s - \lambda} \right\} \right] \quad (3.33)$$

where l_h is the heated length of the heated section.

3.4 Governing Equations

In this section, the governing equations for the modeling of the flow instabilities are presented. The equations in dimensional space are given for the two different regions; Single-Phase Region and Two-Phase Mixture Region. For simplicity, the averaging operators are omitted from the field equations. However, the parameters in the equations presented in this section must be understood as area-averaged parameters.

3.4.1 Single Phase Flow

The flow enters the channel as subcooled and until it reaches to void departure temperature single phase flow exists in the channel. The continuity equation for the liquid can be written by assuming constant liquid density as follows:

$$\frac{\partial v_f}{\partial z} = 0 \quad (3.34)$$

which implies that v_f is spatially uniform and equals to inlet velocity, $v_{fin}(t)$, which changes in time. For the boiling boundary determination, single phase energy equation needs to be solved with boundary condition introduced at the channel inlet as the subcooling, $\Delta i_{sub} = i_{fs} - i_i$. At the boiling boundary, the void departure enthalpy given by Eq. (3.25) is used. The single phase energy equation in the heated section is given as:

$$\frac{\partial i_f}{\partial t} + v_{fin} \frac{\partial i_f}{\partial z} = \frac{q'' \xi_h}{A_h \rho_f} \quad (3.35)$$

The wall heat flux is axially uniform in the channel and the wall heat capacitance is neglected. Therefore, the wall heat flux can be directly related to the heat generation. This is reasonable approximation especially for solids having high thermal conductivity and low heat capacity.

The momentum equation in the single-phase region is written as follows:

$$-\frac{dP}{dz} = \rho_f \frac{dv_{fin}}{dt} + \frac{f_{1\phi}}{2D_e} \rho_f v_f^2 + \rho_f g \sin(\theta) + \frac{1}{2} K_{in} \rho_f v_{fin}^2 \delta(z) \quad (3.36)$$

where the normal component of the axial shear stress and the covariance in the velocity have been neglected. The angle, θ , in Eq. (3.36) shows the channel orientation. For instance, $\theta = 90$ defines the vertical upward flow. K_{in} is the flow loss coefficient at the channel inlet.

3.4.2 Two-Phase Mixture Flow

In the two-phase mixture region, the one dimensional drift flux model is used with some simplifying assumptions. First of all, the compressibility effects are ne-

glected. Moreover, the drift flux parameters, C_o and $\langle\langle v_{gj} \rangle\rangle$ are assumed to be constant, i.e. independent from the flow regime. This assumption simplifies the analytical modeling results.

The mixture continuity equation can be written as

$$\frac{\partial \rho_m}{\partial z} + \frac{\partial \rho_m v_m}{\partial z} = 0 \quad (3.37)$$

With simplifying assumption, the void wave equation given by Eq. (3.14) reduces to the following form

$$\frac{\partial \alpha}{\partial t} + C_k \frac{\partial \alpha}{\partial z} = C_g \frac{\Gamma_s}{\rho_g} \quad (3.38)$$

which can be written as density wave equation by means of Eq. (3.3):

$$\frac{\partial \rho_m^+}{\partial t} + C_k \frac{\partial \rho_m^+}{\partial z} = -C_o C_g \frac{\Gamma_s \Delta \rho}{\rho_f \rho_g} \quad (3.39)$$

where C_g is the multiplier defined in Eq. (3.33) to account for the subcooled boiling, and ρ_m^* is the modified density which can be related to the mixture density as follows:

$$\rho_m = \frac{C_o - 1}{C_o} + \frac{1}{C_o} \rho_m^+ \quad (3.40)$$

In Eq. (3.38), the kinematic wave velocity, C_k , becomes:

$$C_k = C_o j + \langle\langle v_{gj} \rangle\rangle \quad (3.41)$$

which is the void-weighted vapor velocity. The mixture volumetric flux equation is simplified from Eq. (3.13) as follows:

$$\frac{\partial j}{\partial z} = C_g \Gamma_s \frac{\Delta \rho}{\rho_f \rho_g} \quad (3.42)$$

The boundary condition for Eq. (3.42) is given at boiling boundary. At $z = \lambda$, $j = v_f(\lambda, t)$, which is the channel inlet velocity.

As described in the previous section, the volumetric vapor generation rate can be related to the parameters which can be obtained from the single-phase energy equation and the void-departure enthalpy correlation. Therefore, the energy equation for the mixture given by Eq. (3.17) is redundant.

The mixture momentum equation including the effect of the drift stress is given as follows:

$$\begin{aligned}
-\frac{dP}{dz} = & \rho_m \frac{\partial v_m}{\partial t} + \rho_m v_m \frac{\partial v_m}{\partial z} + \frac{f_m}{2D_e} \rho_m v_m^2 + \rho_m g \sin(\theta) \\
& + \frac{\partial}{\partial z} \left[\frac{\rho_f - \rho_m}{\rho_m - \rho_g} \frac{\rho_f \rho_g}{\rho_m} \bar{v}_{gj}^2 \right] + \frac{1}{2} K_e \rho_m v_m^2 \delta(z - l_h)
\end{aligned} \tag{3.43}$$

where the two-phase friction factor, f_m , can be related to $f_{1\phi}$ by introducing a multiplier, C_m . This multiplier modifies the two-phase friction multiplier, Φ_{lo}^2 , written for the Homegenous Equilibrium Model (HEM);

$$\Phi_{lo}^2 = C_m \left[1 + \frac{\Delta\rho}{\rho_g} \langle x \rangle \right] \tag{3.44}$$

The value ranging from 1 to 2 for C_m is reasonable for the appropriate two-phase frictional pressure drop calculations. K_e in Eq. (3.43) represents the flow loss coefficient at the heated channel exit.

3.5 Dimensional Analysis and Scaling

In this section, the dimensionless analysis is carried out to derive the dimensionless groups for the static and the dynamics of a general two-phase flow systems based on the sipmlifying assumptions described before. The analysis is given by choosing proper scaling parameters for the system. The details of the system is described by Ishii [12].

Table 3.1 shows the scaling variables used for several dimensions and parameters in the problem. For the time, inverse of the reaction frequency, Ω_s , is used. It is also

Scaled Variable	Scaling Parameter
Time	Ω_s^{-1}
Length	l_h
Area	A_h
Density	ρ_f
Velocity	$\Omega_s l_h$
Enthalpy	$\frac{1}{\Delta i_{fg}} \frac{\Delta \rho}{\rho_g}$
Pressure	$\rho_f (\Omega_s l_h)^2$

Table 3.1. Scaling Variables in Dimensionless Analysis

called the “characteristic frequency of the phase change”, which is defined as follows:

$$\Omega_s = \Gamma_s \frac{\Delta \rho}{\rho_f \rho_g} \quad (3.45)$$

The channel heated height, l_h , is chosen as the length scale. Therefore, the hydraulic diameter, D_e , and the heated perimeter, ξ_h are scaled by l_h . Furthermore, the characteristic velocity becomes $\Omega_s l_h$, which can be noticed from Eq. (3.42). Therefore, the dimensionless channel inlet velocity is defined as follows:

$$v_{fin}^* = \frac{v_{fin}}{\Omega_s l_h} \quad (3.46)$$

The heated section flow area scales the area. The liquid enthalpy is scaled by using the latent heat and the density ratio. The dimensionless enthalpy definition includes the scaling these scaling parameters as follows:

$$N_s^* = \frac{i_{fs} - i}{\Delta i_{fg}} \frac{\Delta \rho}{\rho_g} \quad (3.47)$$

3.5.1 Dimensionless Governing Equations

Based on the scaling parameters introduced in the previous section, the governing equations listed in Section 3.4 can be transformed in to the dimensionless form. The solution of steady state single phase continuity equation yields to the inverse

of the Zuber number, which is one of the important dimensionless numbers in the stability analysis;

$$v_{fin,o}^* = \frac{v_{fin,o}}{\Omega_s l_h} = \frac{1}{N_{Zu}} \quad (3.48)$$

The single phase energy equation in dimensionless form is written as follows:

$$\frac{\partial N_s^*}{\partial t^*} + v_i^* \frac{\partial N_s^*}{\partial z^*} = -\Omega_{1\phi}^* \quad (3.49)$$

where $\Omega_{1\phi}^*$ is written in terms of the wall heat flux in the single phase heated section as follow:

$$\Omega_{1\phi}^* = \frac{q_{1\phi}'' \xi_h}{A_h \Delta i_{fg}} \frac{\Delta \rho}{\rho_f \rho_g} \frac{1}{\Omega_s}$$

For the solution of the single-phase energy equation in Eq. (3.49), the dimensionless boundary condition must be introduced at the channel inlet as

$$N_s^*(0, t^*) = N_{sin}(t^*) = \frac{i_{fs} - i_{fin}(t^*)}{\Delta i_{fg}} \frac{\Delta \rho}{\rho_g} \quad (3.50)$$

In order to locate the boiling boundary, the departure enthalpy is introduced. The departure enthalpy given by Eq. (3.25) can be made dimensionless as follows:

$$N_{sd}^* = \begin{cases} 0.0022 \frac{D_e^*}{\xi_h^*} \frac{1}{a_f^*} & N_{Pe} < 70000 \\ \frac{154}{(\xi_h l_h)^*} \frac{1}{v_{fin}^*} & N_{Pe} > 70000 \end{cases} \quad (3.51)$$

where $a_f^* = \frac{k_f}{\rho_f c_{pf}} \frac{1}{\Omega_s A_h}$ is the dimensionless liquid diffusivity, $(\xi_h l_h)^* = \frac{\xi_h l_h}{A_h}$ is the dimensionless heat transfer area.

The dimensionless single-phase momentum equation takes the following form,

$$-\frac{dP^*}{dz^*} = \frac{dv_{fin}^*}{dt^*} + N_f v_i^{*2} + \frac{N_{Fr}^{-1}}{N_{Zu}^2} \sin(\theta) + \frac{1}{2} K_i v_{fin}^{*2} \delta(z^*) \quad (3.52)$$

where $N_f = \frac{f_{1\phi} l_h}{2D_e}$, is the friction number, and $N_{Fr} = \frac{v_{fin,o}^2}{g l_h}$ is the Froude number.

In the two-phase mixture region, the mixture volumetric flux equation reduces to the following form

$$\frac{\partial j^*}{\partial z^*} = \Omega_{2\phi}^* \quad (3.53)$$

where $\Omega_{2\phi}^*$ is the dimensionless reaction frequency in the two-phase mixture region written in terms of the wall heat flux in this region. Based on the solution of this equation, the kinematic wave velocity in dimensionless form becomes

$$C_k^* = C_o j^* + \frac{N_d}{N_{Zu}} \quad (3.54)$$

where $N_d = \frac{\langle\langle v_{gj} \rangle\rangle}{v_{fin,o}}$ is the drift number.

The dimensionless density wave equation in terms of the modified density is written as follows:

$$\frac{\partial \rho_m^{+*}}{\partial t^*} + C_k^* \frac{\partial \rho_m^{+*}}{\partial z^*} = -C_o C_g \Omega_{2\phi}^* \quad (3.55)$$

The boundary condition for the density wave equation simply becomes $\rho_m^{+*}(\lambda^*, t^*) = 1$.

The dimensionless mixture momentum equation can be obtained by using the scaling parameter given in Table (3.1) from Eq. (3.43):

$$\begin{aligned} -\frac{dP^*}{dz^*} &= \rho_m^* \frac{\partial v_m^*}{\partial t^*} + \rho_m^* v_m^* \frac{\partial v_m^*}{\partial z^*} + C_m N_f \rho_m^* v_m^{*2} + \frac{N_{Fr}^{-1}}{N_{Zu}^2} \rho_m^* \sin(\theta) \\ &+ \frac{\partial}{\partial z^*} \left[\frac{1 - \rho_m^*}{\rho_m^*} \frac{N_\rho}{\rho_m^* - N_\rho} \bar{v}_{gj}^{*2} \right] + \frac{1}{2} K_e \rho_m^* v_m^{*2} \delta(z^* - 1) \end{aligned} \quad (3.56)$$

The dimensionless mixture velocity which is needed to integrate the momentum equation can be obtained via the following equation:

$$v_m^* = \frac{\rho_m^{+*}}{\rho_m^*} j^* - \frac{1 - \rho_m^*}{\rho_m^*} \frac{N_d}{N_{Zu}} \quad (3.57)$$

3.5.2 Dimensionless Numbers

In the previous section, the dimensionless form of the field equations have been obtained based on the given scaling variables. In this section, the definition and the physical significance of the dimensionless numbers appearing in the dimensionless equations are examined.

- Subcooling Number: The subcooling number appears as a boundary condition for the single-phase energy equation and incorporates the effect of the inlet subcooling into the analysis. As will be discussed later, it also quantifies the delay due to the propagation of the enthalpy wave in the single phase heated section

$$N_{sub} = \frac{\Delta i_{sub}}{\Delta i_{fg}} \frac{\Delta \rho}{\rho_g} \quad (3.58)$$

- Zuber Number: The Zuber number, or the phase change number, is another important dimensionless number in the stability analysis. It scales the phase change due to the heat addition. Along with the subcooling number, it shows the thermodynamic state within the channel. It is defined as follows:

$$N_{Zu} = \frac{Q}{\dot{m} \Delta i_{fg}} = \frac{\Omega_s l_h}{v_{fin,o}} \quad (3.59)$$

where Q is the total heat input to the flow, and \dot{m} is the mass flow rate through the channel.

- Froude Number: In the momentum equations given by Eqs. (3.52) and (3.56), the Froude number appears in the gravity term. It is the ratio of the inertia and gravity forces. The inverse of the Froude number scales the gravity and is the important scaling parameter in the natural circulation systems where flow is induced by gravity. The Froude number is defined as

$$N_{Fr} = \frac{v_{fin,o}^2}{gH} \quad (3.60)$$

- Friction Number: It demonstrates relative effect of the friction in the momentum equation.

$$N_f = \frac{f_{1\phi} H_h}{2D_e} \quad (3.61)$$

where $f_{1\phi}$ is the single-phase friction factor which depends on the Reynold number:

$$f_{1\phi} = C N_{Re}^m \quad (3.62)$$

In turbulent flow, $m = -0.25$ and $C = 0.184$. Since the constant multiplier is used for the two-phase friction factor, f_m , the friction number also scales the frictional forces in two-phase mixture region.

- Density Ratio Number: The density ratio number defined by Eq. (3.63) scales the system pressure. The density ratio number appears in the constitutive relation for C_o and the drift term in two-phase mixture momentum equation given by Eq. (3.56).

$$N_\rho = \frac{\rho_g}{\rho_f} \quad (3.63)$$

This number appears implicitly in the subcooling number and zuber number. Therefore, the pressure scaling is concealed in these numbers via N_ρ .

- Drift Number: It represents the relative importance of the mechanical equilibrium in the two-phase mixture. It is defined in terms of the void-weighted mean velocity,

$$N_d = \frac{\langle \langle v_{gj} \rangle \rangle}{v_{fin,o}} \quad (3.64)$$

Another parameter effecting the drift is the distribution parameter, C_o , which is already dimensionless. Therefore, along with C_o , the drift number reflects the mechanical non-equilibrium between the phases and the flow regime.

- Peclet Number: It appears in the departure enthalpy correlation of Saha-Zuber model. It is important scaling parameter in the modeling the effect of subcooled

boiling.

$$N_{Pe} = \frac{G_{c_{pf}}}{k_f} \quad (3.65)$$

- Reynolds Number: Reynolds number appears in single-phase friction factor. It is defined as

$$N_{Re} = \frac{\rho_f v_{fin,o} D_e}{\mu_f} \quad (3.66)$$

It is the ratio of the inertia and viscous forces, and it has little importance in scaling issue for the instabilities, since the Reynold number effect on the friction factor is small for the turbulent flow.

- Geometrical Dimensionless Groups: In addition to the dimensionless numbers described above, the dimensionless equations include parameters related to geometry of the system like dimensionless hydraulic diameter, $D_e^* = \frac{D_e}{H_h}$, inlet-flow-loss coefficient, K_{in} , exit-flow-loss coefficient, K_e , and sine of the channel orientation angle, $\sin(\theta)$.

4. FUEL HEAT CONDUCTION MODELING

Modeling of the heat conduction process in the nuclear fuel plays an important role in reactor design and safety analysis. Accurate description of temperature profile within the fuel element is necessary to predict lifetime of the fuel element and its safety characteristics. Thermal stress cracking, maximum allowable power rating and many other aspects of thermal design are directly related to the temperature distribution inside the fuel element.

The basic aspects of the fuel design described above can be analyzed based on the steady-state solution of the heat conduction equation in either one dimension or multi dimensions. However, in most cases, a transient solution of the process is necessary. Especially, during accident conditions such as LOCA, maximum cladding temperature depends on the solution of the heat conduction equation (generally in two dimensions) along with the coolant side conditions.

In the BWR technology, the fuel heat conduction process is important not only for accidental conditions but also for transients such as nuclear-coupled flow oscillations. Actually, the process provides the link between the neutronic (heat generation inside the fuel) and heat transferred to the coolant. The time required for the conduction of heat through the fuel element (fuel time constant) plays a central role in the stability analysis, because it gives the time lag effect between the heat generation and heat flux to the coolant. Even though BWRs have negative void-reactivity coefficients, under certain frequencies of oscillations, they might have positive void-reactivity coefficients in terms of coolant heat flux, which may amplify the oscillations' amplitude and worsen the instability.

All of the Light Water Reactors (LWRs) have similar fuel element design except some changes in assembly design, geometry and material. A typical BWR fuel element

consists of UO_2 fuel pellet enclosed within Zircaloy-2 cladding. There is an initial gap between the pellet and the cladding that is filled with inert helium gas. After a few days of operation, this gap is closed due to expansion of the pellet and thermal cracking on the surfaces. In addition, some fission product gases, such as Krypton and Xenon, escape from the fuel pellet and go to the gap region. The prediction of the characteristics of the gap conductance is a complex task and empirical correlations based on extensive experimental database are used.

As will be described in the following sections, an accurate description of the heat conduction process and the temperature distribution can be determined by solving the parabolic heat conduction equation. This is basically done by an appropriate numerical method. In this study, several simplified models are introduced to predict both the steady-state and transient characteristics of the fuel element temperature. This study has been performed to construct a tractable model for two-phase flow instabilities in BWR systems.

Based on the simplified models developed in this study, expressions for the fuel element time constant are derived. One objective is to appreciate the order of magnitude of this parameter and to analyze several effects such as the temperature-dependent conductivity and non-uniform heat generation, etc., in the process. The other objective is to derive dimensionless groups for the heat conduction process and examine the effects of the modeling strategy. For the purpose of analysis, the frequency domain analysis has been performed based on a linearized conduction equation. Transfer functions have been derived and analyzed for several important links among processes, namely heat generation, heat conduction, and coolant side effects.

The dimensionless analysis carried out in this chapter yields important dimensionless groups for the wall heat flux simulation. Since the SBWR fuel element has a fuel time constant larger than that of the electric heater used in the test section of the experimental loop as described in Chapter 8, the delay due to the heat conduction process should be simulated in the facility based on the dimensionless groups derived for the heat conduction through the fuel element.

4.1 Heat Conduction in Fuel Element

The temperature distribution within the fuel elements depends on the heat generation rate, material thermo-physical properties, and coolant conditions. In general, the heat conduction process is governed by the following solid energy equation:

$$\rho c \frac{\partial T}{\partial t} = \nabla \cdot k(T) \nabla T(\vec{r}, t) + Q'''(\vec{r}, t) \quad (4.1)$$

where ρc is the volumetric heat capacity of the solid. This equation, which is a parabolic type, can be solved numerically with given initial and boundary conditions along with the number of dimensions required for the problem considered. In general, one-dimensional form is appropriate for adequate description of the phenomenon. Two important parameters in Eq. (4.1) are the thermal conductivity, $k(T)$, and heat generation rate, $Q'''(\vec{r}, t)$. In the fuel pellet, because of its low thermal conductivity, a steep temperature gradient exists. However, the thermal conductivity of UO_2 changes significantly with temperature. Another complexity of the problem is that the heat generation term depends on space, the fuel temperature and material properties. The thermal neutron flux distribution determines the rate and spatial distribution of the heat generation inside the pellet. The heat transfer out of the fuel element via convection is also a strong function of the coolant side conditions. Therefore, the process is extremely complex and nonlinear.

A typical BWR fuel element cross section is shown in Figure 4.1. In most cases; except the reflood calculations in LOCA, the axial conduction is negligible compared to the heat conduction in radial direction. This is justified by the very small D/L ratio of the fuel rod. Therefore, the one-dimensional form of Eq. (4.1) can be used,

$$\rho c \frac{\partial T}{\partial t} = \frac{1}{r} \frac{\partial}{\partial r} \left(k(T) r \frac{\partial T}{\partial r} \right) + Q'''(r, t) \quad (4.2)$$

Complications due to the temperature-dependent thermal conductivity, complex heat generation term and non-linear boundary conditions make the analytical solution impossible. However, under certain simplified assumptions, some analytical

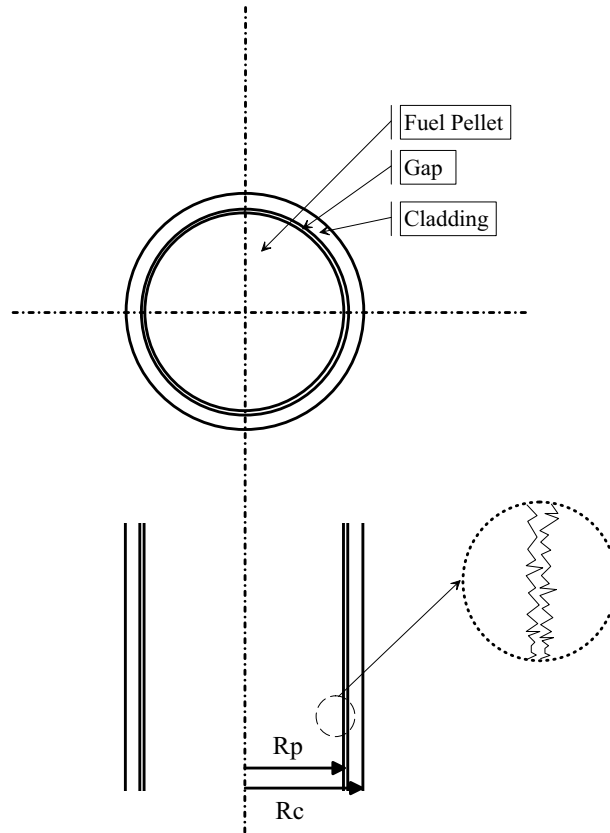


Figure 4.1. Typical BWR Fuel Element

expressions can be derived. Before proceeding further, necessary boundary conditions should be supplied. Even though there are three different zones in a fuel element cross section, equations are derived for only two regions, namely the fuel pellet (p) and the cladding (c). As it will be described below, the gap is practically closed after a few days of operations. As shown in Figure 4.1, protrusions are created especially on the pellet outer surface, and there are many contact points between the pellet and the cladding. Thermal expansion coefficient of the fuel pellet and the cladding is also different. For instance, the coefficient for the fuel pellet is approximately two times greater than that of the cladding. This is another reason for the gap closure. However, there is significant temperature drop within this region that should be taken into account. The amount of temperature drop is determined based on “Gap Heat Transfer Coefficient (h_g)”, which is an experimentally determined parameter and depends on

the thermal conductivity of gases, size of protrusions, burnup level, etc. This region is taken into account as thermal contact resistance. Applicable boundary conditions are given in Eq. (4.3) as

$$\begin{aligned} \left. \frac{\partial T}{\partial r} \right|_{r=0} &= 0 \\ -k_p \left. \frac{\partial T}{\partial r} \right|_{r=R_p^-} &= h_g (T(R_p^-) - T(R_p^+)) = h_g \Delta T_g \\ -k_c \left. \frac{\partial T}{\partial r} \right|_{r=R_c} &= h_\infty (T(R_c) - T_\infty) \end{aligned} \quad (4.3)$$

where k_p and k_c are the thermal conductivity of the pellet and clad, respectively; h_∞ denotes the coolant heat transfer coefficient, and T_∞ is the bulk coolant temperature. $T(R_p^-)$ represents the temperature on the pellet outer surface, and $T(R_p^+)$ represents the clad inner surface temperature. Therefore, $\Delta T_g = T(R_p^-) - T(R_p^+)$ is the temperature drop across the gap region. The first boundary condition given by Eq. (4.3) is for centerline symmetry of temperature at the pellet center. The second boundary condition is for the gap temperature drop and the last one accounts for convective boundary condition at the cladding wall, which requires the coolant side temperature, T_∞ and heat transfer coefficient, h_∞ . However, in addition to the boundary conditions, the heat generation term in Eq. (4.2) should also be given for the solution. For the purpose of this analysis, time and space separability is assumed to specify the heat generation term. As it will be described in Chapter 5, this assumption is the starting point of the derivation of the Point Kinetic Model (PKM). By considering the radial power shape inside the fuel pellet, the following equation is used to describe position- and time-dependent volumetric heat generation term:

$$Q'''(r, t) = \langle Q_o''' \rangle n(t) \phi(r) \quad (4.4)$$

where $\langle Q_o''' \rangle$ is the area-averaged volumetric heat generation rate at steady-state, $n(t)$

is the neutron amplitude function, which can be determined from the PKM equations, and $\phi(r)$ is the shape function that characterizes the spatial distribution of the thermal neutrons inside the pellet. In this analysis, the power shape is normalized such that,

$$\frac{2}{R_p^2} \int_0^{R_p} \phi(r) r dr = 1 .$$

Therefore, the area-averaged volumetric heat generation under steady-state conditions can be determined from the following equation:

$$\langle Q_o''' \rangle = \frac{\int_0^{R_p} Q_o'''(r) r dr}{\int_0^{R_p} \phi(r) r dr} . \quad (4.5)$$

The amount of heat generation and its spatial distribution depend on the thermal neutron flux. The neutron flux, in turn, depends on the fuel composition, temperature, and coolant density. As far as the spatial power shape within the fuel pellet is concerned, a parameter called “Flux Depression Factor”, denoted by ζ , determines the effect of the power profile tilting inside the pellet. The thermal neutron flux is higher inside the coolant and lower inside the pellet. This is because of the fact that neutrons are generated inside the fuel as fast neutrons and they are thermalized in the moderator/coolant region. Therefore, the thermal neutrons, which cause most part of the fission, enter the fuel from the moderator side. Since both U^{235} and U^{238} atoms have high absorption cross sections, more of the thermal neutrons are absorbed at the periphery of the fuel pellet. This effect causes the inner region of the fuel pellet to be shielded against thermal neutrons. Therefore, because of this self-shielding effect, the power generation in the pellet is higher at the periphery. The non-uniform power shape changes the time lag characteristics of the fuel heat conduction and causes the fuel time constant of the fuel element smaller than that of the uniform power profile case.

For the purpose of this study, a parabolic power shape is considered for the radial power shape, $\phi(r)$ to account for the self-shielding effect. The power profile is

given by

$$\phi(r) = 1 + \left[\left(\frac{r}{R_p} \right)^2 - \frac{1}{2} \right] f, \quad (4.6)$$

where f is an adjustable parameter to account for the effect of the flux depression factor, ζ , which is defined as the ratio of the power generation at the pellet periphery and pellet center:

$$\zeta = \frac{\phi(0)}{\phi(R_p)} \quad (4.7)$$

Therefore, the parameter, f , can be written as a function of the flux depression factor as

$$f = \frac{2(1 - \zeta)}{1 + \zeta} \quad (4.8)$$

The flux depression factor is characterized by the neutron flux distribution inside the fuel pellet. It can be calculated via a neutron transport code for a given cell geometry and composition profile.

4.2 Steady-state Temperature Distribution and Thermal Resistances

The steady-state temperature distribution inside the fuel element is determined with given boundary conditions. Thermal resistances in different zones of the fuel element are derived based on the solution of the steady-state heat conduction equation given by Eq. (4.2). In the derivation of the thermal resistance expressions and the simplified models used for the fuel heat conduction, area-averaging over the fuel pellet and cladding is performed. Therefore, the problem is formulated based on two different regions, namely fuel pellet and cladding. For the fuel pellet, power profile-weighted area-averaging is employed to accommodate the effect of the power profile on the fuel time constant. The power profile-weighted area-averaged temperature for the fuel pellet is given as follows:

$$\langle\langle T \rangle\rangle_p \triangleq \frac{\langle T(r)\phi(r) \rangle_p}{\langle \phi(r) \rangle} = \frac{2}{R_p^2} \int_0^{R_p} T(r)\phi(r)rdr \quad (4.9)$$

$$\langle\langle T \rangle\rangle_p \longleftrightarrow T(R_p^-) \longleftrightarrow T(R_p^+) \longleftrightarrow \langle T \rangle_c \longleftrightarrow T(R_c) \longleftrightarrow T_\infty$$

Figure 4.2. Heat Conduction Network for the Fuel Element based on Averaged Temperatures

Similar to Eq. (4.9), the average clad temperature is defined as

$$\langle T \rangle_c = \frac{1}{A_c} \iint_{A_k} T(r) dA = \frac{2}{R_c^2 - R_p^2} \int_{R_p}^{R_c} T(r) r dr \quad (4.10)$$

In the following sections, the steady-state temperature distribution for each region (pellet and clad) and thermal resistances are derived. The heat transfer network shown in Figure 4.2 is the basic scheme in the derivation of the resistances and the simplified models for the fuel heat conduction.

4.2.1 Pellet Region

The steady-state form of Eq. (4.2) can be solved for the pellet by introducing the pellet outer surface temperature, $T(R_p^-)$, as a boundary condition. By considering the temperature-dependent thermal conductivity of UO_2 , the following equation can be written for the general solution of the steady-state temperature distribution inside the pellet:

$$\int_{T(R_p^-)}^{T(r)} k(T) dT = \langle Q''' \rangle R_p^2 \left[\frac{1 - r'^2}{4} - \left(\frac{r'^2 - 1}{4} \right)^2 f \right] \quad (4.11)$$

where $r' = \frac{r}{R_p}$. The integral on the left-hand-side of Eq. (4.11) is called “Conductivity Integral” and can be evaluated with a given “ $k(T)$ ”. The thermal conductivity of the UO_2 pellet shown in Figure 4.3 is given by a correlation based on extensive database [37]. As seen from the figure, the pellet thermal conductivity is a strong function of the temperature. However, the pellet thermal conductivity depends on many other factors besides temperature, such as irradiation due to composition change and porosity [38].

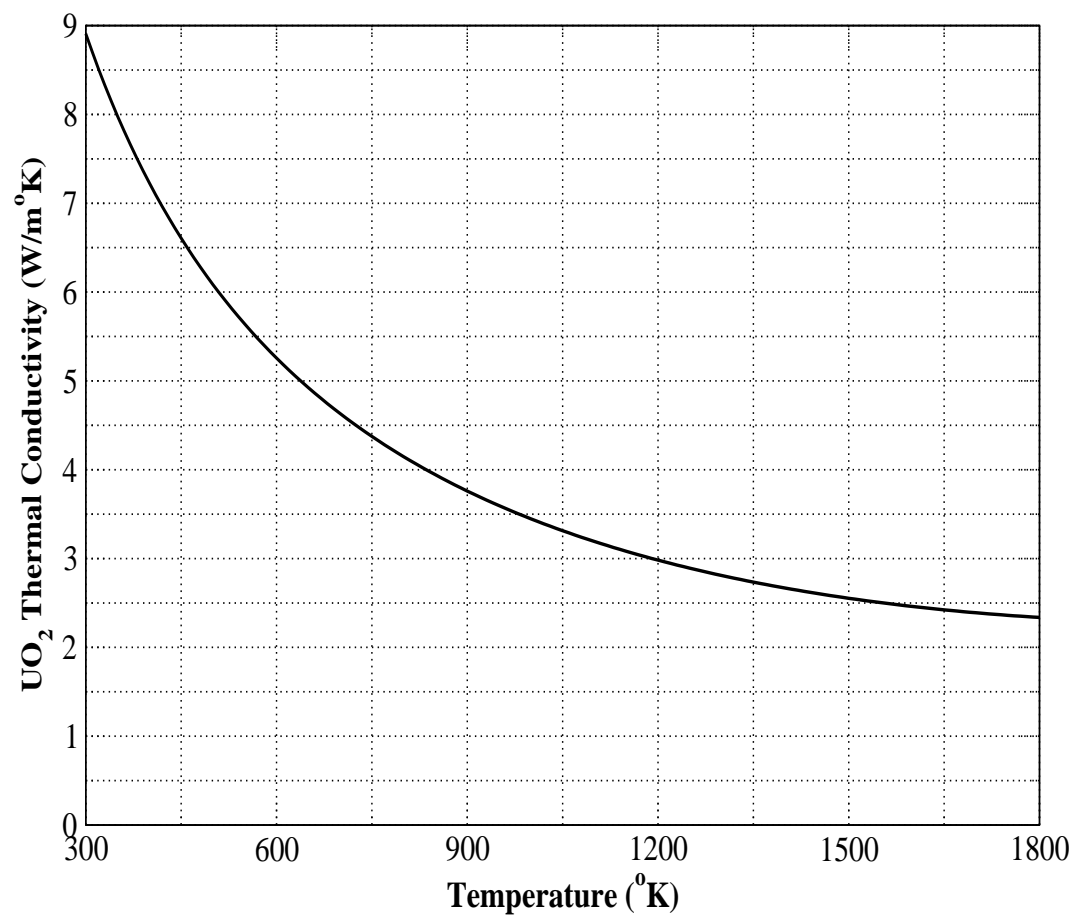


Figure 4.3. Thermal Conductivity of UO_2 Pellet

The temperature distribution given by Eq. (4.11) requires an iterative process. For simplicity, an averaged value for the pellet thermal conductivity is used. Based on the minimum and maximum temperature inside the pellet during the transient, T_{min}, T_{max} , following equation can be written for the average thermal conductivity of the pellet,

$$\bar{k}_p = \frac{1}{T_{max} - T_{min}} \int_{T_{min}}^{T_{max}} k(T) dT \quad (4.12)$$

By introducing the averaged-thermal conductivity of the pellet, following equation for the pellet steady-state temperature distribution can be written from Eq. (4.11),

$$T_p(r) = T(R_p^-) + \frac{\langle Q' \rangle}{\pi \bar{k}_p} \left[\frac{1 - r'^2}{4} - \left(\frac{r'^2 - 1}{4} \right)^2 f \right] \quad (4.13)$$

where $\langle Q' \rangle = \pi R_p^2 \langle Q''' \rangle$ is the area-average linear heat rate for the fuel element. By using the definition of power profile-weighted area-averaging given by Eq. (4.9), the average temperature drop across the fuel pellet is given as follows,

$$\langle \langle T \rangle \rangle_p - T(R_p^-) = \langle Q' \rangle \frac{f^2 - 8f + 24}{192\pi \bar{k}_p} \quad (4.14)$$

The conductive thermal resistance for the fuel pellet, R'_1 , based on the average temperature drop given by Eq. (4.14) can be written as follows

$$R'_1 \triangleq \frac{f^2 - 8f + 24}{192\pi \bar{k}_p} \quad (4.15)$$

In general, the thermal resistance, R' , is defined as follows

$$R' = \frac{\Delta T}{\langle Q' \rangle} \quad (4.16)$$

which is given in terms of the linear heat rate. Therefore, R' has unit $\frac{m^\circ K}{W}$.

4.2.2 Gap and Cladding Regions

As described in Section 4.1, the gap region is practically closed after few days of operation. Therefore, it is reasonable to treat this region as a contact thermal resistance given in terms of gap heat transfer coefficient, h_g . The determination of the gap heat transfer coefficient is quite complicated and difficult to develop an analytical model. The current approach for the gap conductance problem is to treat the gap conductance as a contact resistance between two solids (pellet and clad) including the effect of protrusions, fission gas release rate and its content. The detailed analysis for the gap conductance is given by Ref. [39, 40]. In the current study, the value of 5700 W/m²K for the gap heat transfer coefficient is used as recommended for design calculations [41].

As shown in Eqs. (4.3), the linear heat rate can be written in terms of gap heat transfer coefficient, h_g , and gap temperature drop, $\Delta T_g = (T(R_p^-) - T(R_p^+))$ as follows,

$$\langle Q' \rangle = 2\pi R_p h_g (T(R_p^-) - T(R_p^+)) . \quad (4.17)$$

From the definition of the thermal resistance given by Eq. (4.16), the gap region thermal resistance, R'_2 is given by

$$R'_2 \triangleq \frac{1}{2\pi R_p h_g} . \quad (4.18)$$

The steady-state heat conduction equation for the cladding can be obtained by dropping the heat generation term in Eq. (4.2). During normal operation, certain amount of heat is also deposited inside the cladding due to the γ -ray attenuation, however this is negligible compared to the heat generation inside the pellet, therefore, it is simply neglected.

As shown in Figure 4.2, two separate thermal resistance expressions are derived for the cladding. This can be achieved by solving the conduction equation with the clad inner surface temperature, $T(R_p^+)$, and the clad outer surface temperature, $T(R_c)$, as boundary conditions. Therefore, two different forms of the clad temperature

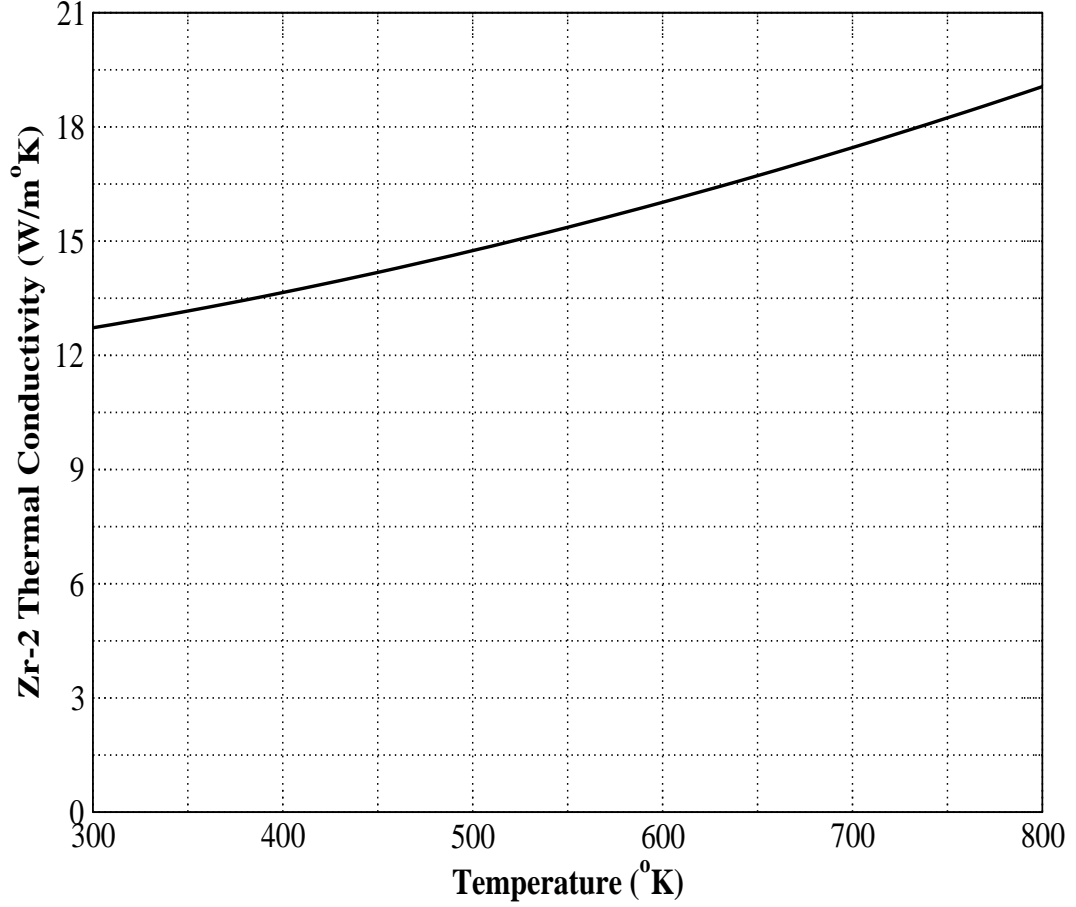


Figure 4.4. Thermal Conductivity of Zr2 Cladding

distribution are derived. By means of clad inner surface temperature as a boundary condition, the following equation is written for the clad,

$$T_c(r) = T(R_p^+) - \frac{\langle Q' \rangle}{2\pi \bar{k}_c} \ln \left(\frac{r}{R_p} \right) \quad (4.19)$$

where \bar{k}_c is the average thermal conductivity of the clad. The effect of temperature on the thermal conductivity should also be considered for Zircaloy-2. However, the effect is not as significant as that in UO_2 thermal conductivity. The linear dependency can be easily assumed as can be seen from Figure 4.4. The correlation for the Zircaloy-2 thermal conductivity used in the figure was developed by Scott [42].

The average temperature drop, $T(R_p^+) - \langle T \rangle_c$, in the clad can be determined by applying area averaging defined via Eq. (4.10). The thermal resistance corresponding to the temperature drop, $T(R_p^+) - \langle T \rangle_c$, can be written by means of Eq. (4.16) as follows,

$$R'_3 \triangleq \frac{1}{2\pi\bar{k}_c} \left[\frac{R_c^2}{R_c^2 - R_p^2} \ln \left(\frac{R_c}{R_p} \right) \frac{1}{2} \right] \quad (4.20)$$

The temperature profile can also be determined by introducing the boundary condition on the clad outer surface. Therefore, by using the clad outer surface temperature (wall temperature), $T(R_c)$, the distribution is given as

$$T_c(r) = T(R_c) + \frac{\langle Q' \rangle}{2\pi\bar{k}_c} \ln \left(\frac{R_c}{r} \right) \quad (4.21)$$

The second thermal resistance of the clad for the temperature drop, $\langle T \rangle_c - T(R_c)$, is determined after area-averaging and by using the definition of the thermal resistance as follows,

$$R'_4 \triangleq \frac{1}{2\pi\bar{k}_c} \left[\frac{1}{2} - \frac{R_p^2}{R_c^2 - R_p^2} \ln \left(\frac{R_c}{R_p} \right) \right] \quad (4.22)$$

4.2.3 Convective Resistance of the Coolant

Based on the temperature difference between the clad outer surface temperature, $T(R_c)$, and the bulk coolant temperature, T_∞ , the resistance for the convective heat transfer between the clad and coolant is given by

$$R'_5 \triangleq \frac{1}{2\pi R_c h_\infty} \quad (4.23)$$

where h_∞ is the heat transfer coefficient of the coolant. Since its functional dependency on flow conditions differs depending on whether the flow is single phase or two-phase, two different flow conditions should be examined separately.

In the single phase flow, the heat transfer coefficient is written as a function of the Reynolds and Prandtl numbers. Neglecting the pressure dependency on the flow conditions, the heat transfer coefficient in single phase flow, $h_{1\phi}$, is written as a

Table 4.1. Coefficient of Eq. (4.27) for Different Correlations

	$\kappa(P)(10^6)$	m
Jens and Lottes	$\frac{\exp(4P/6.2)}{25^4}$	3
Thom	$\frac{\exp(2P/8.7)}{22.7^4}$	1

function of liquid velocity through the Reynolds number. The Reynolds number is defined as

$$N_{Re} \triangleq \frac{\rho_f v_f D_e}{\mu_f} \quad (4.24)$$

where ρ_f and μ_f are the liquid density and viscosity, respectively. v_f is the liquid velocity and D_e is the equivalent hydraulic diameter of the flow channel. The heat transfer coefficient in single phase flow can be determined from Dittus-Boelter correlation [43],

$$h_{1\phi} = 0.023 \frac{k_f}{D_h} N_{Re}^{0.8} N_{Pr}^{0.4} \quad (4.25)$$

where k_f is the liquid thermal conductivity and D_h is the heated diameter calculated based on heated perimeter of the heated channel. N_{Pr} is the Prandtl number given by

$$N_{Pr} \triangleq \frac{\nu_f}{a_f} \quad (4.26)$$

where ν_f and a_f are the momentum and thermal diffusivity of the liquid, respectively.

In two-phase flow, the heat transfer coefficient is determined based on given heat transfer regime. In general, nucleate boiling heat transfer dominates. The general form of the heat transfer coefficient is given as a function of pressure, P , and wall

superheat, $\Delta T_w = T(R_c) - T_s$, as

$$h_{2\phi} = \kappa(P)\Delta T_w^m \quad (4.27)$$

The saturation temperature, T_s , at given pressure is considered as the bulk coolant temperature in the two-phase flow.

For the purpose of the analysis, two correlations for the nucleate boiling are highlighted: Jens and Lottes [44] and Thom [45] correlations. Table 4.1 summarizes the coefficients of Eq. (4.27) for those two correlations.

4.3 Simplified Models for Fuel Heat Conduction

In this section, simplified models for predicting the transient behavior of the fuel heat conduction process are derived. The partial differential equations given by Eq. (4.2) is transformed into two ordinary differential equations for the pellet and cladding regions by introducing the area averaging over each region of the fuel element. Two alternative models are presented in this study: One is “Double-Node Lumped Model”, which considers the fuel pellet and clad separately; While the other method, called “Single-Node Lumped Model”, is the result of lumping the pellet and cladding regions into one, which is called “fuel element”.

As shown in Figure 4.2, there are five thermal resistances along the heat flow path. Since ordinary differential equations are written for power profile-weighted area-averaged pellet temperature and area-averaged clad temperature, two separate heat conductances are defined:

$$U'_{pc} \triangleq \frac{N_{rod}}{R'_1 + R'_2 + R'_3} \quad (4.28)$$

which considers the heat flow from the fuel pellet to the clad. The conductance from the cladding to the coolant is given by

$$U'_{c\infty} \triangleq \frac{N_{rod}}{R'_4 + R'_5} \quad (4.29)$$

where N_{rod} is the number of fuel rods in the reactor core. R'_1 is the pellet resistance (Eq. (4.15)); R'_2 is the gap resistance (Eq. (4.18)); R'_3 is the resistance of the inside half of the cladding (Eq. (4.20)); R'_4 is the resistance for the outside half of the cladding (Eq. (4.22)); and R'_5 is the convective resistance of the coolant (Eq. (4.23)).

4.3.1 Double-Node Lumped Model

The one-dimensional form of the heat conduction equation given by Eq. (4.2) can be integrated over each region to obtain the coupled ordinary differential equations for the fuel pellet and the clad. The following equations can be obtained for the double-node lumped model: The pellet region:

$$\langle \rho c \rangle_p A_p \frac{d\langle T \rangle_p}{dt} = \langle Q'_o \rangle n(t) - U'_{pc} (\langle T \rangle_p - \langle T \rangle_c) \quad (4.30a)$$

and the cladding region:

$$\langle \rho c \rangle_c A_c \frac{d\langle T \rangle_c}{dt} = U'_{pc} (\langle T \rangle_p - \langle T \rangle_c) - U'_{c\infty} (\langle T \rangle_c - T_\infty) \quad (4.30b)$$

where $\langle \rho c \rangle_p$ and $\langle \rho c \rangle_c$ are the volumetric heat capacity of the pellet and clad, respectively. $A_p = N_{rod} \pi R_p^2$ is the total fuel pellet cross sectional area, and $A_c = N_{rod} \pi (R_c^2 - R_p^2)$ is the total clad cross sectional area. Equations (4.30a) and (4.30b) are integral energy balance equations inside each region, considering energy production, transfer and storage terms. Since they are ordinary differential equations in time domain, the solution requires initial temperatures for each region. The initial conditions are given as

$$\langle T \rangle_{p,o} = T_{\infty,o} + \langle Q'_o \rangle \frac{U'_{pc} + U'_{c\infty}}{U'_{pc} U'_{c\infty}} \quad (4.31a)$$

$$\langle T \rangle_{c,o} = T_{\infty,o} + \frac{\langle Q'_o \rangle}{U'_{c\infty}} \quad (4.31b)$$

4.3.2 Single-Node Lumped Model

Single-node lumped model can be obtained by integrating the energy equation over the entire cross-sectional area of the fuel element, including the pellet and cladding. The area-averaged fuel element temperature for which the single-node lumped model is derived is written in terms of power profile-weighted area-averaged pellet temperature, $\langle\langle T \rangle\rangle_p$, and area-averaged clad temperature, $\langle T \rangle_c$:

$$\langle T \rangle_{fe} = \frac{A_p}{A_{fe}} \langle\langle T \rangle\rangle_p + \frac{A_c}{A_{fe}} \langle T \rangle_c \quad (4.32)$$

where $A_{fe} = A_p + A_c = N_{rod} \pi R_c^2$ is the total fuel element cross sectional area. Therefore, the differential equation for the area-averaged fuel element temperature is written as follows:

$$\langle \rho c \rangle_{fe} A_{fe} \frac{d\langle T \rangle_{fe}}{dt} = \langle Q'_o \rangle n(t) - U' (\langle T \rangle_{fe} - T_\infty) \quad (4.33)$$

where U' is the overall heat conductance which is derived based on the area averaging as follows,

$$U' = \frac{N_{rod}}{\frac{A_p}{A_{fe}} (R'_1 + R'_2 + R'_3) + R'_4 + R'_5} \quad (4.34)$$

The area-averaged volumetric heat capacity of the fuel element, $\langle \rho c \rangle_{fe}$, is given as,

$$\langle \rho c \rangle_{fe} = \frac{\langle \rho c \rangle_p A_p + \langle \rho c \rangle_c A_c}{A_p + A_c} \quad (4.35)$$

The initial condition required for the solution of Eq. (4.33) is given as follows:

$$\langle T \rangle_{fe,o} = T_{\infty,o} + \frac{Q'_o}{U'} \quad (4.36)$$

4.4 Fuel Heat Conduction Time Constant

The conduction of the heat across the fuel element requires a certain amount of time which is characterized by a time constant. A typical BWR fuel element has the time constant of four to six seconds. The time constant is one of the fundamental parameter in the stability analysis of the nuclear-coupled density wave oscillations. Depending on the frequency of the flow oscillations, the oscillations in the void and the heat flux may be in-phase, which results in positive void coefficient in terms of heat flux to the coolant.

In this section, based on the developed models in Section 4.3, expressions for the fuel time constant of a typical fuel element are derived.

By using the double-node lumped model, Eqs. (4.30a) and (4.30b) can be written in matrix-vector form as

$$\frac{d}{dt} \left(\langle \vec{T} \rangle \right) = A \langle \vec{T} \rangle + \vec{b}, \quad (4.37)$$

where vector $\langle \vec{T} \rangle = [\langle \langle T \rangle \rangle_p \quad \langle T \rangle_c]^T$. The matrix A, which is used for the time constant determination, is written as

$$A = \begin{pmatrix} -\frac{U'_{pc}}{\langle \rho c \rangle_p A_p} & \frac{U'_{pc}}{\langle \rho c \rangle_p A_p} \\ \frac{U'_{pc}}{\langle \rho c \rangle_c A_c} & -\frac{U'_{pc} + U'_{c\infty}}{\langle \rho c \rangle_c A_c} \end{pmatrix}. \quad (4.38)$$

Transient characteristics of the conduction process can be determined by analyzing the eigenvalues of the matrix in Eq. (4.37). The characteristic equation of this matrix is a second order polynomial, which is written as

$$p(\lambda) = \det(A - \lambda I) = \lambda^2 + p_1 \lambda + p_2 = 0, \quad (4.39)$$

where the coefficients are

$$p_1 = \frac{U'_{pc}}{\langle \rho c \rangle_p A_p} + \frac{U'_{pc} + U'_{c\infty}}{\langle \rho c \rangle_c A_c} \quad (4.40a)$$

and

$$p_2 = \frac{U'_{pc} U'_{c\infty}}{\langle \rho c \rangle_c A_c \langle \rho c \rangle_p A_p} \quad (4.40b)$$

As can be seen from Eqs. (4.40), both coefficients (p_1 and p_2) are positive. Therefore, the roots of Eq. (4.39) have the same signs. In addition, the discriminant, $\Delta = p_1^2 - 4p_2$, is always greater than zero, assuring that the following two roots are real:

$$\lambda_1 = -\frac{p_1}{2} \left[1 + \left(1 - \frac{4p_2}{p_1^2} \right)^{1/2} \right] \quad (4.41a)$$

$$\lambda_2 = \frac{p_1}{2} \left[\left(1 - \frac{4p_2}{p_1^2} \right)^{1/2} - 1 \right] \quad (4.41b)$$

The second root that is the smallest in magnitude determines the transient characteristics dominantly. Therefore, the fuel time constant is the inverse of the second root, given by

$$\tau_F = \frac{2}{p_1 \left[\left(1 - \frac{4p_2}{p_1^2} \right)^{1/2} - 1 \right]}. \quad (4.42)$$

The second approach for determining the fuel time constant is to derive expressions from the single-node lumped model. From the ordinary differential equation written for the average fuel element temperature, the fuel time constant expression becomes

$$\tau_F = \left(\langle \rho c \rangle_p A_p + \langle \rho c \rangle_c A_c \right) \frac{\left(\frac{A_p}{A_{fe}} \right) U'_{c\infty} + U'_{pc}}{U'_{pc} U'_{c\infty}}. \quad (4.43)$$

4.5 Dimensional Analysis and Transfer Functions for Fuel Heat Conduction

In the previous sections, the simplified models for the fuel heat conduction process in a typical BWR fuel element have been derived. Applying area averaging to the one-dimensional heat conduction equation in cylindrical geometry, two ordinary differential equations are derived for the power profile-weighted area-averaged fuel pellet temperature and area-averaged clad temperature. The model is further simplified by lumping the pellet and cladding region into one single region.

In this section, a detailed dimensional analysis is performed. By introducing appropriate form of the scaling variables, the model equations are non-dimensionalized. The problem is transformed into frequency domain by linearizing and applying Laplace transformation on Eq. (4.33). The frequency domain analysis provides the transfer functions that link the heat generation and wall heat flux. Based on the derived transfer function for the fuel heat conduction process, several dimensionless numbers are emphasized for the modeling of heat conduction delay in the void-reactivity feedback simulation experiments.

4.5.1 Scaling Variables and Dimensionless Conduction Equations

Essence of dimensional analysis is based on the definition of appropriate scaling variables. The scaling variables are chosen in such a way that they are consistent with the flow-field dimensionless analysis described in Ref. [46]. The following list describes the scaling variables for each dimension appearing in the model formulation:

- I. Time: Inverse of the reaction frequency in saturated two-phase flow, Ω_o , is chosen for time scale. The reaction frequency at steady-state conditions is defined as

$$\Omega_o = \frac{\langle Q'_o \rangle}{A \Delta i_{fg}} \frac{\Delta \rho}{\rho_f \rho_g} \quad (4.44)$$

where

$\langle Q'_o \rangle \triangleq$ Linear heat rate at steady-state [W/m]

$\Delta\rho \triangleq$ Density difference between liquid and vapor at saturation [kg/m³]

$A \triangleq$ Channel Flow Area [m²]

$\Delta i_{fg} \triangleq$ Latent heat of vaporization [J/kg]

$\Omega_o \triangleq$ Reaction Frequency at steady-state [1/sec]

Therefore, the dimensionless time is defined as

$$t^* = t\Omega_o \quad (4.45)$$

The dimensionless fuel time constant determined from the single-node lumped model is written as

$$\tau_F^* = \frac{\langle \rho c \rangle_{fe} A_{fe}}{U'} \Omega_o \quad (4.46)$$

The term $\frac{U'}{\langle \rho c \rangle_{fe}}$, denoted by a_{fe} is considered as pseudo thermal diffusivity which is the integral quantity of the fuel element. Similarly, pseudo thermal diffusivity for the pellet and cladding can be written as follows,

$$a_p = \frac{U'_{pc}}{\langle \rho c \rangle_p} \quad a_c = \frac{U'_{c\infty}}{\langle \rho c \rangle_c} \quad (4.47)$$

II. Area: The transverse length scale is lost due to the area-averaging in the radial direction. The area scale is chosen to be the channel flow area as it is consistent with flow field scaling. Therefore, the dimensionless cross sectional area of the pellet and cladding becomes,

$$A_p^* = \frac{A_p}{A} \quad A_c^* = \frac{A_c}{A} \quad (4.48)$$

where subscripts p and c stand for the pellet and cladding regions, respectively.

III. Volumetric Heat Capacity: The volumetric heat capacity of each region is scaled by the saturated liquid heat capacity, $\rho_f c_{pf}$:

$$\langle \rho c \rangle_p^* = \frac{\langle \rho c \rangle_p}{\rho_f c_{pf}} \quad \langle \rho c \rangle_c^* = \frac{\langle \rho c \rangle_c}{\rho_f c_{pf}} \quad (4.49)$$

IV. Reaction Frequency: The reaction frequency, Ω , depends on whether the flow is single phase or two-phase. The transient reaction frequency for the single phase and two-phase flows is defined in terms of the linear heat rate, $\langle Q' \rangle$, in each flow region as follows:

$$\Omega_{1\phi} = \frac{\langle Q'_{1\phi} \rangle}{A \Delta i_{fg}} \frac{\Delta \rho}{\rho_f \rho_g} \quad \Omega_{2\phi} = \frac{\langle Q'_{2\phi} \rangle}{A \Delta i_{fg}} \frac{\Delta \rho}{\rho_f \rho_g} \quad (4.50)$$

The linear heat rate in each flow conditions is written as follows,

$$\langle Q' \rangle = U'_{\infty} \left(\langle T \rangle_c - T_{\infty} \right) \quad (4.51)$$

where the heat conductance, U'_{∞} , and the bulk coolant temperature T_{∞} change depending on the flow condition as described in Section 4.2.3. Equation (4.51) is written based on the area-averaged clad temperature. However, a similar expression can be written based on the single-node lumped model by replacing U'_{∞} with U' and $\langle T \rangle_c$ with $\langle T \rangle_{fe}$. It is important to note that U'_{∞} and U' are both a function of the heat transfer coefficient of the coolant, h_{∞} , which is time dependent. Based on the definitions given by Eq. (4.50), the dimensionless transient reaction frequency for each phase is given by

$$\Omega_{1\phi}^* = \frac{\Omega_{1\phi}}{\Omega_o} \quad \Omega_{2\phi}^* = \frac{\Omega_{2\phi}}{\Omega_o} \quad (4.52)$$

V. Temperature: The dimensionless temperature for the pellet and cladding is de-

defined as follows,

$$\theta_p^* \triangleq \frac{c_{pf} \left(\langle \langle T \rangle \rangle_p - T_s \right) \Delta \rho}{\Delta i_{fg} \rho_g} \quad \theta_c^* \triangleq \frac{c_{pf} \left(\langle T \rangle_c - T_s \right) \Delta \rho}{\Delta i_{fg} \rho_g} \quad (4.53)$$

where T_s is the saturation temperature of the coolant at a given system pressure. The definition of the dimensionless temperatures given in Eq. (4.53) is similar to the dimensionless liquid enthalpy in single phase flow in flow field scaling [46]. From the definition of the dimensionless liquid enthalpy in single phase flow, the dimensionless temperature for the bulk coolant temperature is given by

$$\theta_\infty^* \triangleq \frac{c_{pf} \left(T_s - T_\infty \right) \Delta \rho}{\Delta i_{fg} \rho_g} \quad (4.54)$$

As seen from Eqs. (4.53) and (4.54), the dimensionless temperatures are all positive quantities. In two-phase flow section of the channel, θ_∞^* becomes zero since bulk coolant temperature is the same as the saturation temperature.

Based on the scaling variables defined above, the dimensionless fuel pellet and cladding equations are written as

$$\frac{d\theta_p^*}{dt^*} = \frac{n(t^*)}{\langle \rho c \rangle_p^* A_p^*} - a_p^* \left(\theta_p^* - \theta_c^* \right) \quad (4.55a)$$

$$\frac{d\theta_c^*}{dt^*} = a_p^* \frac{\langle \rho c \rangle_p^* A_p^*}{\langle \rho c \rangle_c^* A_c^*} \left(\theta_p^* - \theta_c^* \right) - a_c^* \left(\theta_c^* + \theta_\infty^* \right) \quad (4.55b)$$

where a_p^* and a_c^* are the dimensionless pseudo thermal diffusivity of the pellet and cladding, respectively. Another dimensionless equation is written for the single-node lumped model as follows:

$$\frac{d\theta_{fe}^*}{dt^*} = \frac{n(t^*)}{\langle \rho c \rangle_{fe}^* A_{fe}^*} - a_{fe}^* \left(\theta_{fe}^* + \theta_\infty^* \right) \quad (4.56)$$

4.5.2 Frequency Domain Analysis: Transfer Functions

In this section, the problem derived in time domain in the previous sections is transformed into frequency domain by linearizing Eq. (4.56) and then applying the Laplace transformation to it. The transfer functions between coolant power and the heat generation inside the pellet are derived by considering the single and two-phase flow conditions in the channel.

The initial condition for Eq. (4.56) is given as

$$\theta_{fe,o}^* = \frac{1}{N_{Fo} \langle \rho c \rangle_{fe}^* A_{fe}^*} - \theta_{\infty,o}^* \quad (4.57)$$

where N_{Fo} is the Fourier number defined as

$$N_{Fo} \triangleq \frac{U'_o}{\langle \rho c \rangle_{fe} A_{fe} \Omega_o} \quad (4.58)$$

which is the dimensionless fuel element thermal diffusivity at steady state. Since the heat conductance, U'_o , depends on the flow conditions, the Fourier number is defined for single and two-phase flow sections of the channel, separately. The Fourier number is the ratio of the heat transferred to the heat stored in the fuel element and a measure of the conduction time lag. Therefore, it is one of the important dimensionless numbers of the fuel heat conduction process.

In single phase flow, the heat transfer coefficient, $h_{1\phi}$, can be written as a function of liquid velocity after neglecting the pressure dependency. From Dittus-Boelter correlation [43], the following equation is written for the heat transfer coefficient in terms of dimensionless liquid velocity,

$$\frac{h_{1\phi}}{h_{1\phi,o}} = (N_{Zu} v_f^*)^{0.8} \quad (4.59)$$

where $v_f^* = \frac{v_f}{\Omega l_h}$ is the dimensionless liquid velocity in single phase flow. N_{Zu} is the

Zuber or Phase Change Number defined as

$$N_{Zu} \triangleq \frac{\Omega_o l_h}{v_{f,o}} = \frac{\langle Q'_o \rangle l_h}{A \Delta i_{fg} v_{f,o} \rho_f} \frac{\Delta \rho}{\rho_g} \quad (4.60)$$

where l_h is the channel heated length. As described in Ref. [46], the Zuber number is one of the important dimensionless numbers in fluid flow field scaling. $h_{1\phi,o}$ in Eq. (4.59) is the heat transfer coefficient in single phase flow computed from the liquid velocity at the steady-state condition.

In two-phase flow, as described in Section 4.2.3, the heat transfer coefficient, $h_{2\phi}$, depends on wall superheat, $\Delta T_w = (T(R_c) - T_s)$. However, the model equation is written in terms of area-averaged temperature. Therefore, the functional form of the heat transfer coefficient in the two-phase flow should be adjusted from Eq. (4.27) and resistance network shown in Figure 4.2. The following equation can be written for the heat transfer coefficient in the two-phase flow by neglecting the pressure effect:

$$\frac{h_{2\phi}}{h_{2\phi,o}} = \left(\frac{\theta_{fe}^*}{\theta_{fe,o}^*} \right)^{\frac{m}{m+1}} \quad (4.61)$$

where the coefficient, m , is given in Table 4.1. In the formulation of Eq. (4.61), the convective resistance, R'_5 , is assumed small compared to other conductive thermal resistances in the fuel pellet and cladding. This is a reasonable assumption especially for the two-phase flow since the two-phase flow associates with higher heat transfer coefficients.

In the following two sections, the transfer functions between coolant power (reaction frequency) and heat generation inside the fuel pellet (neutron amplitude function) are derived for both single and two-phase sections of the flow channel.

The linearization procedure can be viewed as a first order Taylor expansion of a function. Let f be a function of parameters $x_1, x_2, x_3, \dots, x_n$. The first order

perturbation on the independent variables, x_i , yields perturbation in f as

$$\delta f = \frac{\partial f}{\partial x_1} \delta x_1 + \frac{\partial f}{\partial x_2} \delta x_2 + \dots + \frac{\partial f}{\partial x_n} \delta x_n \quad (4.62)$$

where partial derivatives are evaluated at stationary state.

4.5.2.1 Single Phase Flow

The dimensionless thermal diffusivity in Eq. (4.56), which is a function of the liquid velocity, can be perturbed and Laplace-transformed to yield

$$\delta a_{fe}^*(s^*) = 0.8 \frac{N_{Fo,1\phi}}{N_{Bi,1\phi}} N_{Zu} \delta v_f^*(s^*) \quad (4.63)$$

where $N_{Bi,1\phi}$ is the Biot number for the single phase flow defined as follows,

$$N_{Bi,1\phi} \triangleq \frac{2\pi N_{rod} R_c h_{1\phi,o}}{U'_o} \quad (4.64)$$

The Biot number represents the ratio of convective conductance, $2\pi N_{rod} R_c h_{1\phi,o}$, to the total conductance, U'_o . $N_{Fo,1\phi}$ is the Fourier number in the single phase flow calculated by means of the heat transfer coefficient, $h_{1\phi,o}$ from Eq. (4.58).

The reaction frequency in the single phase flow is written as

$$\Omega_{1\phi}^* = a_{fe}^* \langle \rho c \rangle_{fe}^* A_{fe}^* (\theta_{fe}^* + \theta_\infty^*) \quad (4.65)$$

By linearizing Eqs. (4.56) and (4.65), and applying the Laplace transformation, the following transfer function for the reaction frequency in the single phase flow can be derived,

$$\begin{aligned} \delta \Omega_{1\phi}^*(s^*) &= \frac{N_{Fo,1\phi}}{s^* + N_{Fo,1\phi}} \delta n(s^*) + \langle \rho c \rangle_{fe}^* A_{fe}^* \frac{N_{Fo,1\phi} s^*}{s^* + N_{Fo,1\phi}} \delta \theta_\infty^*(s^*) \\ &+ 0.8 \frac{N_{Zu}}{N_{Bi,1\phi}} \frac{s^*}{s^* + N_{Fo,1\phi}} \delta v_f^*(s^*) \end{aligned} \quad (4.66)$$

where $s^* = \frac{s}{\Omega_o}$ is the dimensionless frequency.

4.5.2.2 Two-phase Flow

In two-phase flow section of the channel, the dimensionless fuel element equation reduces to

$$\frac{d\theta_{fe}^*}{dt^*} = \frac{n(t^*)}{\langle \rho c \rangle_{fe}^* A_{fe}^*} - a_{fe}^* \theta_{fe}^* \quad (4.67)$$

where the dimensionless thermal diffusivity, a_{fe}^* , depends on the dimensionless fuel element temperature, θ_{fe}^* through Eq. (4.61). Applying first order perturbation and the Laplace transformation, the following expression is obtained,

$$\delta a_{fe}^*(s^*) = \frac{N_{Fo,2\phi}}{N_{Bi,2\phi}} \frac{m}{m+1} \delta \theta_{fe}^*(s^*) \quad (4.68)$$

where $N_{Fo,2\phi}$ and $N_{Bi,2\phi}$ are Fourier and Biot numbers in two-phase flow computed by means of heat transfer coefficient, $h_{2\phi,o}$.

The dimensionless reaction frequency in the two-phase flow is written as

$$\Omega_{2\phi}^* = a_{fe}^* \langle \rho c \rangle_{fe}^* A_{fe}^* \theta_{fe}^* \quad (4.69)$$

By linearizing Eqs. (4.67) and (4.69) and applying the Laplace transformation, the following transfer function for the reaction frequency in the two-phase flow can be obtained:

$$\Omega_{2\phi}^*(s^*) = \frac{N_{Fo,2\phi} + \frac{m}{m+1} \frac{1}{\langle \rho c \rangle_{fe}^* A_{fe}^* N_{Bi,2\phi}}}{s^* + N_{Fo,2\phi} + \frac{m}{m+1} \frac{1}{\langle \rho c \rangle_{fe}^* A_{fe}^* N_{Bi,2\phi}}} \quad (4.70)$$

Equation (4.70) can be further simplified if one assumes

$$N_{Fo,2\phi} \gg \frac{m}{m+1} \frac{1}{N_{Bi,2\phi} \langle \rho c \rangle_{fe}^* A_{fe}^*} \quad (4.71)$$

to the following form:

$$\delta\Omega_{2\phi}^*(s^*) = \frac{N_{Fo,2\phi}}{s^* + N_{Fo,2\phi}} \delta n(s^*) \quad (4.72)$$

As seen from Eqs. (4.66) and (4.72), the Fourier number is the most important dimensionless number for fuel heat conduction time delay, which characterizes the time lag between the generation inside the pellet ($\delta n(s^*)$) and the heat transferred to the coolant ($\Omega_{1\phi}^*(s^*)$, $\Omega_{2\phi}^*(s^*)$). The transfer function between $\Omega_{1\phi}^*$, $\Omega_{2\phi}^*$ and n is simply a first order time delay and has quite similar characteristics compared to RC-circuits which are used in signal processing in electronics. The following section examines this similarity based on two different RC-circuits.

4.6 RC-circuit Analogy

Heat conduction process can be considered as a process which can be represented with representative resistance and capacitance in a RC circuit. Two different RC circuits are shown in Figure 4.5.

The first circuit is used as a low-pass filter which removes the high frequency content of the input signal. When the frequency domain analysis is performed for the input and the output signals, the following transfer function can be obtained:

$$\frac{\delta E_{out}}{\delta E_{in}} = \frac{1}{\tau s + 1}, \quad (4.73)$$

where $\tau = RC$ is the time constant of the circuit, which is equivalent to the inverse of the Fourier number defined by Eq. (4.58). R and C represent the resistance and capacitance in the circuits shown in Figure 4.5. The basic function of the circuit is integration and it filters the high frequency oscillations in the input signal. Comparing to the transfer function obtained between the heat flux (reaction frequency) and heat generation (neutron amplitude) given in Eqs. (4.66) and (4.72), it can be concluded that the heat conduction process behaves similarly compared to the RC-integrator circuit which removes the high frequency oscillations in the input signal, which is the neutron flux amplitude.

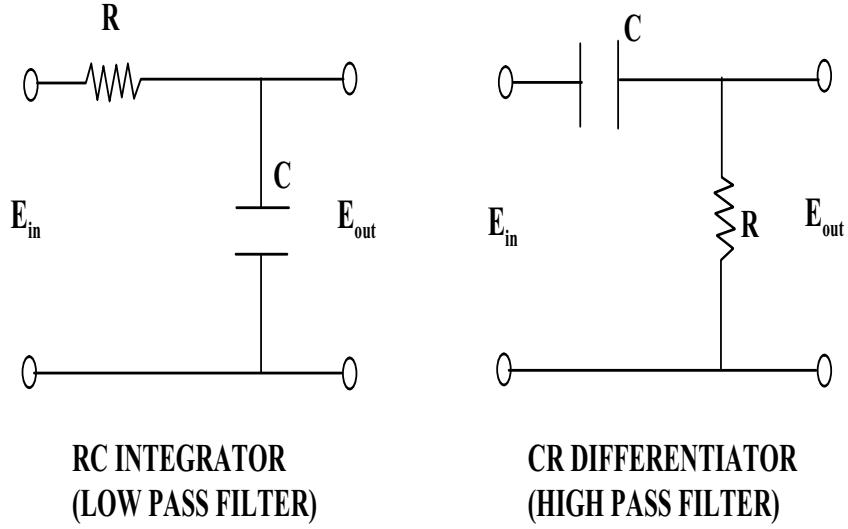


Figure 4.5. High Pass and Low Pass RC Circuits

The detailed properties of a RC-integrator can be analyzed by giving a sinusoidal input signal with an oscillating frequency, ω . The input signal can be defined as

$$E_{in} = A_{in} \sin(2\pi\omega t) \quad (4.74)$$

and the output signal

$$E_{out} = A_{out} \sin(2\pi\omega t + \phi) \quad (4.75)$$

where ϕ is the phase shift between the input and output signals. A_{in} and A_{out} represent the input and output amplitudes, respectively. The amplitude ratio of the output signal to the input signal, which is the damping in the system, can be written as

$$\frac{|A_{out}|}{|A_{in}|} = \frac{1}{\sqrt{1 + (\omega/\omega_f)^2}}. \quad (4.76)$$

Furthermore, the phase shift between the input and output signals is written as

$$\phi = -\arctan(\omega/\omega_f) \quad (4.77)$$

where ω_f is the characteristic frequency given as the reciprocal of the circuit time

constant, τ . Similarly, for the heat conduction process, the characteristic frequency is proportional to the Fourier number.

There is a certain relation between the oscillation period and the time constant in terms of the damping in the system. However, it can be easily shown that when the oscillating frequency is much larger than the Fourier number, $\omega \gg N_{Fo}$, the system has large damping on the neutron flux oscillations. In other words, the high-frequency oscillations in neutron flux are smoothed out by the heat conduction. The coolant side does not feel rapid change in the heat generation due to the high frequency neutron flux oscillations. On the other hand, when the oscillating frequency is much smaller than the Fourier number, $\omega \ll N_{Fo}$, which corresponds to low-frequency oscillations, there is almost no damping. Therefore, large amplitude neutron flux oscillations are translated into large amplitude heat flux oscillations on the fuel element wall.

For the second circuit in Figure 4.5, which is CR-Differentiator circuit, the transfer function between the input and the output signal is written as

$$\frac{\delta E_{out}}{\delta E_{in}} = \frac{\tau s}{\tau s + 1}. \quad (4.78)$$

The RC-Differentiator circuit is used for removing the low-frequency content of the signal. In other words, only high-frequency information is passed through. From the transfer function of the wall heat flux in the single phase region given by Eq. (4.66), it can be seen that the coolant side perturbation like velocity and the inlet subcooling have RC-Differentiator-like behavior on the wall heat flux. However, the neutron flux oscillations have major contribution to the wall heat flux oscillations. In addition, in the two-phase region, inlet velocity and subcooling have no effect on the wall heat flux response. Therefore, low-pass filter behavior is dominant in the heat conduction process.

5. NEUTRON KINETICS MODELING

The neutron kinetics describes the rate of change in the neutron flux throughout the core. Since the neutron flux level determines the amount of heat generation inside the fuel pellet as a result of fission, it is directly related to the volumetric heat generation rate in the heat conduction equation.

General introduction and modeling strategy for the neutron kinetics analysis are presented in this chapter. After some introductory material, Point Kinetic Model (PKM) is described as a model for simulating the void-reactivity coupling simulation in the experimental facility.

The vital part of the void-reactivity feedback simulation is to generate the void-reactivity coefficient which links the neutron flux change to the void fraction change in the core. HELIOS [47], a two-dimensional neutron transport code, is used to determine the void-reactivity coefficient for a typical SBWR fuel bundle under different operating pressures and average void fractions. By generating the neutron group constants at different thermal-hydraulic conditions, the reactivity coefficient as a function of simulated void fraction and pressure used in the simulation is obtained.

5.1 Introduction

The nature of the kinetic problem in reactor physics highly depends on the time constant of the phenomenon considered [48]. Three different phenomena can be highlighted:

1. Short Time Phenomena, which typically occur in time intervals of milliseconds to seconds: In special cases, the time intervals may extend to many minutes.
2. Medium Time Phenomena, which occur over hours or days corresponding to the mean buildup and decay times of certain fission products that can strongly

affect the reactivity.

3. Long Term Phenomena, with variations developing over several month to years.

In each category, the modeling strategy differs appreciably. For the startup analysis of SBWR, the strategy includes the phenomena of first and second types. Since the startup process takes over hours, medium time phenomena becomes important and requires consideration of control rod motion and power increase. On the other hand, possible oscillation in the flow field causes the void-reactivity feedback loop to occur, which creates short time power change within seconds. For the medium term transients, parameters affecting the neutron kinematics can be considered in a quasi-steady manner. However, for the latter case in which void oscillations occur in the core, transient aspects of the problem should be considered in detail such as the heat conduction time constant (Sec. 4.4), the neutron generation time, and the precursor decay constant, etc.

The transient behavior of neutron flux in the core is a result of off-criticality. In other words, transient is caused by the imbalance between the neutron production via fission and loss via absorption and leakage. Off-criticality can be described by a time-dependent neutron diffusion equation of the form

$$\frac{1}{v} \frac{\partial \Phi}{\partial t} = (F - M - F_d)\Phi + S_d, \quad (5.1)$$

where

F : Fission operator which contains fission cross section

F_d : Delayed fission operator which represents the delayed fission neutron source

M : Diffusion and loss operator which contains absorption and transport cross sections

Φ : Space, time and energy dependent neutron flux

S_d : Delayed neutron source coming from the decay of some of the fission products

v : Neutron velocity

Small fraction of total fission neutrons comes from the decay of some of the fission products. Even though the fraction, which is called “delayed neutron yield”, is very small (0.00625), it is very important in nuclear reactor control because of their long time constants [48]. Since the delayed neutrons are coming from some of the fission product groups, the delayed neutron population is also a function of the neutron flux. Therefore, an equation for S_d is necessary for closure. The relation between the delayed neutron source, S_d , and the precursor concentration, C_k , is given as follows:

$$S_d(\vec{r}, t) = \sum_k \lambda_k C_k(\vec{r}, t) \quad (5.2)$$

where index k represents the k^{th} precursor group. The equation for the precursor concentration of the group k is written as a simple balance equation consisting of a source term due to fission and loss term due to radioactive decay:

$$\frac{\partial C_k}{\partial t} = -\lambda_k C_k(\vec{r}, t) + \int_0^\infty \nu_{dk} \Sigma_f(\vec{r}, t) \Phi(E' \vec{r}, t) dE'. \quad (5.3)$$

where the energy dependency in the neutron flux is considered.

Precursor groups describes the nuclei groups having similar properties in terms of the decay constant and neutron energy. Each group can be described with precursor concentration, C_k , decay constant, λ_k , and delayed neutron yield, ν_{dk} .

5.2 Point Kinetic Model

Transient behavior of the neutron flux or the core power generation can be determined by solving the Eqs. (5.1) and (5.3). However, the neutron group cross-sections, especially absorption and transport cross-sections are strong functions of temperature and flow field. In BWRs, the coolant density or the void fraction changes the diffusion and loss operator, M , appreciably. The phenomenon is called “void-reactivity feedback” and requires the knowledge of the void-fraction dependent neutron group cross-sections.

There are some simplified models which can be used to predict the time-

dependent behavior [48]. The Point Kinetic Model (PKM) is one of the very simplified models which has been used over the years. It is based on the separability assumption that space and time dependency of neutron flux can be described by two-separate functions; neutron amplitude, $n(t)$, and neutron flux distribution at steady state, $\Phi_o(r)$. Therefore, the neutron flux can be written as a product of these two functions

$$\Phi(r, t) = n(t)\Phi_o(r), \quad (5.4)$$

This model considers the reactor core as a point where time dependent change in neutron flux distribution is negligible. This model gives good estimation for BWR oscillations where the whole core oscillates in-phase [20].

Based on the separability assumption, two set of ordinary differential equations can be obtained for the neutron amplitude function, $n(t)$, and the precursor concentration for group k , $\xi_k(t)$, as follows

$$\frac{dn}{dt} = \frac{\rho(t) - \beta}{\Lambda} n(t) + \frac{1}{\Lambda} \sum_{k=1}^6 \lambda_k \xi_k(t) \quad (5.5a)$$

and

$$\frac{d\xi_k}{dt} = -\lambda_k \xi_k(t) + \beta_k n(t), \quad (5.5b)$$

where

β_k : Delayed neutron yield of the k^{th} group

λ_k : k^{th} group precursor decay constant

ξ_k : k^{th} group reduced precursor concentration

ρ : dynamic reactivity $\frac{k-1}{k}$

Λ : neutron generation time

Reactivity used in Eq. (5.5a) is an integral quantity defined as

$$\rho = \frac{k-1}{k} \quad (5.6)$$

where k is the multiplication factor, which is the inverse of the eigenvalue of the

diffusion equation. From its definition, reactivity is zero for a critical reactor. Positive values indicate the super-criticality and negative values indicate the sub-criticality. The formal definition of reactivity can be derived from the first order perturbation theory as [49]

$$\rho(t) = \frac{\int_V \int_E \Phi_o^*(r, E) (\frac{1}{k} \Delta F - \Delta M) \Phi_o(\vec{r}, E) dE dV}{\int_V \int_E \Phi_o^*(\vec{r}, E) F_o \Phi_o(\vec{r}, E) dE dV}, \quad (5.7)$$

where Φ_o^* is adjoint flux which shows the importance of neutrons. The adjoint flux is actually the eigenfunction of the neutron diffusion problem at steady state written in terms of adjoint operators for M and F. Ref. [49] provides detailed explanation of the problem for adjoint flux and operators for the neutron diffusion equation. For the one group neutron diffusion equation, it can be shown that the adjoint flux, Φ_o^* , is same as the neutron flux, Φ_o . Therefore, Φ_o^* is larger at the core center where neutron population is higher and more important. The definition of reactivity involves the change in migration and fission operators. For BWR applications, reactivity change due to the void fluctuations comes from the change in M.

For a general neutron kinetics problem, the reactivity should be provided in order to solve the problem when the Point Kinetic Equations (PKEs) given in Eqs. (5.5a, 5.5b) and are used ρ consists of several components,

$$\rho(t) = \rho_{ext}(t) + \rho_\alpha(t) + \rho_D(t) \quad (5.8)$$

where

- $\rho_{ext}(t)$: reactivity due to control rods or other control elements
- $\rho_\alpha(t)$: reactivity due to void fraction change – moderator density
- $\rho_D(t)$: reactivity due to fuel temperature change – Doppler

External reactivity due to control rod motion is the reactivity that can be computed from power curve. For a given power transient, inverse problem, which will be described later, can be solved for reactivity. However, for medium transients such as the startup of SBWR, one should also consider the thermodynamic state change

(changes in the average void and the fuel temperature) during this transient. In that case, it is necessary to consider the reactivity loss due to the moderator density change via average core void fraction and fuel temperature changes.

The void-reactivity and the fuel temperature-reactivity are two important reactivities that link the thermal-hydraulics and the neutronics. Generally, they are specified with reactivity coefficients which show the change in the reactivity due to change in the feedback parameter, either the void fraction or the fuel temperature. Therefore, following coefficients are defined for the thermal-hydraulic feedback reactivities,

$$K_{\alpha} = \frac{\partial \rho}{\partial \alpha} \quad (5.9a)$$

and

$$K_D = \frac{\partial \rho}{\partial T_p} \quad (5.9b)$$

where $\langle\langle T \rangle\rangle_p$ is the fuel pellet temperature which is properly averaged over pellet region considering the pellet radial power shape. Based on the definitions of the reactivity coefficients, reactivity due to each feedback loop can be determined from the following equations:

$$\rho_{\alpha} = \int_{\langle\langle \alpha \rangle\rangle_o}^{\langle\langle \alpha \rangle\rangle(t)} K_{\alpha} d\langle\langle \alpha \rangle\rangle \quad (5.10a)$$

and

$$\rho_D = \int_{\langle\langle T \rangle\rangle_{po}}^{\langle\langle T \rangle\rangle_p(t)} K_D d\langle\langle T \rangle\rangle_p \quad (5.10b)$$

5.3 Void Reactivity Coefficient for SBWR

The void-reactivity coefficient, the vital part of the void-reactivity feedback simulation, is calculated by means of the HELIOS code [47], which is a two-dimensional neutron transport code. A typical SBWR 8×8 square-array fresh fuel bundle is considered for the analysis. All detailed structures such as Zircaloy-2 bundle-box, single-phase liquid which surrounds the bundle can and control rod blade are modeled.

Considering the different pressure levels during the startup process, bundle-

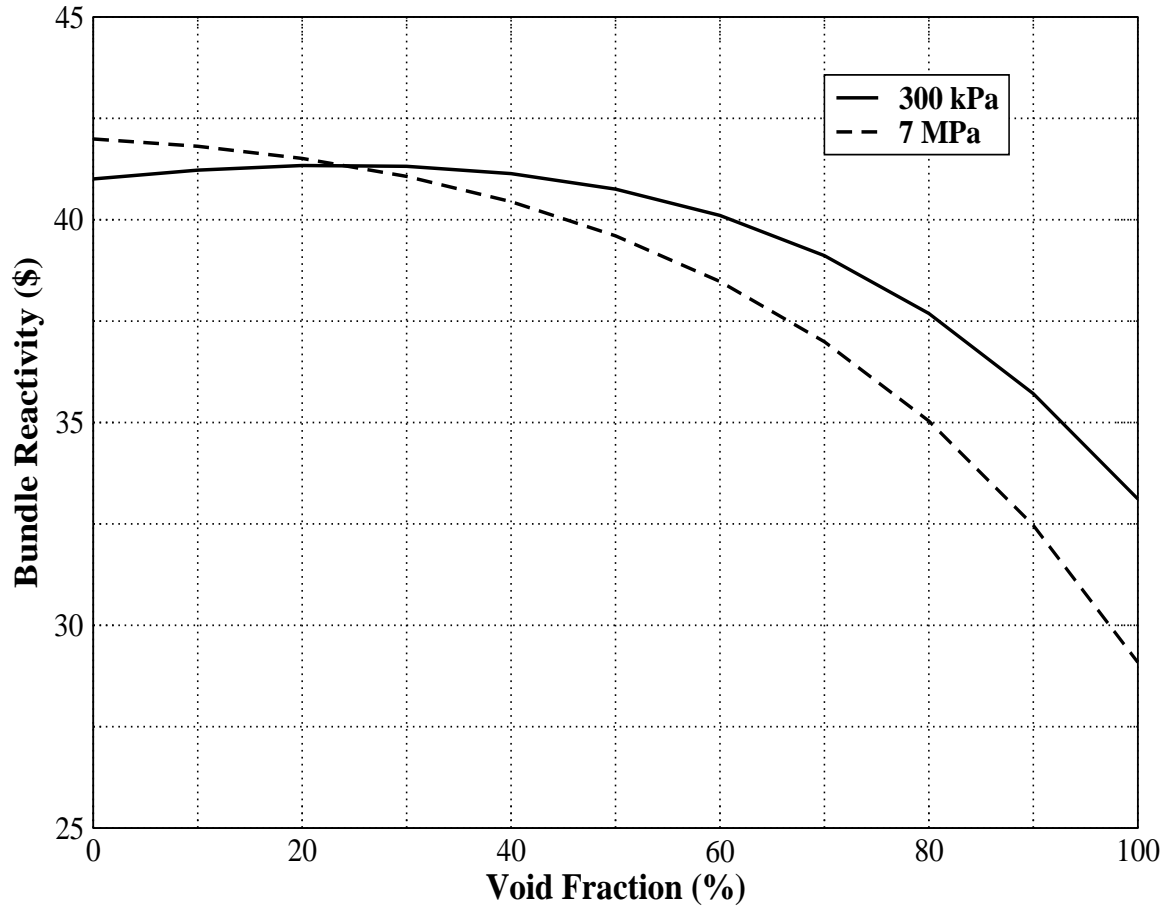


Figure 5.1. Change in Bundle Reactivity with the Void Fraction at Different Pressures

reactivity for the SBWR is generated for different values of the void fraction. By varying the void fraction from 0% to 100%, the bundle-reactivity is plotted against the void fraction at different pressures. As an example of the calculation results, Figure 5.1 demonstrates the change in bundle reactivity with the void fraction at two different pressures.

As shown in Figure 5.1, the bundle reactivity increases with the void fraction at low pressures. This behavior can be explained in terms of the absorption and the moderation effect of the water at low pressure. The liquid density at low pressures is higher than the density at high pressures. Therefore, the bundle is initially over-moderated. In other words, neutrons are effectively thermalized and some of the

neutrons are absorbed by the coolant. The amount of the absorption effect is higher than that of the moderation. Therefore, increasing the void fraction is equivalent to remove the absorber material (like withdrawing a control rod). Until a certain void fraction value is reached, the absorption effect of the coolant is important. However, when the void fraction is further increased, the reactivity starts to decrease due to the loss of the moderator material. At the nominal operating pressure, bundle is always under-moderated. Therefore, increasing the void fraction always accompany with decreasing reactivity assuring that the void-reactivity coefficient is always negative. Figure 5.2 shows the derivative of the plot in Figure 5.1 which is the void-reactivity coefficient. It can be clearly seen that at low pressures up to around 22% void fraction, void-reactivity coefficient is positive. However, the total reactivity coefficient, i.e., the sum of the void-reactivity and Doppler reactivity, is always negative, otherwise the reactor cannot be stable. The requirement for a reactor to be stable all the time is that it should have a negative power-reactivity coefficient, thus an increase in reactor power is always accompanied with decreasing reactivity.

In order to reveal the complete picture relevant to the void-reactivity coefficient in the SBWR fuel bundle, several pressure levels are tested and the void-reactivity coefficients is calculated. Figure 5.3 demonstrates the pressure effect on void-reactivity coefficient. Since the reactivity coefficient is averaged over a certain range of the void fraction, the positiveness of the coefficient at low pressure is lost. The averaging is performed over void fraction range from 0% to 30%. Smaller averaging intervals would reveal the positive void reactivity coefficient region at lower pressure. However, the important point in this analysis is that the negative reactivity coefficient increases in magnitude as the pressure increases which increases the amount of reactivity due to void fluctuations.

5.4 Calculation of Reactivities for Point Kinetic Model

A calculation of a transient via PKEs requires specification of reactivities of different types. In this section, a methodology for calculating the following reactivities is discussed:

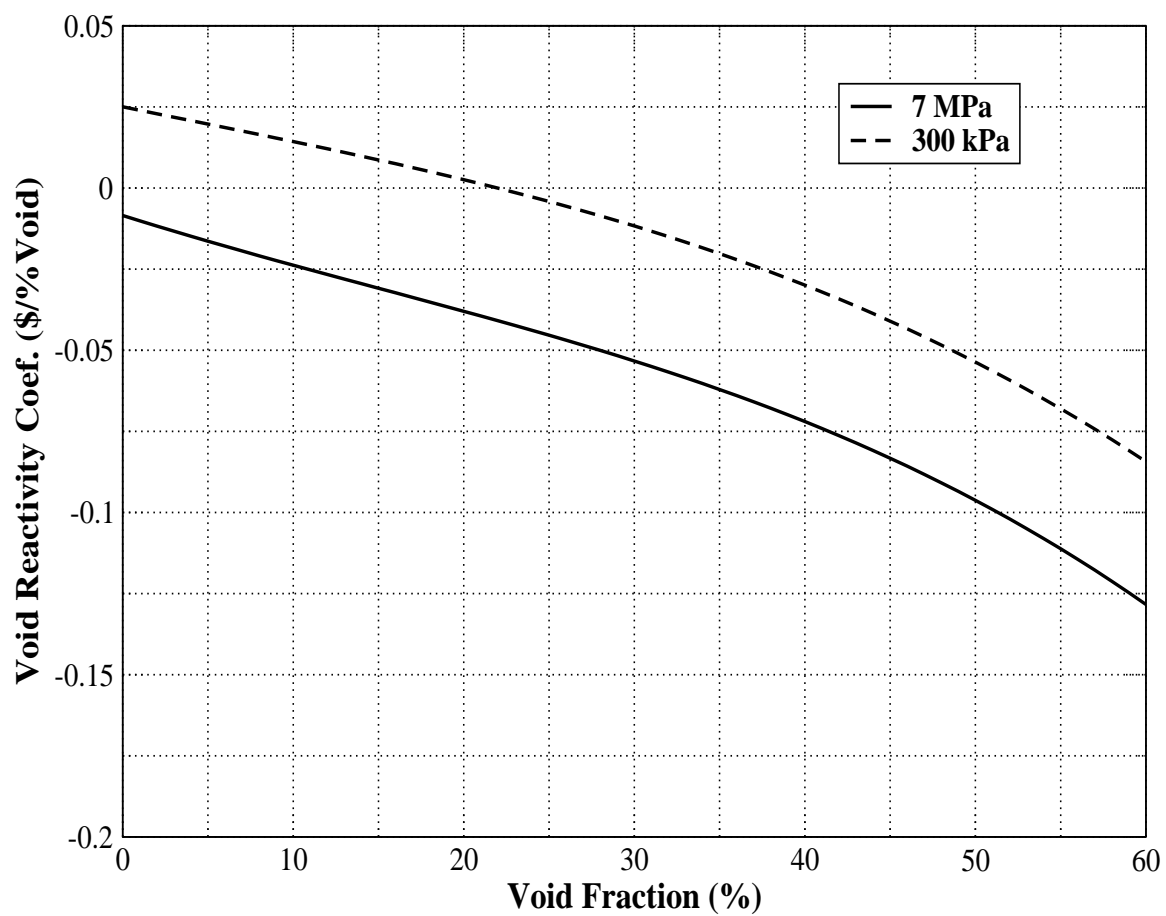


Figure 5.2. Void-Reactivity Coefficient as a Function of the Void Fraction

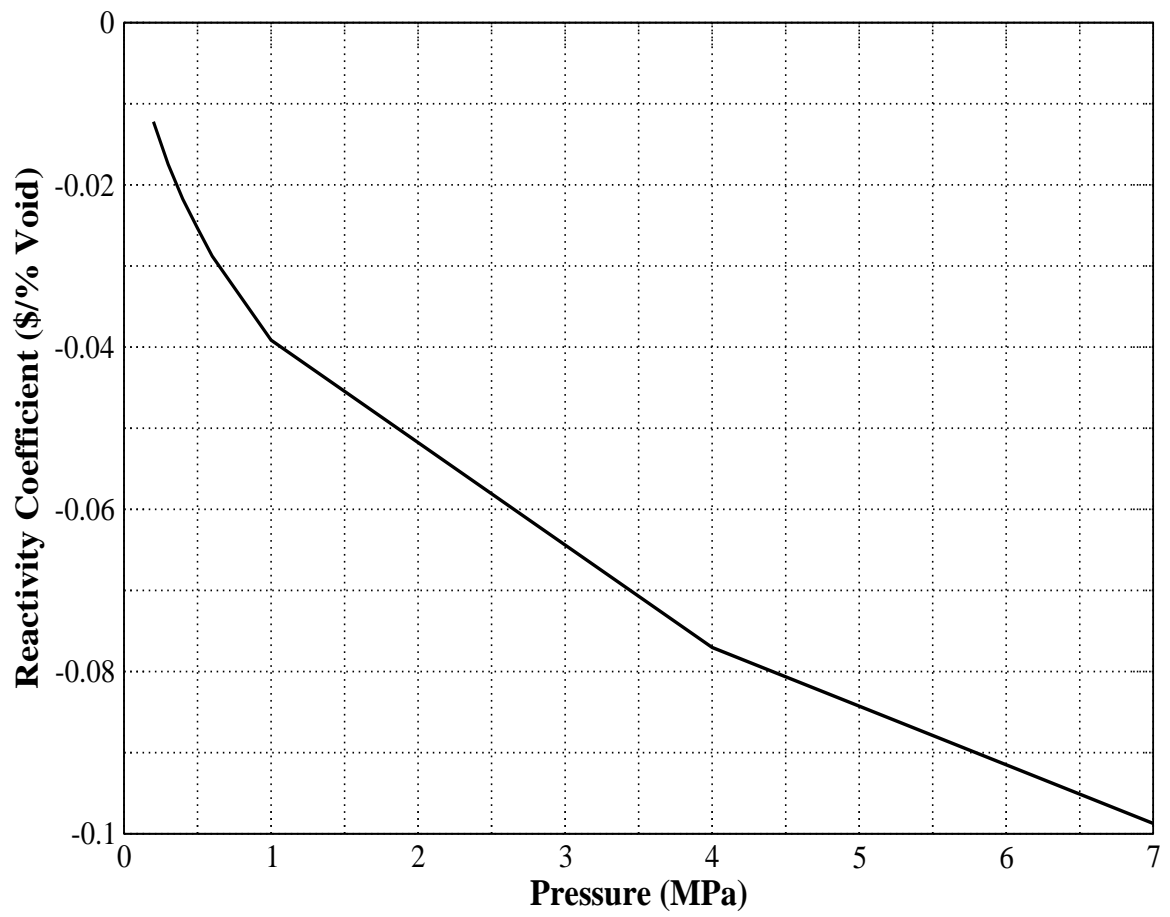


Figure 5.3. Average Void-Reactivity Coefficient over a $\alpha = 0$ to 0.3 as a Function of Pressure

- i. Void Reactivity due to void fraction change
- ii. Doppler Reactivity due to fuel temperature change.

5.4.1 Feedback Reactivities

The void-reactivity feedback caused by the void fraction change in two-dimensional core can be estimated from [50]

$$\Delta\rho_\alpha(t) = \frac{1}{V} \iiint_V \Phi(\vec{r})^* \Phi(\vec{r}) K_\alpha(\vec{r}) dV, \quad (5.11)$$

where $\Phi^*(\vec{r})$ is the adjoint flux described in Section 5.2. In one-group diffusion theory, it can be shown that the adjoint flux, $\Phi^*(\vec{r})$, is identical to the neutron flux, $\Phi(\vec{r})$, or simply the core power distribution [49]. The definition of the void-reactivity can be further simplified by considering the volume-averaged void fraction as;

$$\Delta\rho_\alpha(t) = \int_0^{\langle\langle\alpha\rangle\rangle(t)} K_\alpha d\langle\langle\alpha\rangle\rangle, \quad (5.12)$$

where $\langle\langle\alpha\rangle\rangle$ is the volume-averaged void fraction which includes the effect of power shape and K_α is the void-reactivity coefficient which is calculated via HELIOS [47] code predictions described in Section 5.3.

Similarly, the Doppler reactivity coefficient can be computed from

$$\Delta\rho_D(t) = \int_{\langle\langle T_p \rangle\rangle_o}^{\langle\langle T_p \rangle\rangle(t)} K_D d\langle\langle T_p \rangle\rangle \quad (5.13)$$

where $\langle\langle T_p \rangle\rangle$ is the volume-averaged fuel pellet temperature.

6. FLOW EXCURSION MODELING VIA SUBCOOLED BOILING

The detailed analysis of the flow excursion phenomenon in forced and the natural circulation systems is presented in this chapter. The dimensionless characteristic equation derived based on the analytical modeling presented in Chapter 3 is solved to generate stability maps on Subcooling Number – Zuber Number and Zuber Number (or Subcooling Number) – Froude Number planes.

Before deriving the general characteristic equation for the flow excursion, the problem fundamentals are described in terms of the integral loop momentum equation. The channel pressure drop characteristics are described on the pressure drop vs. mass flow rate curve.

The steady-state solution of the dimensionless equations introduced in the previous chapter is presented and the dimensionless pressure drop components are obtained by integrating the momentum equation over the single-phase and the two-phase regions. The criterion obtained for the flow excursion stability is applied and the characteristic equation is obtained in terms of the dimensionless numbers.

6.1 Stability Criterion for Flow Excursion

For simplicity, let us consider a single heated channel imposed to constant pressure drop boundary condition. Integrating the momentum equation along the flow path gives the following loop momentum equation:

$$\left(\frac{l_h}{A_h}\right) \frac{d\dot{m}}{dt} = \Delta P_s - \sum_i (\Delta P)_i \quad (6.1)$$

where ΔP_s is the supply pressure drop for the channel, which is provided by either a pump or gravity head. In the particular example, the supply pressure drop is taken constant, i.e. independent from channel flow rate, \dot{m} . ΔP_i is the i^{th} pressure drop

component such as gravity, friction, spatial acceleration etc.

By assuming small perturbation around the steady state solution for flow rate and expanding the pressure drop into the Taylor Series expansion, the following equation can be obtained after neglecting the second and higher order terms:

$$\delta\dot{m}(t) = \delta\dot{m}(0) \exp \left[\left(\frac{l_h}{A_h} \right) \left\{ \frac{\partial \Delta P_{so}}{\partial \dot{m}} - \sum_i \frac{\partial (\Delta P_o)_i}{\partial \dot{m}} \right\} t \right] \quad (6.2)$$

In order for the initial perturbation on the channel flow rate, $\delta\dot{m}(0)$, to die away, the term inside the exponential in Eq. (6.2) should be negative. Therefore, for the stability of the system in terms of the flow excursion, the following criterion should be met,

$$\sum_i \frac{\partial (\Delta P_o)_i}{\partial \dot{m}} \geq \frac{\partial \Delta P_{so}}{\partial \dot{m}} = 0 \quad (6.3)$$

where the subscript, o , denotes the steady state value. The steady state pressure drop can be written as a summation of the several components;

$$(\Delta P)_o = (\Delta P)_{in} + (\Delta P)_{fr} + (\Delta P)_{gr} + (\Delta P)_{sa} + (\Delta P)_{dr} + (\Delta P)_e \quad (6.4)$$

The first term on the right-hand-side of Eq. (6.4) is the channel inlet pressure drop, the second term is the frictional pressure drop, the third is the pressure drop due to the gravity, the forth term is due to convective acceleration, the fifth term is the pressure drop due to the drift and last term stands for the localized pressure drop at the channel exit.

6.2 Characteristic Equation for Flow Excursion

The characteristic equation for the flow excursion can be derived based on the steady state solution of the dimensionless field equations. The formulation presented in this section considers the following sections:

- i– Single Phase Heated Section
- ii– Two-Phase Mixture Heated Section

iii– Two-Phase Mixture Unheated Section

For each region, required field equations are solved to obtain the velocity and the density profile. Finally, the integration of the momentum equation in each region yields Euler Number, N_{Eu} , which is the ratio of the pressure to the inertia forces, defined as

$$N_{Eu} = \frac{\Delta P}{\rho_f v_{fin,o}^2} = \frac{\Delta P}{\rho_f (\Omega_s l_h)^2} \frac{(\Omega_s l_h)^2}{v_{fin,o}^2} = \Delta P^* N_{Zu}^2 \quad (6.5)$$

6.2.1 Single-Phase Heated Section

The constant liquid density assumption yields spatially uniform liquid velocity in the single phase heated section. Therefore, up to the PNVG, λ , the dimensionless velocity is given as the inverse of the Zuber number defined by Eq. (3.59). Since axially uniform heat flux distribution is assumed, the single phase energy equation can be easily integrated to obtain the non-boiling height with the following boundary conditions; $N_s(0) = N_{sub}$, and $N_s(\lambda) = N_{sd}$, which is the dimensionless departure enthalpy for PNVG. Therefore, the non-boiling height is give as follows:

$$\lambda^* = \frac{N_{sub}}{N_{Zu}} - \frac{1}{N_{Zu}} \begin{cases} 0.0022 \frac{D_e^*}{\xi_h^*} \frac{1}{a_f^*} & N_{Pe} < 70000 \\ \frac{154}{A_h^*} N_{Zu} & N_{Pe} \geq 70000 \end{cases} \quad (6.6)$$

The integration of the momentum equation given by Eq. (3.52) in this region, $(0 < z^* < \lambda^*)$, gives the single phase heated region Euler number as follows;

$$N_{Eu,h}^{1\phi} = \left[\left(N_f + \frac{1}{N_{Fr}} \right) \lambda^* + \frac{K_{in}}{2} \right] \quad (6.7)$$

6.2.2 Two-Phase Mixture Heated Section

In order to integrate the momentum equation over this region, the void distribution should be obtained via solving the continuity equations described in Chapter 3.

The solution of the mixture volumetric flux equation (Eq. (3.42)) gives a linear profile,

$$j^*(z^*) = \frac{1}{N_{Zu}} + C_g(z^* - \lambda^*) \quad (6.8)$$

and the kinematic wave velocity becomes

$$C_k^* = \frac{C_o + N_d}{N_{Zu}} + C_o C_g(z^* - \lambda^*) \quad (6.9)$$

where C_g is the parameter defined by Eq. (3.33) to account for the subcooled boiling in the volumetric vapor generation rate.

The solution of the density wave equation with Eq. (6.9) along with boundary condition, $\rho_m^{+*}(\lambda^*) = 1$, is given by,

$$\rho_m^{+*} = \frac{C_k^*(\lambda^*)}{C_k^*(z^*)} \quad (6.10)$$

which is related to the real density as

$$\rho_m^* = \frac{(C_o - 1)C_k^*(z^*) + C_k^*(\lambda^*)}{C_o C_k^*(\lambda^*)} \quad (6.11)$$

From Eq. (6.11), the heated channel exit density required for the solution in the unheated section can be obtained as follows:

$$\rho_{me}^* = \frac{(C_o - 1)C_r^* + 1}{C_o C_r^*} \quad (6.12)$$

where C_r^* is the ratio of the kinematic wave velocity at the channel exit and the boiling boundary, given by

$$C_r^* = 1 + \frac{N_{Zu} C_o C_g}{C_o + N_d} (1 - \lambda^*)$$

which is always greater than one as long as the two-phase mixture exists in the heated section.

The momentum equation given by Eq. (3.56) can be integrated to determine the Euler number in the two-phase mixture heated section. The integration of the second term in Eq. (3.56) yields the Euler number due to convective acceleration:

$$N_{Eu,h}^{sa} = \frac{C_r^* - 1}{1 + C_r^*(C_o - 1)} \quad (6.13)$$

The Euler number due to friction is determined as:

$$N_{Eu,h}^{fr} = N_f \frac{C_m(C_o + Nd)}{N_{Zu}(C_o - 1)C_g} \left[(C_r^* - 1) - \frac{1}{C_o - 1} \ln \left(\frac{1 + C_r^*(C_o - 1)}{C_o} \right) \right] \quad (6.14)$$

The Euler number due to gravity is

$$N_{Eu,h}^{gr} = \frac{1}{N_{Fr}} \left[\frac{C_o - 1}{C_o} (1 - \lambda^*) + \frac{C_o + Nd}{N_{Zu}C_o^2C_g} \ln(C_r^*) \right] \quad (6.15)$$

Finally, the Euler number in terms of the localized pressure drop at the channel exit, where the two-phase mixture exists, can be written as

$$N_{Eu,h}^e = \frac{K_e}{2} \frac{C_o C_r^*}{1 + C_r^*(C_o - 1)} \quad (6.16)$$

The total Euler number in the heated section is given in Appendix A. In the following section, the Euler number is obtained for the unheated two-phase mixture section.

6.2.3 Two-Phase Mixture Unheated Section

Since it is assumed that unheated section is adiabatic and the compressibility effects are neglected, the void fraction is spatially uniform throughout the unheated part. The mixture velocity in this section becomes

$$v_{muh}^* = v_m^*(1) \frac{1}{A_{uh}^*}$$

where A_{uh}^* is the dimensionless flow area in the unheated two-phase mixture section. By integrating the momentum equation, the Euler number for this section is obtained

as follows:

$$N_{Eu}^c = \frac{C_o C_r^*}{1 + C_r^*(C_o - 1)} \left[\frac{C_m N_f}{D_{e,uh}^* A_{uh}^{*2}} + \frac{K_{e,c}}{2} \frac{1}{A_{uh}^{*2}} \right] + \frac{1}{N_{Fr}} \frac{1 + C_r^*(C_o - 1)}{C_o C_r^*} l_{uh}^* \quad (6.17)$$

where $K_{e,c}$ represents the localized flow resistance at the unheated section exit.

In contrast to the forced circulation systems, the subcooling number is not independent parameter in the natural circulation systems. It depends on the feedwater subcooling and the heated section exit quality which determines the amount of saturated liquid separated in separator section of the loop. Therefore, the subcooling number in the natural circulation systems is a function of the feedwater subcooling number and the Zuber number. By means of a simple energy and mass balance in the mixer region, one can obtain the expression for the subcooling number as

$$N_{sub} = \frac{(1 - N_\rho) N_{sub}^F}{1 + N_\rho (N_{sub}^F - 1)} N_{Zu} \quad (6.18)$$

where N_{sub}^F is the feedwater subcooling number defined in terms of the feedwater enthalpy, i_f^F .

Finally, the Euler number of the system can be written as sum of all components as described before;

$$N_{Eu} = N_{Eu,h}^{1\phi} + N_{Eu,h}^{2\phi} + N_{Eu,uh}^{2\phi}$$

The detailed form of each term is summarized in Appendix A. From Eq. (6.3), the dimensionless characteristic equation can be written by considering the inlet velocity dependency of some of the dimensionless groups such as the Zuber number, Froude number, friction number, and the drift number. In the natural circulation systems, it has been shown that the subcooling number also depends on the inlet velocity via the Zuber number. Therefore, the subcooling number dependency in the characteristic equation should be included.

The characteristic equation for the flow excursion can be written based on the partial derivatives of the Euler number respect to the dimensionless numbers described

above, as follows:

$$Q^* = -N_{Zu} \frac{\partial N_{Eu}}{\partial N_{Zu}} + 2N_{Fr} \frac{\partial N_{Eu}}{\partial N_{Fr}} - N_{sub} \frac{\partial N_{Eu}}{\partial N_{sub}} + mN_f \frac{\partial N_{Eu}}{\partial N_f} - N_d \frac{\partial N_{Eu}}{\partial N_d} = 0 \quad (6.19)$$

which is written in a general form,

$$Q^*(N_{Zu}, N_{sub}, N_{Fr}, N_f, N_d) = 0$$

where m is the Reynold number exponent in the single phase friction factor, which is around 0.25 for the turbulent flow. The negative values of the characteristic equation for the given geometry and operational conditions imply the instability in terms of the flow excursion.

6.3 Pressure Drop vs. Flow Rate Curve Characteristics

As described in Section 6.1, the physical mechanism that causes the flow excursion phenomenaon is explained in terms of the channel pressure drop and the supply pressure drop characteristics. In this section, the detailed discussion on the $\Delta P-v_i$ curve is presented based on parametric study performed for a typical BWR fuel bundle. Effects of several important parameters such as the heat flux, the inlet subcooling, the localized flow resistance, and the flow orientation are discussed.

Figure 6.1 explains the basic properties of the pressure drop in a heated channel. One of the distinguished characteristics of the two-phase flow is that it has higher pressure drop compared to single-phase flow with the same mass flow rate. Especially the frictional and the accelerational pressure drop components of the total channel pressure drop increases with decreasing flow rate. This is because of increasing in the flow quality with decreasing flow at fixed power input. Therefore, under certain conditions, the demand pressure drop curve may have a negative slope. The supply pressure drop or the pressure drop across the channel is constant for the parallel channel systems and natural circulation systems. This causes multiple steady-state solution exists. It is obvious that the solution on the negative-slope portion is stati-

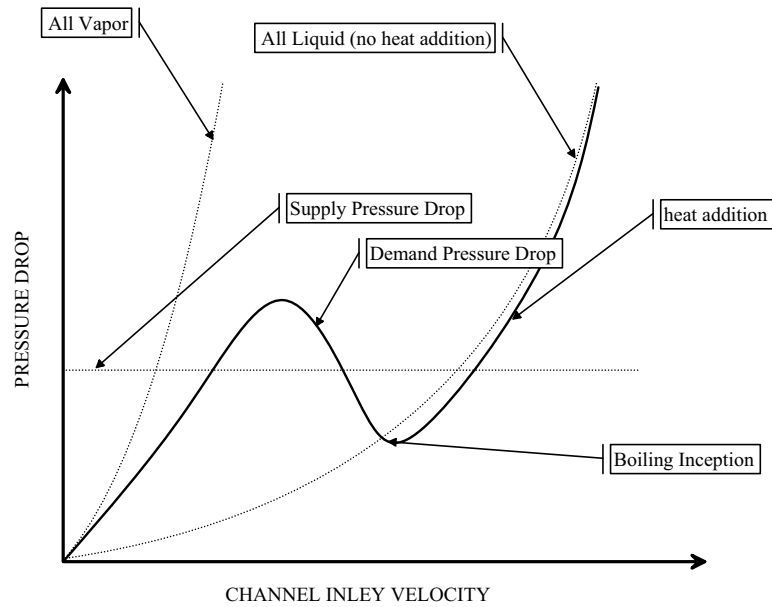


Figure 6.1. The Pressure Drop versus Flow Rate Curve

cally unstable because of the criterion given by Eq. (6.3).

For a typical BWR bundle geometry, the pressure drop components are shown in Figure 6.2. As the figure implies, the two-phase frictional and the accelerational pressure drop are the main cause of the s-shaped curve. However, the gravitational pressure drop component always tries to make the derivative of the curve positive in the upward flow systems. Therefore, gravity is stabilizing effect.

6.3.1 Effect of Heat Flux

The power input is the important parameter for the flow excursion since it determines the amount of void generation in the system. For understanding the effect of the heat flux on the pressure drop versus flow rate curve, several values of heat input are considered. Figure 6.3 clearly shows that increase in the heat flux enlarges the negative slope portion of the curve and makes the system more unstable. The starting point of s-shape shifts towards the higher flow rate as the heat flux increases. Since the s-shape curve may move up and down with the heat flux, and the channel demand pressure drop is more or less constant, system may have unstable steady-state solution by varying the heat flux.

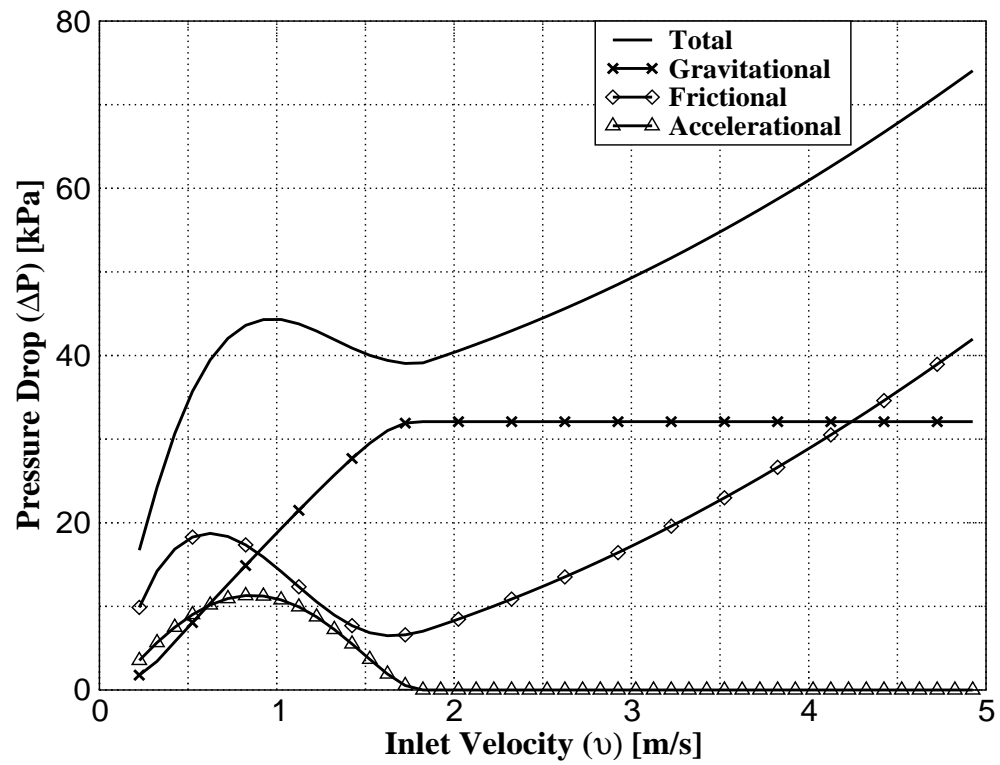


Figure 6.2. Pressure Drop Components for a Typical BWR Fuel Bundle

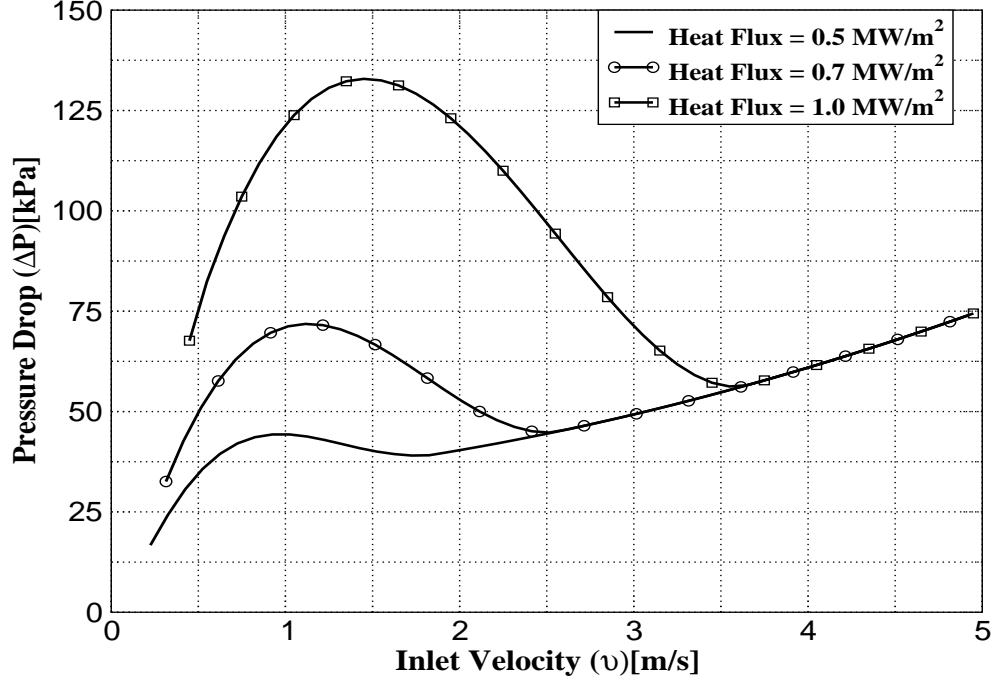


Figure 6.3. Effect of Heat Flux on ΔP - \dot{m} Curve

6.3.2 Effect of Inlet Subcooling

The inlet subcooling is another important parameter for the steady-state characteristics of a heated channel. It determines the single-phase length and the time-lag in the single-phase heated section. Figure 6.4 demonstrates the effect of the inlet subcooling on the pressure drop characteristics. It shows that increase in the inlet subcooling has the same effect as increasing the heat flux and is destabilizing effect.

6.3.3 Effect of Localized Flow Resistances

The localized flow resistances at the inlet and the exit of the bundle are examined. Figure 6.5 shows that large values of K_i eliminates the negative slope portion of the curve, while K_e increases the negative slope region on the curve. Obviously, increasing K_i is stabilizing effect on the flow excursion. However, as the figure demonstrates, the stability is paid by the pumping power requirements for a given flow rate because of the increase in the channel pressure drop.

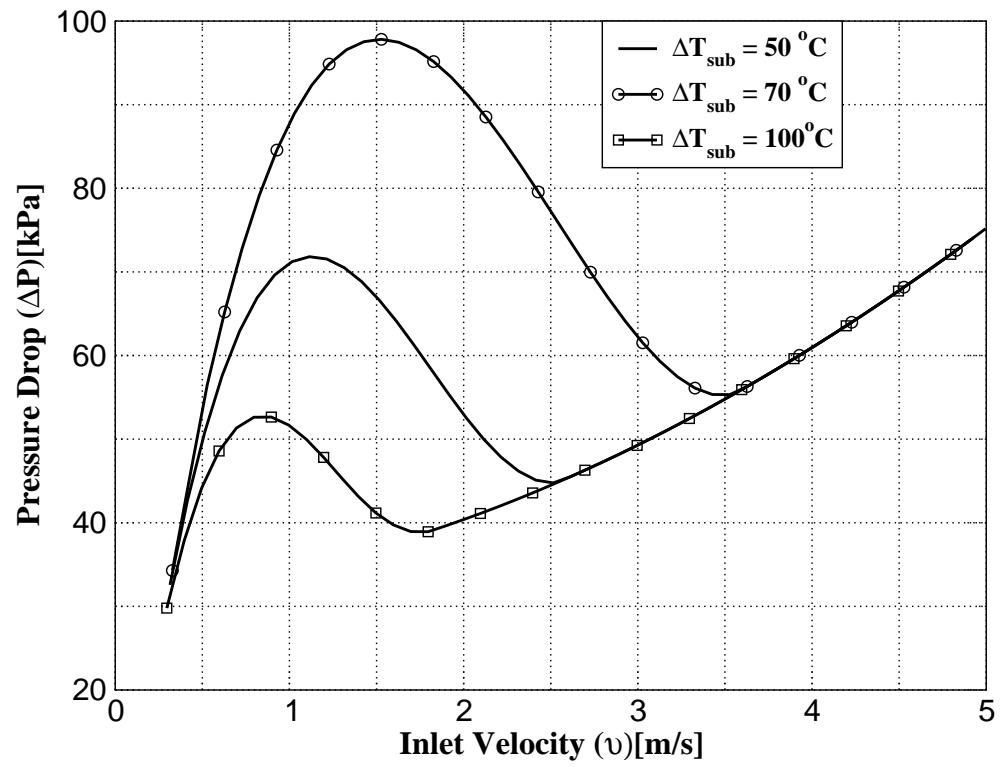
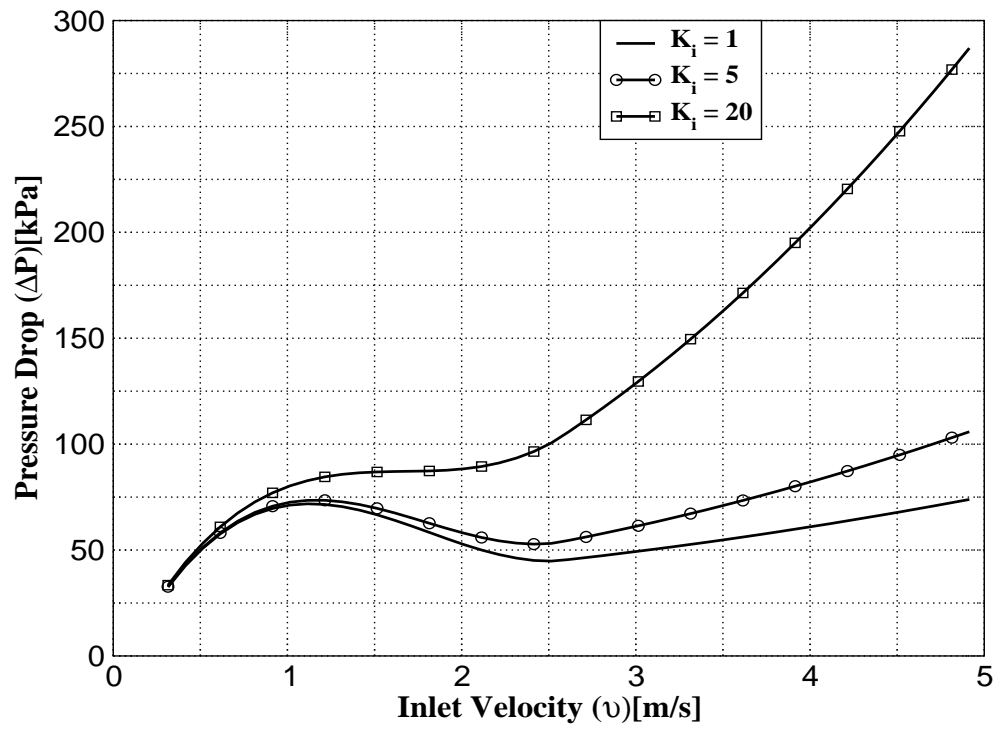
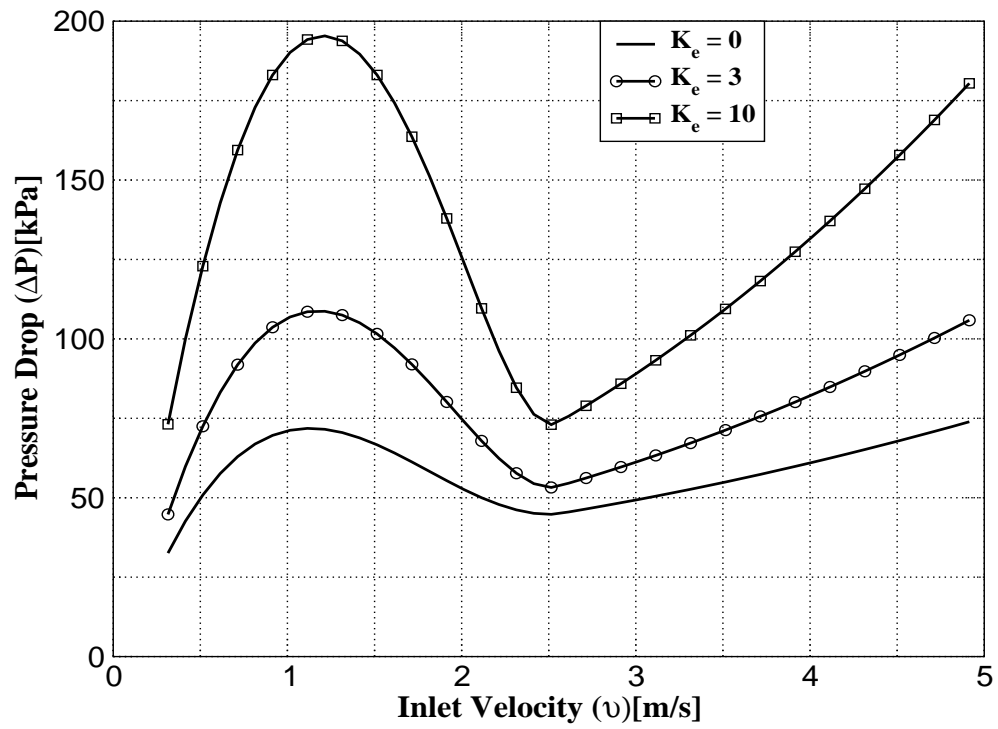


Figure 6.4. Effect of Inlet Subcooling on ΔP - \dot{m} Curve



(a) Effect of K_i



(b) Effect of K_e

Figure 6.5. Effect of Localized Flow Resistances on ΔP - \dot{m} Curve

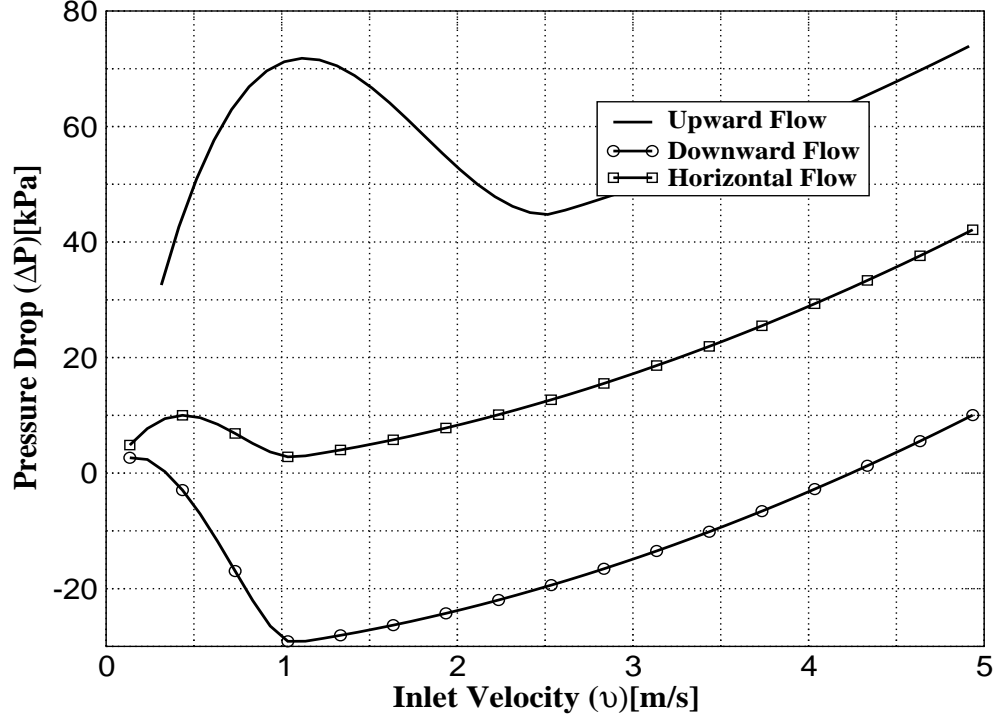


Figure 6.6. Effect of Gravity Field on ΔP - \dot{m} Curve

6.3.4 Effect of Channel Orientation

The effect of the gravity is investigated by considering three different flow orientations: Upward, Downward and Horizontal. Figure 6.6 demonstrates that the gravity in the upward flow is always stabilizing, because it has positive contribution to total pressure drop. In contrast to the upward flow, downward flow seems to be the most unstable flow configuration in terms of the flow excursion because of the inverse effect of the gravity field.

6.4 Stability Maps for Flow Excursion

The equation derived in Section 6.2 describes the stability of a given system in terms of the dimensionless groups. It is common practice to show the stability boundary on a suitable map. For the purpose, two different stability maps are introduced; Subcooling Number vs. Zuber Number and Zuber Number vs. Inverse of Froude Number Planes.

Table 6.1. Typical BWR Fuel Bundle Geometrical Data

Bundle Type	8×8 , Square Array
Hydraulic Diameter (m)	1.32×10^{-2}
Heated Perimeter (m)	2.52
Heated Height (m)	3.71
Flow Area (m ²)	100.9×10^{-4}

As an example for the forced circulation systems, a typical BWR fuel bundle is considered. The geometrical parameters for the bundle is presented in Table 6.1.

6.4.1 Subcooling Number versus Zuber Number Plane

The subcooling number vs. zuber number plane is well-known stability plane [12] and combines the effect of the subcooling, the channel power, the inlet velocity and the pressure in a single plane. The characteristic equation is solved by fixing the dimensionless numbers other than subcooling number and zuber number via bisection method. The detailed discussion about the characteristic equation and solution methodology are given in Appendix A. A typical stability map on the subcooling number vs. zuber number is shown in Figure 6.7. Two lines enclosing the unstable region represent the solution where $\frac{\partial \Delta P}{\partial v_i}$ is zero. Therefore, between the lines, the channel pressure drop has negative slope.

The first boundary on the left-hand-side of the $X_e = 0$ line is due to subcooled boiling initiated at the channel exit. In other words, the line can be considered as a separating line between the single-phase and the two-phase regions inside the channel. Since it is the indication of the starting point of the two-phase flow, from Saha-Zuber model, an equation can be written for that line which can also be used to estimate the flow excursion boundary. Assuming $N_{Pe} \geq 70000$ where departure enthalpy is hydraulically controlled, the following equation can be used to estimate the line

$$\frac{N_{sub}}{N_{Zu}} = 154 \frac{A_h}{\xi_h H_h} \quad (6.20)$$

Figure 6.8 shows the effect of subcooled boiling on prediction of flow excursion sta-

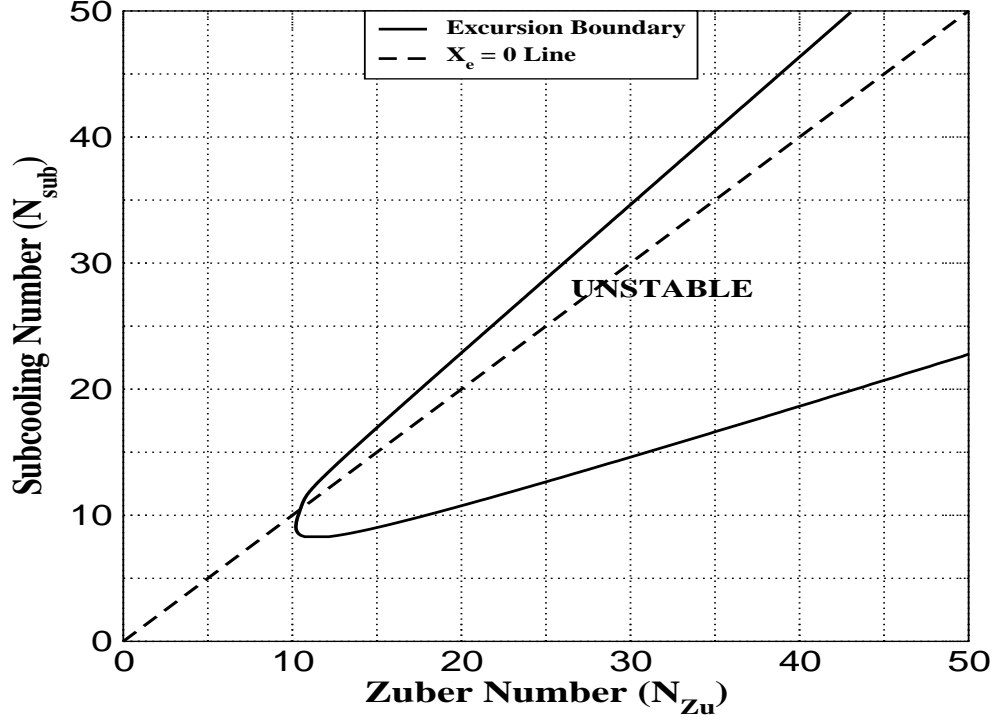


Figure 6.7. Stability on Subcooling Number –Zuber Number

bility boundary compared to the model which assumes thermodynamic equilibrium between the phases. The subcooled boiling should be included in the analysis of flow excursion, since neglecting subcooled boiling gives non-conservative estimation for stability boundary especially at high subcoolings.

When the thermodynamic equilibrium between the phase is assumes, unstable region starts when boiling starts at the channel exit which is given by $X_e = 0$ line. Similarly, first line can be estimated by the Saha-Zuber model for the departure enthalpy and provides good approximation for the stability boundary at high subcooling numbers.

6.4.2 Zuber Number versus Inverse of Froude Number

It has been shown that gravity is one of the important parameters in the flow excursion. Therefore, the stability boundary is expected to be strong function of the froude number which is the ratio of inertial to gravity forces. Zuber number vs. inverse of froude number plane is proposed for the flow excursion as an alternative

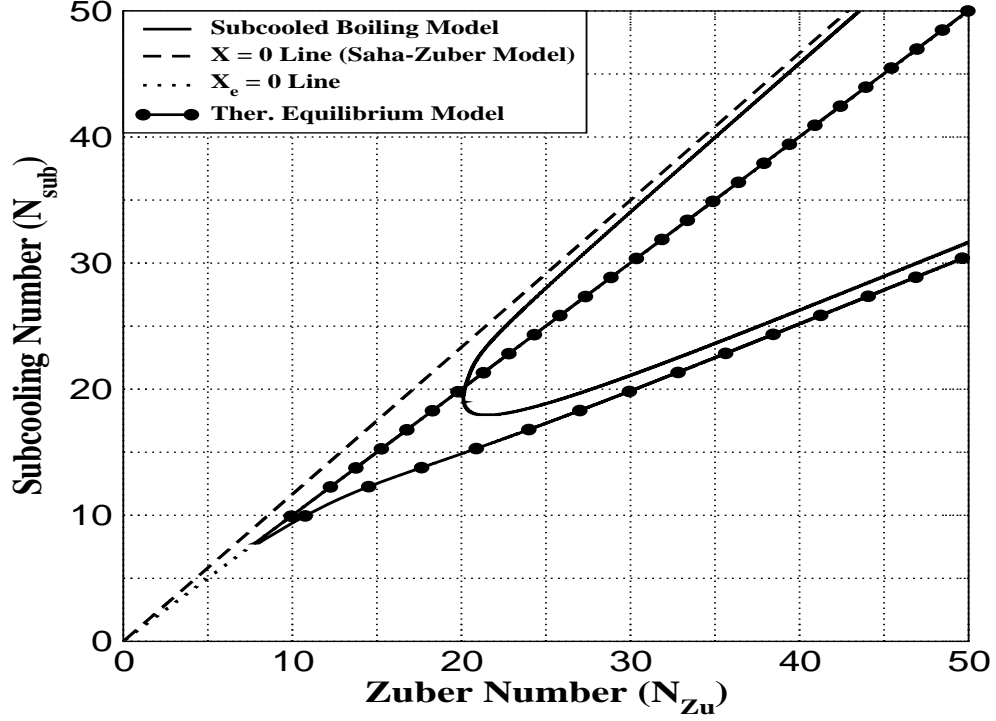


Figure 6.8. Effect of Subcooled Boiling on Flow Excursion Boundary

stability map. Inverse of the froude number is used as one of the axis of the map. A similar stability map can be generated by means of subcooling number instead of zuber number. In this case, the map shows the constant zuber number curves.

Figure 6.9 shows a typical stability map on the zuber number vs. inverse of the froude number plane. It is clearly shown that increasing the froude number is always destabilizing effect. This is basically due to decrease in the effectiveness of the gravity field. Since the froude number is proportional to the square of the velocity, increase in the froude number due to increase in the inertia is stabilizing due to decrease in the zuber number as can be seen from Figure 6.7. The same stability map can be generated for different subcooling numbers. Figure 6.10 shows the destabilizing effect of the inlet subcooling by enlarging the unstable region.

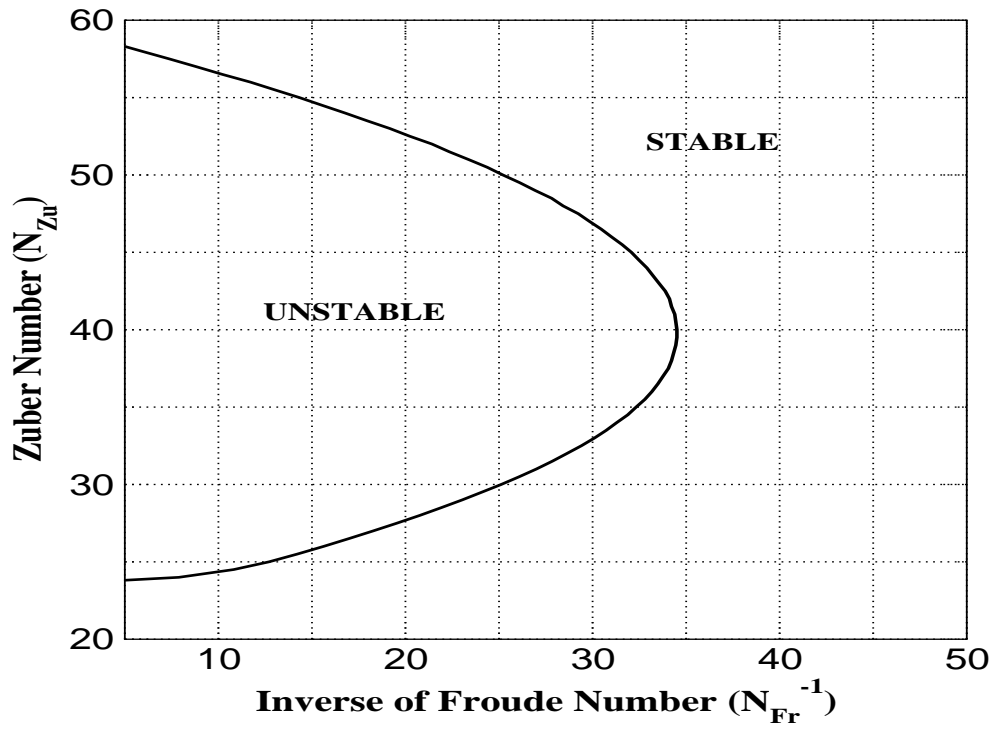


Figure 6.9. Stability on the Zuber Number – the Inverse of the Froude Number

Table 6.2. SBWR Geometrical Data

Bundle Type	8×8 , Square Array
Number of Fuel Bundle	732
Core Hydraulic Diameter (m)	1.97×10^{-2}
Core Heated Perimeter (m)	1694
Core Heated Height (m)	2.74
Core Flow Area (m^2)	7.4
Chimney Hydraulic Diameter (m)	0.5
Chimney Height (m)	9.1
Chimney Flow Area (m^2)	18.6

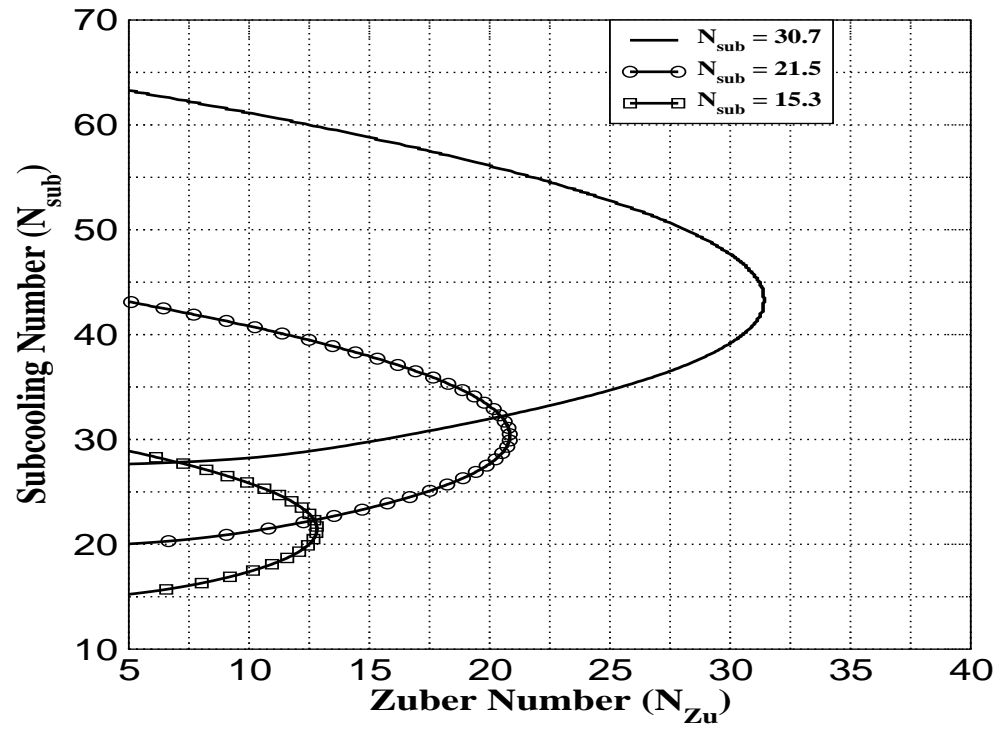


Figure 6.10. Stability on the Zuber Number – the Inverse of the Froude Number for Different Values of the Subcooling Number

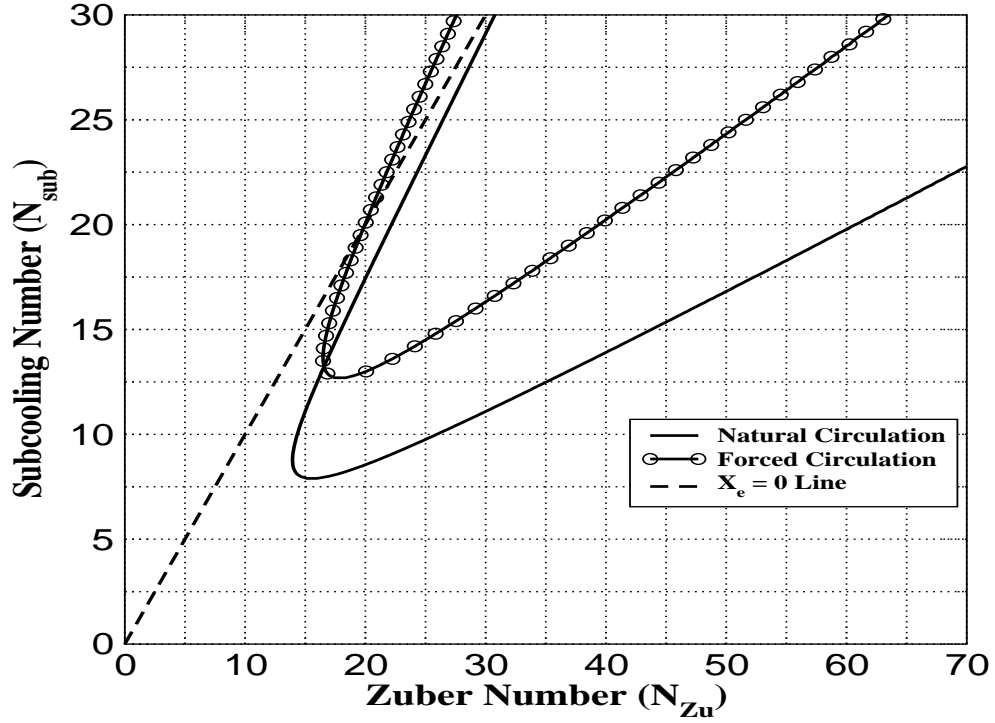


Figure 6.11. Flow Excursion Boundary in BWR and SBWR

6.5 Forced Circulation versus Natural Circulation

Figure 6.11 demonstrates the comparison of the flow excursion boundary between the BWR and SBWR. The geometrical information of the SBWR as an example of a natural circulation system is given in Table 6.2.

Figure 6.11 has shown that at high inlet subcooling, BWR is less stable than the SBWR. The first boundary appears at the smaller zuber number due to the subcooled boiling. In other words, the subcooled boiling is not important for the natural circulation systems as far as the flow excursion boundary is concerned. However, the natural circulation systems have larger negative slope region in the pressure drop curve provided by the unstable area in the figure. It can also be seen that as the subcooling becomes smaller, the natural circulation systems seem to be more stable. This simulation has been performed by keeping the K_i and K_e same.

7. NONLINEAR ANALYSIS OF NUCLEAR-COUPLED DWO

As discussed in Chapter 2, the frequency domain methods are useful tools when the stability boundary is needed in the operational plane either in dimensional or dimensionless form. However, these tools use small perturbation around steady state and neglects the second and higher order terms which represent the nonlinear effects in the system. Therefore, important nonlinear effects such as amplitude of the limit cycle oscillations are lost. In order to capture the physics of the nonlinear phenomena in the nuclear-coupled flow instabilities in BWRs, the time domain solution of the field equations representing several physical processes such as flow field, fuel heat conduction, and neutron kinetics need to be solved. In view of the difficulty of the problem in BWRs which require sophisticated time domain analysis tools, a simple model is derived in this chapter to understand the basic physical phenomenon underlying the nonlinear nature of the instability problem.

By introducing the Galarkin Weighted Residual Method, the field equations governing the flow field (Chapter 3), fuel heat conduction (Chapter 4), and neutron kinetics (Chapter 5) are transformed to a system of nonlinear ordinary differential equation (ODE). In this chapter, the basic procedure to derive the equations for each field is described. In the following section, the introductory information about the Galarkin Method is presented.

7.1 Galarkin Weighted Residual Method

The field equations which are described in the following section, the governing partial differential equation (i.e., flow field equations) can be written in a general form as follows:

$$\mathbb{H}\Phi(z, t) = \mathbb{S}(z, t) \tag{7.1}$$

where \mathbb{H} represents the operator for the partial differential equation considered in the problem. For instance, for a first order wave equation (liquid enthalpy wave, mixture density wave), it is written in a general way as,

$$\mathbb{H} \triangleq \frac{\partial}{\partial t} + V \frac{\partial}{\partial z} \quad (7.2)$$

where V represents the wave velocity by which the disturbances are propagated. In Eq. (7.1), \mathbb{S} denotes the source term.

The following approximate function is used to represent the solution of Eq. (7.1):

$$\Phi(z, t) \approx \Phi'(z, t) = \Phi_o(t) + \sum_{i=1}^N \Phi_i(t) \Psi_i(z) \quad (7.3)$$

where $\Phi_i, i = 1 \dots N$ represents the time dependent coefficients and $\Psi_i, i = 1 \dots N$ denotes the spatial dependency of the solution. When Eq. (7.3) is inserted into Eq. (7.1), the residual equation can be derived as follows:

$$\mathbb{R}(z, t) = \mathbb{H}\Phi'(z, t) - \mathbb{S}(z, t) \quad (7.4)$$

which is not equal to zero since the function $\Phi'(z, t)$ is not the solution of the system. However, the coefficients, $\Phi_i, i = 1 \dots N$, can be determined in such a way that the residual in Eq. (7.4) is minimized. The coefficient, $\Phi_o(t)$, is given based on the boundary condition for Eq. (7.1).

The residual equation given by Eq. (7.4) can be minimized by multiplying the equation with appropriated weighting functions, $\Xi_i(z), i = 1 \dots N$ and integrating over the domain of interest. By evaluating the following integral, the ODEs for the coefficients, $\Phi_i, i = 1 \dots N$ can be determined:

$$(\mathbb{R}, \Xi_i) = 0 \quad (7.5)$$

where $(,)$ is the inner-product operator for the two functions, $F(z), G(t)$, given as

follows:

$$(F, G) = \int_D F(z)G(z)dz \quad (7.6)$$

where D represents the domain of interest.

In the following sections, the set of ODEs for the flow field, fuel heat conduction, and neutron kinetics is derived for the nonlinear dynamics of nuclear-coupled instabilities in BWR systems.

7.2 Flow Field Formulation

The detailed discussion has been presented in Chapter 3 about the basics of flow field formulation in dimensionless form ¹. In this section, the necessary equations for the nonlinear dynamics are derived based on Galarkin Weighted Residual Method described in Section 7.1. However, for the purpose of analysis, some simplifying assumptions are used. The mechanical and thermal equilibrium between the phases are assumed. Therefore, the drift number, N_d and subcooled boiling number, N_{sd} are set to zero. In the following sections, the details of the derivation are presented. First, the single phase energy equation, which shows the propagation of the enthalpy wave in the single phase heated section, is solved to determine the boundary between the single and two-phase mixture section in a heated channel. Once the equation for the boiling boundary is determined, the density wave equation given by Eq. (3.55) is solved to obtain the mixture density or void fraction along the heated channel. By knowing the boiling boundary and the mixture density, the dimensionless momentum equations for the heated channel can be integrated.

At steady-state condition, it has been shown that the mixture density is spatially constant in the unheated section. However, during the transient where the heated section exit mixture density oscillates, the mixture density is also a function of the space due to the void wave propagation. Therefore, the mixture density in the unheated section should also be solved.

¹In this chapter, the asterisk sign (*) is removed from the dimensionless equations. Throughout the chapter, all parameters should be understood as dimensionless

7.2.1 Boiling Boundary Dynamics

The single phase energy equation in dimensionless form is given by Eq. (3.49). In this equation, $\Omega_{1\phi}$, represents the reaction frequency in single phase heated region which is given in terms of the wall heat flux. The formulation for the wall heat flux is described in Chapter 4. It is important to mention here that the wall heat flux is assumed spatially constant considering uniform wall heat generation and averaged bulk liquid temperature.

The following polynomial of degree N_1 is used to describe the general solution to Eq. (3.49):

$$N_s(z, t) \approx N_{sin}(t) + N_{s1}(t)z + \dots + N_{sN_1}(t)z^{N_1} = N_{sin}(t) + \sum_{i=1}^{N_1} N_{si}z^i \quad (7.7)$$

where $N_{sin}(t)$ represents the inlet subcooling which is introduced as a boundary condition for the problem. By choosing the weighting function as $z^i, i = 0 \dots N_1 - 1$, and integration domain as $[0, \lambda(t)]$, the equation for the coefficients can be determined. The equation can be written in matrix-vector form as follows:

$$M_{1\phi} \frac{d\vec{N}_s}{dt} = \vec{b}_{1\phi} \quad (7.8)$$

where the generic elements for the matrix, $M_{1\phi}$ and the vector, $\vec{b}_{1\phi}$ can be written as follows:

$$[M_{1\phi}]_{i,j} \triangleq \frac{\lambda^{i+j}(t)}{i+j} \quad (7.9a)$$

$$[b_{1\phi}]_i \triangleq - \left(\frac{dN_{sin}}{dt} + \Omega_{1\phi}(t) \right) \frac{\lambda(t)^i}{i} - v_{fin}(t) \sum_{k=1}^{N_1} \frac{k\lambda^{k+i-1}(t)}{k+i-1} N_{sk}(t) \quad (7.9b)$$

where the vector, \vec{N}_s in Eq. (7.8) is given as $\vec{N}_s = [N_{s1} \dots N_{sN_1}]^T$.

The boiling boundary, $\lambda(t)$, in Eq. (7.9a) can be determined by solving Eq. (7.7) for $\lambda(t)$ with given boundary condition, $N_s(\lambda(t), t) = 0$. Another method of deriving an equation for the boiling boundary dynamics is to differentiate Eq. (7.7) with respect

to time after inserting $z = \lambda(t)$ in to the equation. The following equation can be easily derived for the boiling boundary:

$$\left(\sum_{i=1}^{N_1} i \lambda^{i-1}(t) N_{si}(t) \right) \frac{d\lambda}{dt} = -\frac{dN_{sin}}{dt} - \sum_{i=1}^{N_1} \frac{dN_{si}}{dt} \lambda^i(t) \quad (7.10)$$

Equation (7.10) is coupled to Eq. (7.8). However, a simpler boiling boundary dynamics equation can be derived by assuming linear enthalpy profile and constant inlet subcooling. The resulting equation can be written as follows:

$$\frac{d\lambda}{dt} = 2v_{fin}(t) - 2\frac{\Omega_{1\phi}(t)}{N_{sub}}\lambda(t) \quad (7.11)$$

where N_{sub} is the subcooling number given by Eq. (3.58). The detailed derivations related to the boiling boundary can be found in Appendix B.

7.2.2 Mixture Density and Velocity in Two-phase Mixture Regions

By assuming mechanical and thermal equilibrium between the phases, the equation for the mixture density in the heated section can be written as follows:

$$\frac{\partial v_m}{\partial z} = \Omega_{2\phi}(t) \quad (7.12)$$

which can be easily integrated by supplying the boundary condition at the boiling boundary, $v_m(\lambda(t), t) = v_{fin}(t)$ to obtain the solution as,

$$v_m(z, t) = v_{fin}(t) + \Omega_{2\phi}(t)(z - \lambda(t)) \quad (7.13)$$

where $\Omega_{2\phi}$ is the reaction frequency in the two-phase mixture heated section. It is determined via solving the heat conduction equation.

The density wave equation in the heated section can be simplified as follows:

$$\frac{\partial \rho_m}{\partial t} + v_m \frac{\partial \rho_m}{\partial z} = -\Omega_{2\phi} \rho_m \quad (7.14)$$

which can be rewritten as $\mathbb{H}_{2\phi}\rho_m(z, t) = 0$. The operator, $\mathbb{H}_{2\phi}$ is defined as

$$\mathbb{H}_{2\phi} \triangleq \frac{\partial}{\partial t} + v_m \frac{\partial}{\partial z} + \Omega_{2\phi} \quad (7.15)$$

For the solution of the mixture density in the heated section, the following N_2^{th} degree polynomial is proposed as an approximate solution:

$$\rho_m(z, t) \approx \rho'_m(z, t) = 1 + \sum_{i=1}^{N_2} \rho_{mi}(t) \theta^i \quad (7.16)$$

where $\theta = z - \lambda(t)$ is the position in the heated mixture region. By choosing the weighting function as $\theta^i, i = 0 \dots N_2 - 1$ and performing the integration for the residual equation, the following set of equation can be obtained for the coefficients in Eq. (7.16):

$$M_{2\phi} \frac{d\vec{\rho}_m}{dt} = \vec{b}_{2\phi} \quad (7.17)$$

where the generic elements for the matrix, $M_{1\phi}$ and the vector, $\vec{b}_{1\phi}$ can be written as follows:

$$[M_{1\phi}]_{i,j} \triangleq \frac{\theta_1^{i+j}(t)}{i+j} \quad (7.18a)$$

$$\begin{aligned} [b_{2\phi}]_i &\triangleq \left(\sum_{k=1}^{N_2} \frac{k\theta_1^{k+i-1}}{k+i-1} \rho_{mk}(t) \right) \left(\frac{d\lambda}{dt} - v_{fin}(t) \right) \\ &- \Omega_{2\phi}(t) \left(\frac{(k+1)\theta_1^{k+i}}{k+i} \rho_{mk}(t) + \frac{\theta_1^i}{i} \right) \end{aligned} \quad (7.18b)$$

where the vector, $\vec{\rho}_m$ in Eq. (7.17) is given as $\vec{\rho}_m = [\rho_{m1} \dots \rho_{mN_2}]^T$.

In the unheated section, the mixture velocity is spatially uniform as can be seen from Eq. (7.12) since $\Omega_{2\phi}$ becomes zero. However, the mixture density is a function of the spatial coordinate due to wave propagation. Therefore, solution of Eq. (7.14) is needed to define the two-phase flow in the unheated section. The following polynomial

of degree N_3 is used for the solution:

$$\rho_{m,uh}(z, t) \approx \rho'_m(z, t) = \rho_{me}(t) + \sum_{i=1}^{N_2} \rho_{m,uhi}(t) z^i \quad (7.19)$$

where $\rho_{me}(t)$ is the heated section exit mixture density. The integration domain for the unheated mixture section for computing the equation for the coefficient of Eq. (7.19) is $[0, l_{uh}]$. The parameter, l_{uh} , is the dimensionless unheated section height. The general equation for the coefficients can be determined in a similar way performed for the coefficients in the heated mixture region. In the matrix-vector form, the general equation for the unheated mixture density coefficients is given as follows:

$$M_{2\phi,uh} \frac{d\vec{\rho}_{m,uh}}{dt} = \vec{b}_{2\phi,uh} \quad (7.20)$$

where the generic elements for the matrix, $M_{1\phi}$ and the vector, $\vec{b}_{1\phi}$ can be written as follows:

$$[M_{2\phi,uh}]_{i,j} \triangleq \frac{l_{uh}^{i+j}}{i+j} \quad (7.21a)$$

$$[b_{2\phi,uh}]_i \triangleq -v_{m,uh} \sum_{k=1}^{N_3} \frac{k l_{uh}^{k+i-1}}{k+i-1} \rho_{m,uhk}(t) - \frac{l_{uh}^i}{i} \frac{d\rho_{me}}{dt} \quad (7.21b)$$

where the vector, $\vec{\rho}_{m,uh}$ in Eq. (7.20) is given as $\vec{\rho}_{m,uh} = [\rho_{m,uh1} \dots \rho_{m,uhN_2}]^T$. The heated section mixture density, $\rho_{me}(t)$, is given by

$$\rho_{me} = 1 + \sum_{i=1}^{N_2} \rho_{mi}(t) \theta_1^i \quad (7.22)$$

where $\theta_1 = 1 - \lambda(t)$ is the boiling length of the channel or the length of the heated mixture region. The mixture velocity in the unheated section is spatially uniform and from the continuity requirements it can be written as follows:

$$v_{m,uh}(t) = \frac{1}{A_{uh}} (v_{fin}(t) + \Omega_{2\phi}(t) \theta_1(t)) \quad (7.23)$$

7.2.3 Flow Dynamics

The dynamic characteristics of the flow can be determined by integrating the momentum equation over the heated and unheated section to yield an equation for the inlet velocity, $v_{fin}(t)$. By using the constant pressure drop boundary condition across the heated and unheated sections, $\Delta P_h + \Delta P_{uh} = \Delta P_o$, the following equation can be obtained for the inlet velocity:

$$\begin{aligned} I(t) \frac{dv_{fin}}{dt} &= \Delta P_o \\ &- \frac{d\Omega_{2\phi}}{dt} \left(\frac{\theta_1^2}{2} + \sum_{i=1}^{N_2} \frac{\theta_1^{i+1}}{i+1} \rho_{mi}(t) + \frac{\theta_1}{A_{uh}} \left(\rho_{me}(t) l_{uh} + \sum_{i=1}^{N_3} \frac{l_h^{i+1}}{i+1} \rho_{m,uhi}(t) \right) \right) \\ &+ \Omega_{2\phi}(t) \frac{d\lambda}{dt} \left(\theta_1 + \sum_{i=1}^{N_2} \frac{\theta_1^{i+1}}{i+1} \rho_{mi}(t) + \frac{1}{A_{uh}} \left(\rho_{me}(t) l_{uh} + \sum_{i=1}^{N_3} \frac{l_h^{i+1}}{i+1} \rho_{m,uhi}(t) \right) \right) \\ &- \Delta P_{sa}(t) - \Delta P_{fr}(t) - \Delta P_{gr}(t) - \Delta P_{form} \end{aligned} \quad (7.24)$$

where $I(t)$ is the inertia of the flow which is given as follows:

$$I(t) = 1 + \sum_{i=1}^{N_2} \frac{\theta_1^{i+1}}{i+1} \rho_{mi}(t) + \frac{1}{A_{uh}} \left(\rho_{me}(t) l_{uh} + \sum_{i=1}^{N_3} \frac{l_{uh}^{i+1}}{i+1} \rho_{m,uhi}(t) \right) \quad (7.25)$$

In Eq. (7.24), ΔP_{sa} denotes the convective acceleration. ΔP_{fr} , ΔP_{gr} represents the frictional and gravitational pressure drop components along the heated and unheated sections. The last term on RHS of Eq. (7.24) represents the localized pressure drop. The detailed expressions for the pressure drop components are given in Appendix C.

7.3 Fuel Heat Conduction Equations

The detailed discussion about the heat conduction process inside a typical BWR fuel element has been presented in Chapter 4 where the governing equations for the fuel heat conduction equation are transformed. For the formulation of the problem, the single-node lumped model is used. The field equations are reproduced here as follows:

$$\frac{d\theta_{1\phi}}{dt} = \frac{n(t)}{\langle \rho c \rangle_{fe} A_{fe}} - a_{fe,1\phi} \left(\theta_{1\phi} + \frac{N_{sin}(t)}{2} \right) \quad (7.26a)$$

$$\frac{d\theta_{2\phi}}{dt} = \frac{n(t)}{\langle \rho c \rangle_{fe} A_{fe}} - a_{fe,2\phi} \theta_{2\phi} \quad (7.26b)$$

where a_{fe} is the dimensionless thermal diffusivity defined for both single and two-phase mixture section of the heated channel. The detailed expressions for a_{fe} in each section are described in Chapter 4. However, the expression for the reaction frequencies, $\Omega_{1\phi}$ and $\Omega_{2\phi}$, are given here. In addition to the reaction frequencies, the derivative of the reaction frequency in two-phase mixture region appears in Eq. (7.24) needs to be derived.

The reaction frequency in the single phase region, $\Omega_{1\phi}$ is given by the following equation:

$$\Omega_{1\phi} = \langle \rho c \rangle_{fe} A_{fe} a_{fe,1\phi} \left(\theta_{1\phi}(t) + \frac{N_{sin}(t)}{2} \right) \quad (7.27)$$

The dimensionless thermal diffusivity is a function of the heat transfer coefficient in the single phase heated section. The heat transfer coefficient, $h_{1\phi}$, is a function of the inlet velocity as shown in Eq. (4.25). In the two-phase mixture region, the reaction frequency is given by

$$\Omega_{2\phi} = \langle \rho c \rangle_{fe} A_{fe} a_{fe,2\phi} \theta_{2\phi} \quad (7.28)$$

The derivative of Eq. (7.28) can be written by assuming the time rate of change in the heat transfer coefficient, $h_{2\phi}$ in two-phase mixture region is small as follows:

$$\frac{d\Omega_{2\phi}}{dt} = \langle \rho c \rangle_{fe} A_{fe} a_{fe,2\phi} \frac{d\theta_{2\phi}}{dt} \quad (7.29)$$

where the time dependency in $a_{fe,2\phi}$ is taken into account via Eq. (4.27).

7.4 Neutron Kinetics

The neutron kinetic is modeled through the PKM as described in Chapter 5. The time rate of change in the volumetric heat generation term is described by the function $n(t)$, which is the neutron amplitude function represented with Eq. (5.5a). The delayed neutron source is represented via precursor concentration equation given by Eq. (5.5b). Two important parameters in the neutron kinetics model are void-

reactivity and Doppler reactivity feedback. In order to compute the feedback reactivities, the axial-averaged void fraction and fuel temperature are defined. The averaged void-fraction for the channel is given in terms of the mixture density coefficients described in Section 7.2.2 as follows:

$$\langle \alpha \rangle_z(t) = \frac{1}{\theta_1(N_\rho - 1)} \sum_{i=1}^{N_2} \frac{\theta_1^{i+1}}{i+1} \rho_{mi}(t) \quad (7.30)$$

where $\theta_1 = 1 - \lambda(t)$ is the boiling length and N_ρ is the density ratio number. The averaged fuel temperature is defined as follows:

$$\langle \theta \rangle_z(t) = (1 - \lambda(t))\theta_{2\phi}(t) + \lambda(t)\theta_{1\phi}(t) \quad (7.31)$$

By considering the void fraction-dependent void reactivity coefficient, $K_\alpha(\alpha)$ and constant Doppler reactivity coefficient, K_D , the total reactivity, $\rho(t)$, in Eq. (5.5a) can be written as follows:

$$\rho(t) = \rho_{ext}(t) + \int_{\langle \alpha_o \rangle_z}^{\langle \alpha \rangle_z(t)} K_\alpha(\alpha) d\alpha + K_D(\langle \theta \rangle_z(t) - \langle \theta_o \rangle_z) \quad (7.32)$$

7.5 ODE Set for the Nonlinear Dynamics

The equations derived in previous section can be written as a system of equation as follows:

$$\frac{d\vec{X}}{dt} = \vec{F}(\vec{X}; \vec{\gamma}) \quad (7.33)$$

where the vector \vec{X} represents the state variables for which the ODEs are derived. Therefore, it is a vector of $N_1 + N_2 + N_3 + 11$ dimensions: N_1 equations for $N_{si}, i = 1 \dots N_1$, single equation for $\lambda(t)$, N_2 equations for $\rho_{mi}, i = 1 \dots N_2$, N_3 equations for $\rho_{m,uhi}, i = 1 \dots N_3$, single equation for $v_{fin}(t)$, single equation for $\theta_{1\phi}$, single equation for $\theta_{2\phi}$, single equation for $n(t)$, and finally six equations for $\xi_i(t), i = 1 \dots 6$. The vector, $\vec{\gamma}$ represents the dimensionless numbers such as N_{Zu} , N_{sub} , N_ρ , N_f , N_{Fo} , etc., representing the operational state of the system in terms of steady-state values.

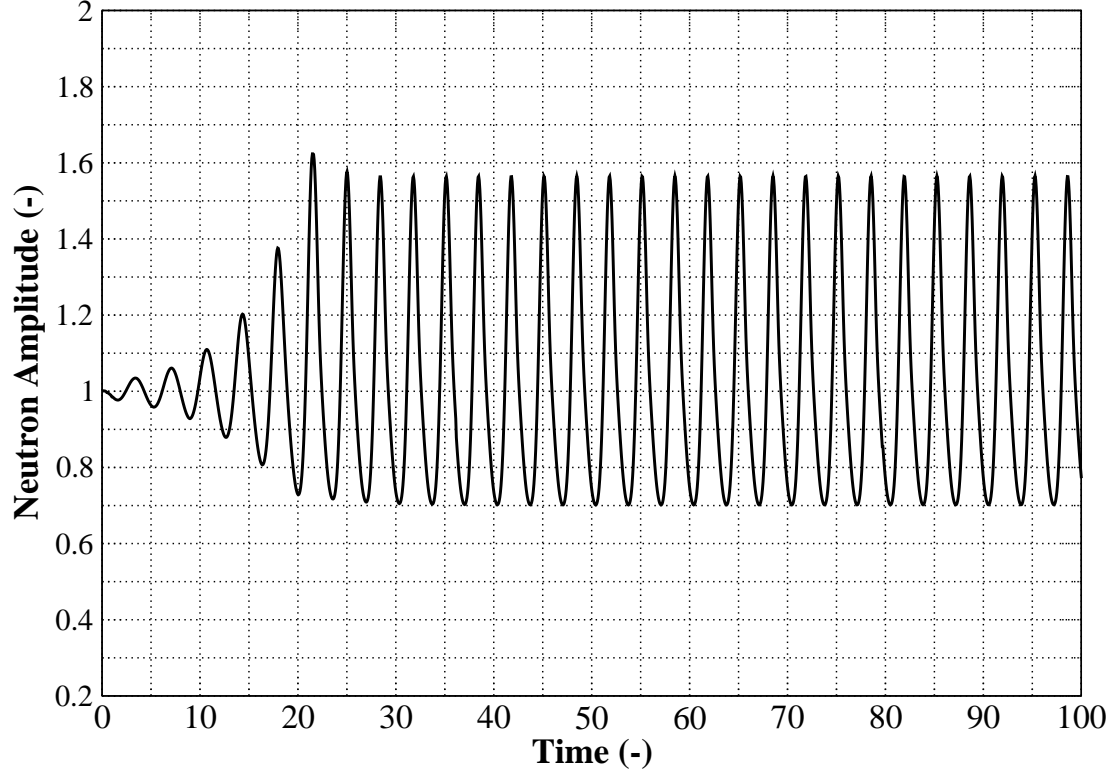


Figure 7.1. Neutron Flux Oscillations inside the Linearly Unstable Region

The model developed in this chapter is used to investigate the nuclear-coupled flow instabilities in a typical BWR fuel bundle. Figure 7.1 demonstrates a typical limit-cycle oscillations which can be observed in unstable region which is determined by frequency domain tools. The limit-cycle is directly related to the nonlinear effects inherent to the nature of the problem. Even though the system is linearly unstable, the indefinite grow of oscillations are inhibited due to the nonlinearities. This can also be viewed from phase portraits where nonlinear effects can be seen clearly. For the purpose, the phase plane composed of the neutron amplitude function and its derivative is demonstrated in Figure 7.2.

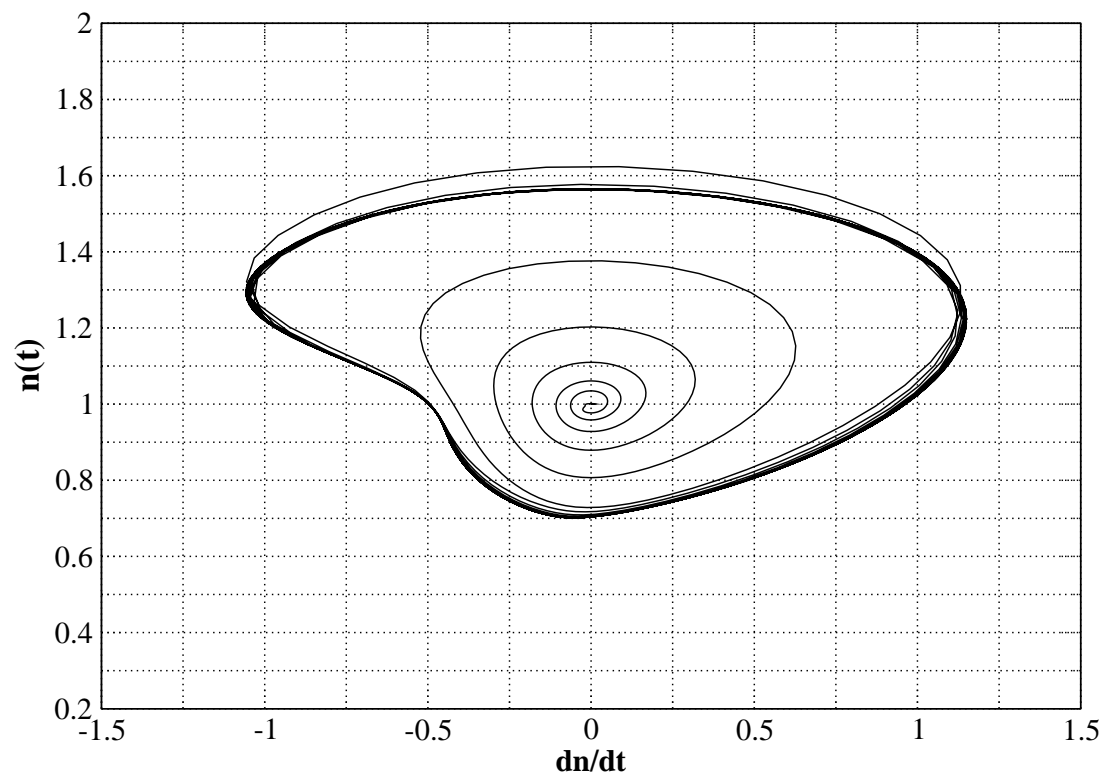


Figure 7.2. Limit-cycle Oscillation in a Phase Plane

Part II

Experimental Study

8. EXPERIMENTAL FACILITY

An experimental facility has been designed and built to study thermal-hydraulic instabilities and characterize the phenomena with hydrodynamic, kinematic and thermal parameters. The measured parameters are area-averaged instantaneous void fraction, temperature, pressure, pressure differential across certain section of the loop, liquid flow rate, heater power. The facility is a scaled prototypic BWR based on scaling criteria for geometric, hydrodynamic and thermal similarities. The experimental facility, test section, instrumentation and data acquisition system are described in this chapter.

8.1 Experimental Loop Layout

The experimental facility is mainly composed of a test section, bypass channel, condenser/cooler, main tank, expansion tank, preheater and pump. The general layout of the facility is shown in figure 8.1. Test section simulates the typical BWR fuel channel with a single fuel rod. The large bypass channel incorporated parallel to the test section. It provides constant pressure drop boundary condition for the test section by allowing most of the flow through the bypass channel. The constant pressure drop boundary condition is typical hydrodynamic boundary condition for BWR instabilities. Especially, during oscillations where large number of fuel channels are stable and few of them oscillate, this type of boundary condition is applicable. It is also valid when out-of-phase oscillations are observed.

Large water volume is kept inside the main tank. The water is pumped from this tank by a G&L SSH pump, and divided into bypass line and test section after the preheater. The water can be mixed with air before it is injected into the test section to calibrate the impedance meters, which are used for area-averaged void fraction measurement. Air supply also provides the capability of performing air-water

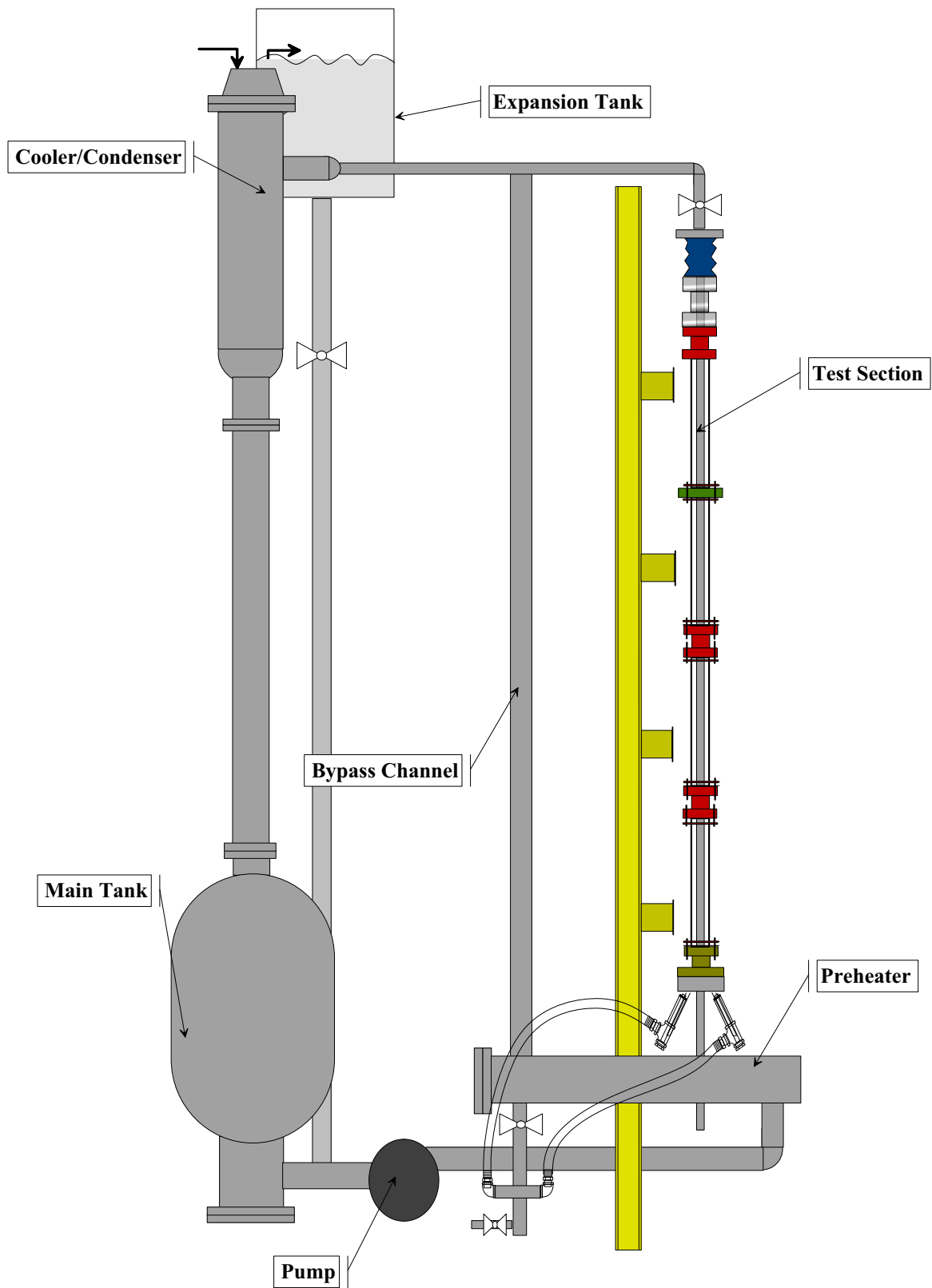


Figure 8.1. Experimental Loop Layout

experiments in an annular channel. Preheater power can be setup to provide variable heating for given set temperature or it can be adjusted manually through computer. The test section is annular geometry which is built by PYREX glass pipes on the outside and a cartridge heater on the inside. The air-water mixture flows through the vertical test section. However, for the diabatic steam-water flow, flow enters with a certain amount of subcooling, which is controlled by preheater and cooling water flow rate. The boiling starts after certain point and two-phase flow region starts. The steam-water flow then mixes with single-phase bypass flow and enters the condenser located at the top section of the facility. The condensate flows downward toward the main tank and pumped through the test section and bypass line.

The bypass section is made of 3.81 cm stainless steel pipe, providing 13.83 cm^2 of flow area. The bottom of the pipe is directly connected preheater inlet with a hose of length 60 cm. The bypass channel ensures that stable single-phase liquid flows through the section so that it can provide constant pressure differential across the test section. The magnetic flow meter is located on the middle of the bypass pipe to measure the volumetric flow rate of liquid.

The main holding tank for the subcooled water is 600 gal. stainless steel tank. The tank is cylindrical and oriented vertically. There are two penetrations on the top and bottom. The 101.6 mm I.D. top penetration is connected to the condensate return line, and the 152.4 mm I.D. bottom penetration is connected to the pump inlet. A K-type thermocouple is installed at the pump inlet to measure the tank water temperature.

The pump is an AISI 316L stainless steel pump manufactured by G&L Pumps. It is controlled with a Toshiba S7 Adjustable Speed Drive. Following the pump exit, the pipe is divided into test section flow and bypass flow through preheater. The preheater is a process heater made by Gaumer Company, Inc. The 18 kW heater is built in a 7.62 cm stainless steel pipe with a length of 136 cm. The heater is powered with a three phase 480 VAC source. A flexible pipe is installed between pump inlet and pipe coming from main tank to reduce the vibrations. Flow rate through test

section and bypass are measured with two Honeywell MagneW-3000 magnetic flow meters. The main flow is directed toward the test section with four separate line made of 25.04 mm hose to make test section inlet flow uniform.

8.2 Test Section

A detailed schematic view of the test section is demonstrated in figure 8.2. The test section flow is diverted via four separate lines. The air supply line is integrated on each line via Mott type 850 sparger element made of stainless steel. The spargers have overall length of 152.4 mm with a 95.3 mm porous length. Air comes from a regulated laboratory supply. The supply air tank provides a constant supply of air at 896 kPa. A regulator and filter are placed in-line to provide a variable line pressure. The regulator is a Norgren Excelon in-line filter-regulator. The air then flows into a set of rotameters that control the flow rate of air into the spargers. The rotameters are ranged 7.87 to 39.3 cm³/s, 23.6 to 157 cm³/s and 47.2 to 787 cm³/s. These rotameters are accurate to $\pm 10\%$ scale. A pressure gauge is used to measure the line backpressure. The air line leaves the pressure gauge and is divided into four separate lines. Each line is connected to a gas sparger. Air and water lines are connected to lower injection flange via four nipples, which are connected at 30° normal to the flange bottom. The center of the cylinder has a 19.1 mm hole cut through it to allow insertion of heater rod through the bottom flange into the test section. O-rings are used to seal the connection of the heater rod and the flange. A strip heater is wrapped around the flange to prevent heat loss. The strip heater is controlled with a solid-state relay on a 120 VAC line. The solid-state relay is controlled with a Dwyer model 15010 PID process controller and a thermocouple is placed between the heater and the flange to provide a feedback loop. The flange is also insulated against heat loss using fiberglass insulation.

The test section is mainly made of four transparent QVF conical pipes of length 60.69 cm. One polycarbonate pipe added to the test section for adjustment, as well as three impedance probes inserted between these pipes. The total height of the test section is 331.5 cm. Each glass pipe has 38.1 mm I.D. The maximum pressure of the

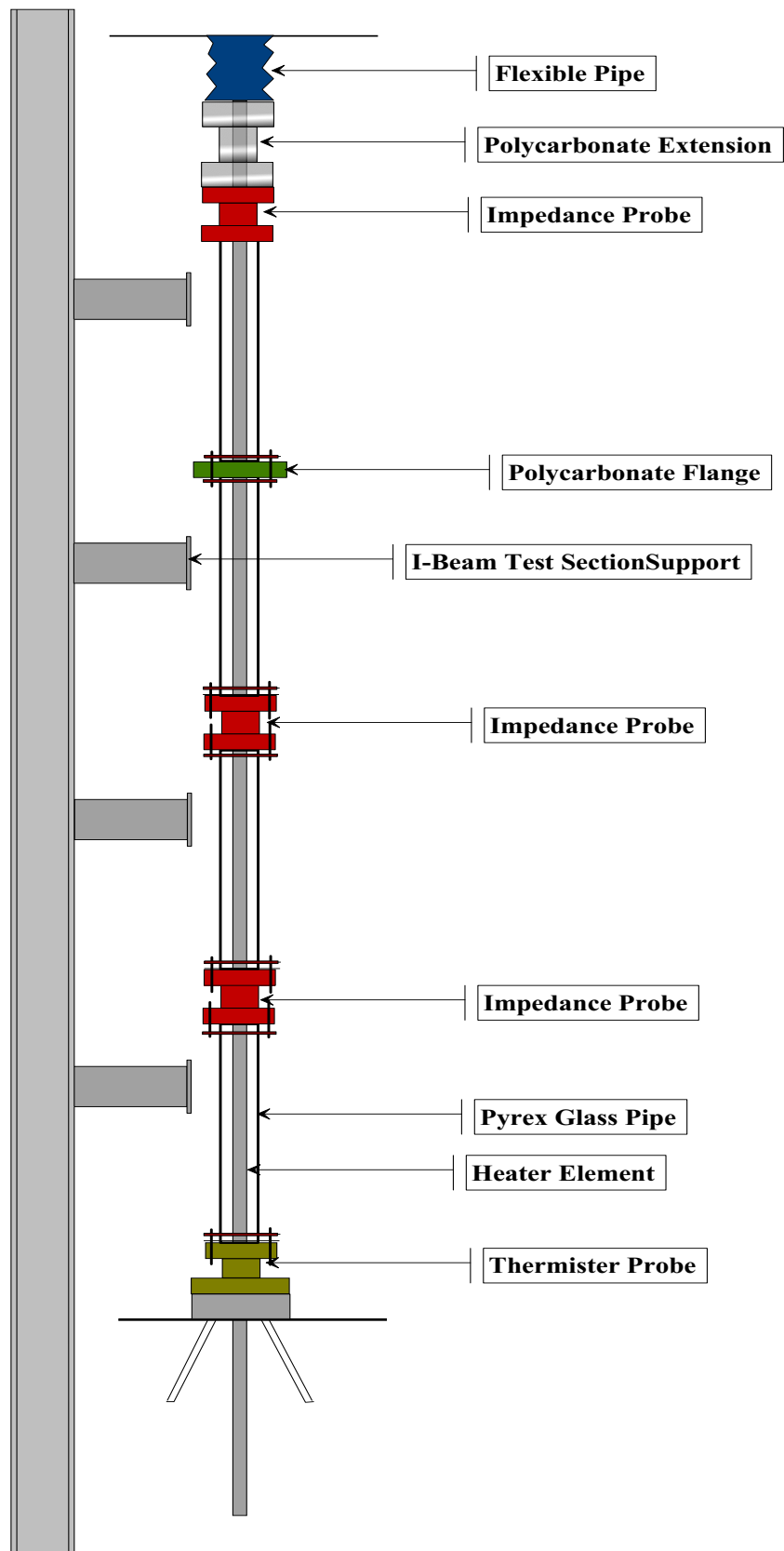


Figure 8.2. Test Section Layout

pipes is 60 psig (4.2 kg/cm^2). The pipes have deformation temperature of 525°C , and up to that point, they retain their mechanical strength. Furthermore, the glass pipe has good properties related to permissible thermal shock. Maximum permissible thermal shock is given as 120°K , which is high enough for the instability tests where oscillatory temperatures occur inside the test section. Two holes are built on the bottom and top polycarbonate flanges. One hole is for a pressure tap and the other one is for thermocouple. Differential pressure(DP) transducer lines are connected to a Honeywell ST3000 smart pressure cell to measure pressure differential across the test section. A pressure cell is connected to the inlet DP line to measure absolute pressure at the inlet of the test section. The K-type thermocouples are installed at test section inlet and outlet.

Test section is supported by five supports made of 1014 aluminum, which are mounted on a single I-beam, for aligning. The supports are spring loaded to absorb possible vibrations on the test section.

Test section heater (main heater) is a cartridge type heater, which is custom made by Watlow Corporation. The overall length of the heater is 3.81 m and has a 19.1 mm O.D. The heated section of the heater rod is 287 cm and begins 64 cm from the bottom of the heater. The maximum power of the heater is 40 kW and provides a maximum heat flux 233 kW/m^2 . It is powered with a three phase 480 VAC source. K-type thermocouple is inserted inside the heater at the location of 210 cm high from bottom. The rod is movable and can be traversed with a milling table. The heater rod must be supported to prevent it from bending. Each impedance probe provides two four-point support at its end flanges. Three sets of the support are used to support the heater rod. For each support, a hole is drilled and tapped; a 6-24 316 stainless steel screw is used. The screw end that is in the flow field are machined off and become a rounded tip. Although these supports interfere with the flow field, it is a necessary trade-off for accurate positioning of the heater.

The top of the test section is connected to an expansion joint. The expansion joint is necessary to accommodate the thermal expansion of the glass test section.

Between the expansion joint and test section upper flange, there is another heater rod support for centering.

Two OMEGA SCR73 series zero angle fired controllers are used to control the power of the main heater and preheater. SCR is acronym for Silicon Controlled Rectifier. The controller accepts a 4-20 mA input from a process controller. The SCR uses zero voltage-switching that controls the load by controlling the number of completed sine waves. Because only whole sine waves are used and the power is switched when the sine wave crosses the zero, there exists no radio frequency interference. The minimum power is 0.8% and the maximum power is 100%. The SCR has a variable time base from 0.2 to 2 sec. The SCR of the heater is sized to allow a maximum current draw of 75 amps for a 3 phase, 480 VAC potential. Similarly, the SCR of the preheater is sized to allow a maximum current draw of 30 amps for a 3 phase, 480 VAC potential.

The SCRs are controlled with either the PC based data acquisition system or an OMEGA CN7600 PID process controller. By using the former feature, nuclear coupling due to void reactivity feedback can be simulated based on void-meter signals. The OMEGA process controller uses a PID scheme to control the feedback temperature. This feature is not used for the heater because constant heat flux is needed during the experiments. This controller is used to prevent heater from burnout by allowing a set point for a maximum temperature and a maximum temperature rate change. The controller gives a 4-20 mA output that is interfaced to an SCR power controller.

8.3 Experimental Loop Instrumentation

This section describes the instrumentation developed for and used in the experimental loop. The instrumentation consists of impedance void-meters, a thermistor, thermocouples, magnetic flow meters, differential and absolute pressure transducers.

8.3.1 Impedance Void Meter

Knowledge of instantaneous void fraction in two-phase flow is important for both theoretical and experimental aspects of the thermal hydraulic instability studies. Void propagation velocity, which is the key for density wave oscillations, can be calculated based on void fraction measurement through the flow channel.

Many methods have been applied for void fraction measurement [51]. For instance, Revankar and Ishii [52] and Miller and Mitchie [53]. For the area averaged void fraction measurement, attenuation techniques were used by Chan and Bannerjee [54] and Eberle et.al. [55], whereas for the volume-averaged void fraction measurement, the traditional "Quick Valve Closure" method was used by Oliver and Hoon [56]. Among these techniques, the one based on the impedance measurement is the most suitable for thermal hydraulic instability experiments due to its fast response and direct knowledge of instantaneous area-averaged void fraction.

The impedance technique can provide the information about void fraction by measuring the electrical impedance of two-phase flow, and applying the relationship between the void fraction and the impedance. The fast response of impedance void-meters makes it possible to use them for measurement during transient situation as well as steady-state conditions. Impedance void-meters have attractive economic features as well, since it is much easier to construct them than other void measurement instruments.

8.3.1.1 Impedance Probe Design

The impedance void-meter consists of two major components: a probe and an electronic circuit. The design of the impedance probe is based on the requirement of withstanding the higher temperature up to 120°C. For good mechanical and non-corrosive properties, stainless steel is chosen as the material for the electrodes. Polycarbonate is used as an electrical insulator between electrodes, and the liner of the probe. The structure of the probe is shown in figure 8.3. Two rings are flush mounted on the inside wall and insulated from each other. The internal diameter is same as the inner diameter of the test section. The height of the electrodes is 12.7

mm and the distance between electrodes is 50.8 mm. A series of O-Rings are installed in gaps between electrodes and insulator material.

The impedance circuit consists of several parts including a buffer, a current-voltage amplifier, a rectifier, a low-pass filter and a voltage amplifier. An alternating current is supplied at 100 kHz to the electrodes on the impedance probe in order to avoid the double-layer effect. The circuit is versatile such that it can be adapted for void fraction measurement of multiphase flow with liquids of different electrical conductivities and different probe sizes by adjusting the gain of amplifiers of the circuit.

In impedance-based void measurements, some errors might be introduced. These errors can be avoided or reduced as discussed below;

1. Effect of Liquid Electrical Conductivity: The conductivity of water varies with temperature. This effect increases the difficulty of void fraction measurements. In order to account for the temperature effect on liquid conductivity, the relationship between temperature and liquid conductivity is measured over temperature range of interest. Based on this relationship, the measured impedance can be converted into dimensionless form at reference temperature.

Conductive chemicals are added to water to increase its conductivity. The chemicals are Morpholine and Ammonia Hydroxide. The water conductivity is kept around 300-400 μSi . Small portion of these chemicals might vaporize during the experiments and could change water conductivity. However, it is difficult to trace the conductivity change during the experiments. It is assumed that the water conductivity is constant during the experiments. This assumption should be justified based on the experimental results.

2. Electronics Drift: The output of impedance measurement circuit is proportional to the amplitude of the carrier signal from the function generator, values of the feedback resistors of voltage amplifier, and conductance of the two-phase mixture. Therefore, the drift of the amplitude of the carrier signal and values

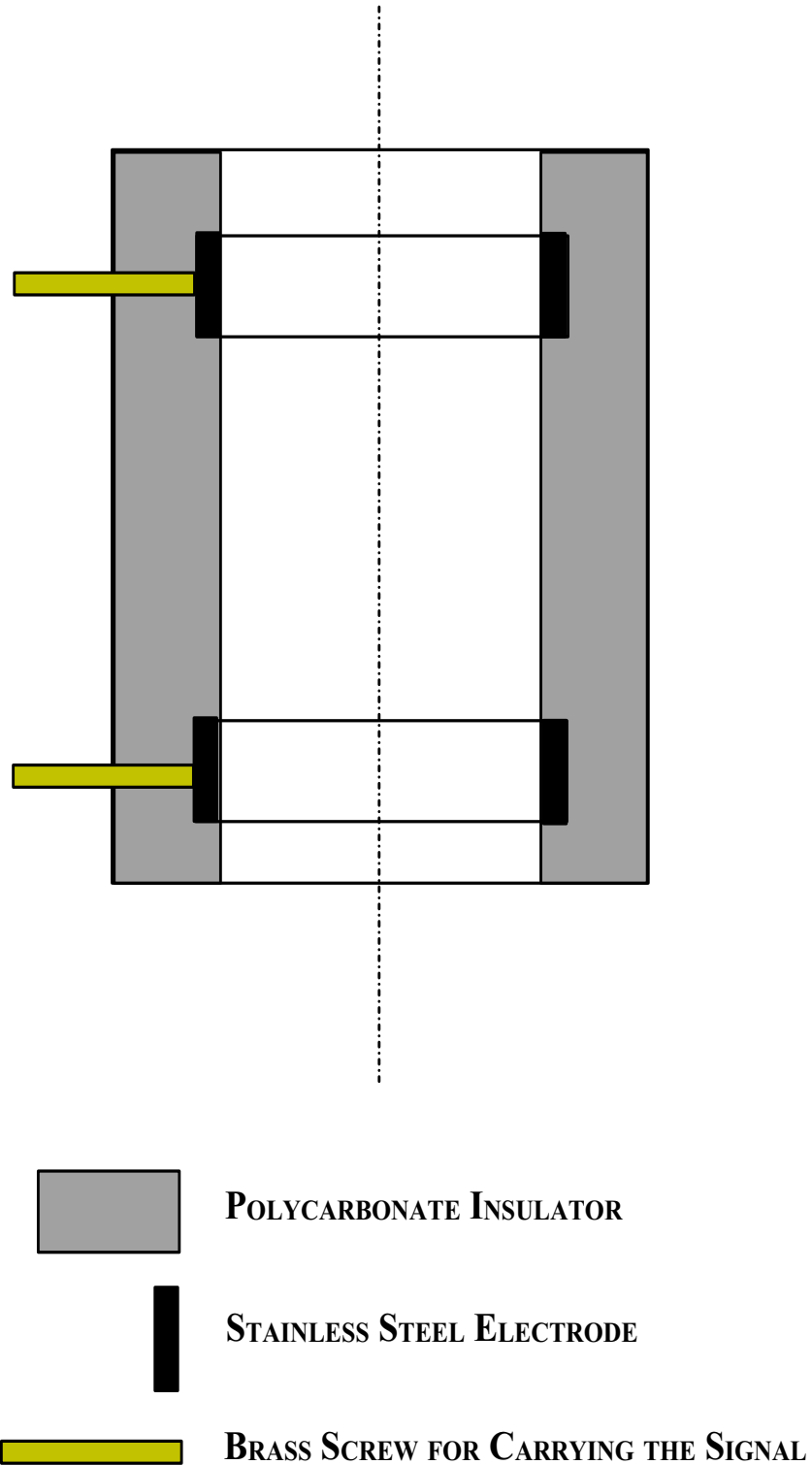


Figure 8.3. Impedance Probe with Ring Type Electrodes

of feedback resistors should be minimized. Feedback resistors with 0.1% temperature coefficient are used. Normally tests are conducted after keeping the instruments on for more than one hour to stabilize the circuit as well as the function generator.

3. Mechanical Installation Error: It should be noted that mechanical errors could be introduced if the impedance probes were not installed with proper alignment. In order to reduce mechanical errors, the impedance probes are installed with extreme care and properly aligned with the test section.

8.3.1.2 Theoretical Basis

During the experiments, the water acts as conductive liquid, and conductance measurements are performed. Normally, conductance of a two-phase mixture depends on conductivity of the phases and their distribution. If conductivity can be assumed constant, the relationship between impedance and void fraction can be predicted for some ideal distributions such as uniform dispersed flow and concentric separated flow.

The dimensionless impedance of a two-phase mixture, G^* , is defined as

$$G^* = \frac{G_f - G_m}{G_f - G_g} \quad (8.1)$$

where G_m is the measured impedance value between two electrodes, G_g is impedance value when the probe section is full of non-conductive gas (vapor) and G_f is impedance measured when probe section is full with conductive liquid.

For dispersed flow, especially bubbly flow, the electrical field between two electrodes is uniformly distributed in the mixture. Hence the impedance of the mixture depends only on the conductivity of the mixture. In such a case, the dimensionless impedance of the two-phase mixture, G^* , can be predicted by Maxwell's relation [57].

$$G^* = \frac{3\alpha}{2 + \alpha} \quad (8.2)$$

Maxwell's relation is based on the assumption that the non-conductive dispersed

phase is composed of non-interacting and equal-size spheres, and distributed uniformly in the continuous phase liquid, which is consistent with the characteristics of bubbly flow when the void fraction is low (less than 30%).

For annular flow, void fraction measurement is no more than a film thickness measurement, if the droplets entrained into the gas phase is neglected. In this case, ring-type electrodes of the impedance probe exhibit more advantages than other type of electrodes. Theoretical analysis of the behavior of a probe with parallel rectangular electrodes separated by a short distance was developed by Coney [58]. Coney computed the impedance between two rectangular electrodes by the conformal transformation and obtained

$$G_m = \sigma_o L_e \frac{K(m)}{K(1-m)} \quad (8.3)$$

where $K(m) = \int_0^{\pi/2} (1 - m \sin^2(x))^{-1/2} dx$ is the complete elliptic integral of the first kind, L_e is the effective length of electrodes, and

$$m = \frac{\sinh^2 \left(\frac{\pi W}{2\delta_e} \right)}{\sinh^2 \left(\frac{\pi(W+D)}{2\delta_e} \right)} \quad (8.4)$$

where W is the width of the electrodes, D is the distance between electrodes, and δ_e is the (equivalent) liquid film thickness.

Andreussi et al. [59] extended the above analysis to the impedance probes with ring-type electrodes by introducing an equivalent thickness,

$$\delta_e = \frac{A_f}{\xi_w} \quad (8.5)$$

where ξ_w is the wetted perimeter, A_f is the flow area. For annular flow, the equivalent thickness is

$$\delta_e = D \frac{1-\alpha}{4} \quad (8.6)$$

If it can be assumed that the liquid film attached on an electrode has the same potential as the electrode's, the dimensionless impedance of the two-phase mixture

can be approximately expressed as

$$G^* = \alpha \quad (8.7)$$

This implies that, for very thin liquid film, the dimensionless impedance measured by the impedance void-meter can be related linearly to void fraction.

8.3.2 Thermistor Probe

The inlet temperature is one of the key parameters in instability experiments. In order to improve the measurement accuracy, a thermistor probe (OMEGA 0N-403-PP) is installed just above the inlet flange of the test section. The thermistor probe has interchangeable sensor and its accuracy is around $\pm 0.1^\circ\text{C}$. During an experiment, measured inlet temperature can be obtained from a handheld thermistor thermometer (OMEGA HH42) that is connected to the thermistor probe. The measurement range for the thermistor thermometer is from -20°C to $+130^\circ\text{C}$, and its resolution is 0.01°C from -20 to 102°C .

The stainless steel probe is 3.2mm in diameter, and 114mm in length. The section of the probe immersed in the flow is required to be at least twenty times longer than the probe diameter, which is 6.4 mm. The flow channel of the test section is only 19.05 mm in width. Thus, the probe is bent 90° and the immersed length is 76.2 mm as seen in figure 8.4.

8.3.3 Magnetic Flowmeter

HONEYWELL MagneW 300 PLUS magnetic flow meters are setup to measure volumetric flow rate in the test section and the bypass section. The flow-meter that measures the main flow through the test section is placed at the preheater outlet. The other flow meter, which is for bypass flow, is located on the middle of the bypass flow.

Each magnetic flow meter consists of a detector and a converter combination, which operates on the principles of Faraday's Law. The detector receives its power from the converter in the form of DC square waves to the detector's excitation coils.

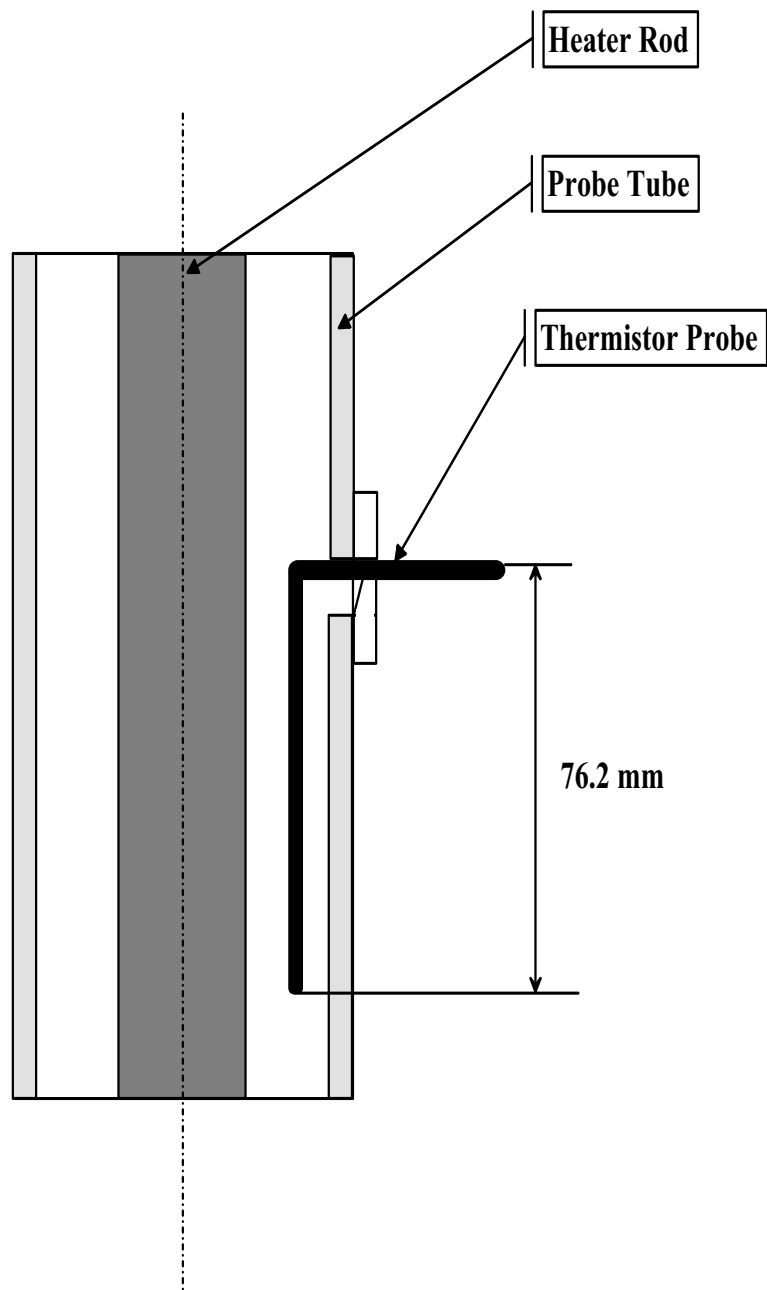


Figure 8.4. Thermistor Probe

These coils create a magnetic field at a right angle with respect to the flow direction. As the conductive liquid flows through this magnetic field, a voltage is produced across the electrodes, which is proportional to liquid flow velocity. The detector send this voltage signal to the converter. The converter, which holds the circuitry that calculates and displays the flow data, converts the detector signal into standard 4-20 mA output for recording and controlling instrumentation.

8.3.4 Differential Pressure Transducer

The measurement of pressure drop across the test section and various parts of the experimental loop is necessary to quantify the thermal-hydraulic instabilities. For the purpose, three differential pressure transducers (DP) have been installed. Two of them are HONEYWELL STD130 type, while the other is HONEYWELL STD120 type. The measurement is done by a piezoresistive sensor, which actually contains three sensors in one. It contains a differential pressure sensor, a temperature sensor, and a static pressure sensor. Micro-processor-based electronics provide higher span-turn-down ratio, improved temperature and pressure compensation, and improved accuracy. The type STD130 has differential pressure range between 0 to 7 bar. The other type STD120 has measuring range between 0 to 1 bar. The locations where differential pressures are measured;

1. Pressure drop across the test section
2. Pump outlet to test section outlet
3. Test section inlet to top of the experimental loop

The exit and inlet losses can be calculated by comparing the measurements from DP cells.

8.3.5 Absolute Pressure Transducer

One of the important parameters in the instability experiments is the inlet sub-cooling ($\Delta T = T_{sat} - T_{in}$), which is used to compute the subcooling number. Along with the Zuber Number, subcooling number determines the stability of the system

for given other dimensionless numbers. Therefore, determination of inlet subcooling via measuring inlet temperature and inlet absolute pressure is highly important.

For the purpose, HONEYWELL ST 3000 Smart Transmitter Series 100e Absolute Pressure Transmitter Type STD140 is used. The working principle is the same as the working principle of the differential pressure transducer. The range for the equipment is between 0 and 500 psia.

8.3.6 Thermocouples

In addition to the thermistor at the test section inlet, there are several points at which temperature is measured with OMEGA K-type thermocouples of model number KMQSS-062G-6. Temperature is measured at test section inlet, test section exit, top of the loop, pump inlet, pump outlet (preheater inlet) and preheater outlet. Temperature measurement at test section inlet and exit are fed to the PC-based data acquisition system. For the inlet temperature measurement, reading from thermistor probe are used to quantify the inlet subcooling because of its higher accuracy.

8.4 Data Acquisition System

Data is acquired from the instruments using a personal computer and a data acquisition system. The computer is a DELL Dimension XPS T800r with 800 MHz CPU. It has a hard drive with 10 GB capacity for data storage. A CD burner and an IOMEGA ZIP drive are installed to archive the raw data.

The data acquisition board is a National Instruments AT-MIO-64E3. The board has a maximum acquisition rate of 500,000 samples per second for a single channel and 12-bit resolution. The board is configured for 64 single-ended or 32 differential analog inputs. The board input range is software selectable. The internal DAS board is connected to a SC-2056 adapter. Most signal-carrying wires are connected to this adapter.

A 5B01 backplane is attached to the SC-2056 adapter. On this signal conditioning backplane, two 5B37 Thermocouple Input Modules and two 5B39 Current Output Modules are installed. The 5B37 Thermocouple Input Modules have input

span limits of ± 10 mV to ± 0.5 V and ab output range of 0 to +5 V. The accuracy and nonlinearity of these input modules are $\pm 0.05\%$ of span and \pm of span, respectively. The 5B39-01 Current Output Modules are used to control the heater and the pre-heater power. These output modules accept a high level signal at its input from the AT-MIO-64E3 analog output and provide a galvanically isolated 4-20 mA process current output signal. The 5B39-01 Current Output Modules features high accuracy of $\pm 0.05\%$, $\pm 0.02\%$ of nonlinearity and 1500 Vrms common mode voltage isolation protection.

9. EXPERIMENTAL RESULTS

The experimental results for the flow excursion and the DWO are presented in this chapter. Air-water experiments are performed to calibrate the impedance void-meter against DP measurements. The characteristic of the flow instabilities observed in the experimental facility is clarified by the diabatic experiments performed at different operating points on the subcooling number and the zuber number plane.

9.1 Air-Water Tests

Series of air-water experiments are performed to cross-calibrate the impedance void-meter with the DP measurements. The dimensionless impedance which is given by

$$G^* = \frac{G_f - G_m}{G_f - G_g} \quad (9.1)$$

where G_f is the impedance measured when the probe is full with water, G_g is the impedance measured when the probe is full with air, and G_m is the impedance corresponding to the two-phase mixture. As can be seen from the Eq. (9.1), G^* is direct indication of the area-averaged void fraction. By increasing the air flow through the test section, different flow regimes can be observed. The impedance probes can also be used for the identification of the flow regimes, since probe signal carries the signature of different flow regimes. Figure 9.1 shows the typical signature of the bubbly, the cap-bubbly and the slug flow regimes observed in the test section.

The differential pressure transducer (DP-2) located to measure the pressure differential across the test section can also be used to measure the the volume-averaged void fraction. The void fraction can be computed from the DP measurement by

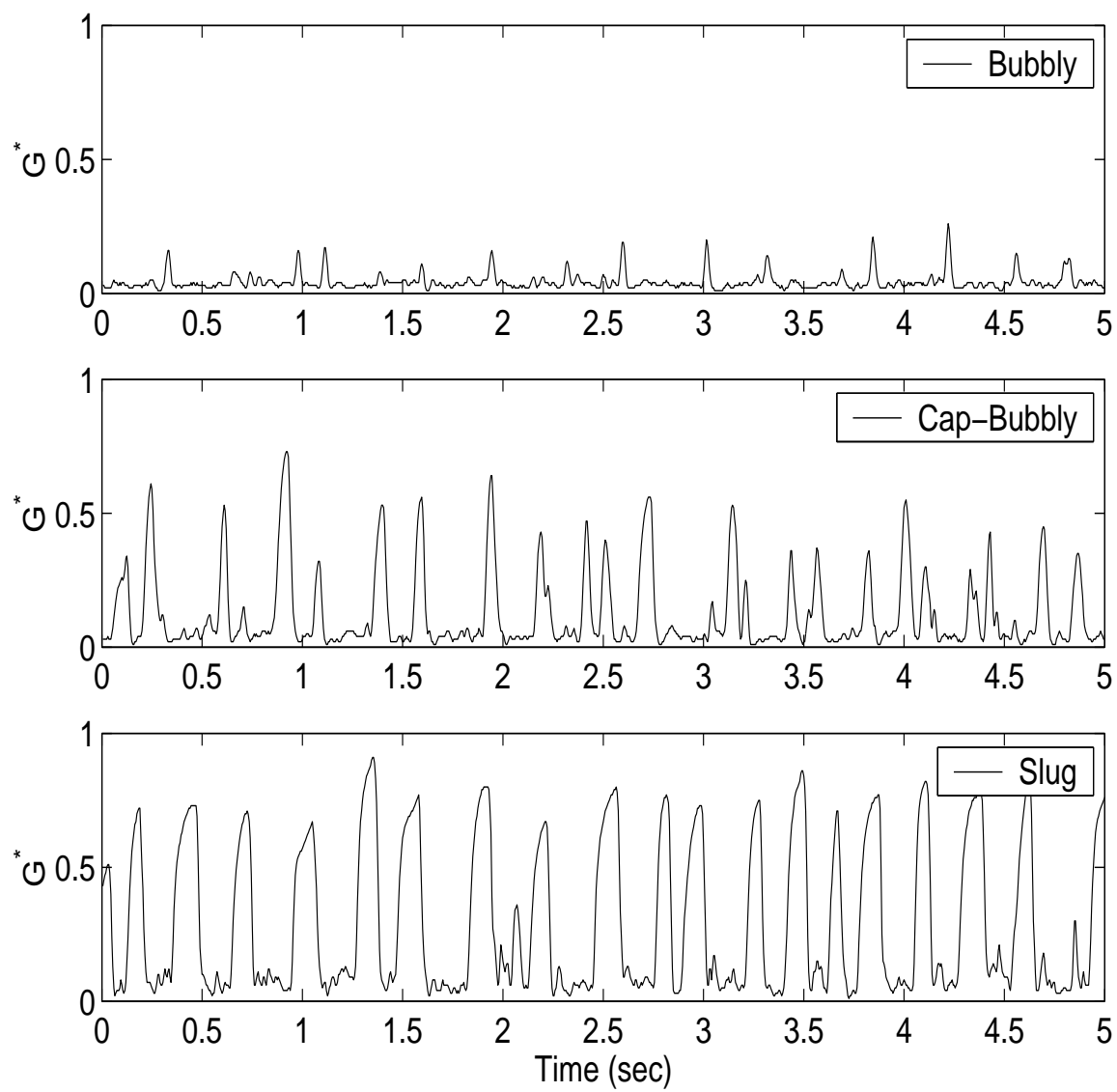


Figure 9.1. Typical Impedance Signal for Different Flow Regimes

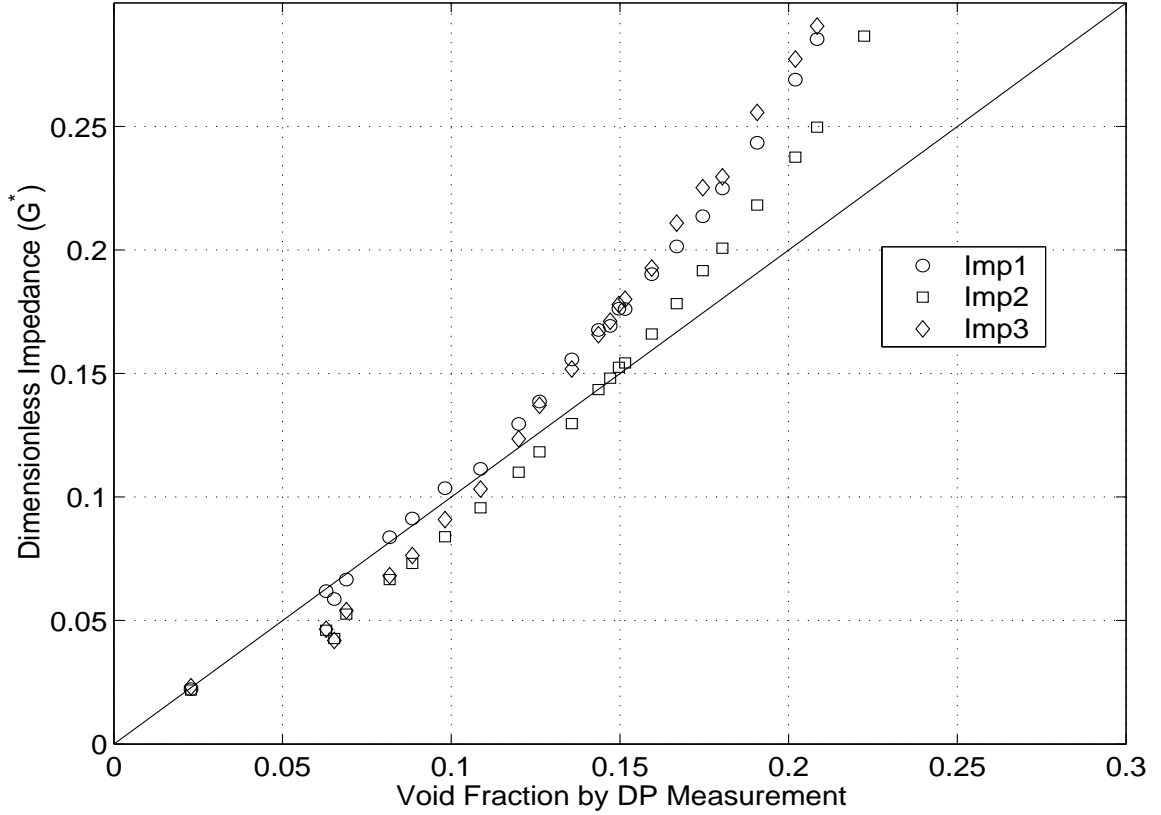


Figure 9.2. Cross-Calibration Curve for the Void Measurement with the DP Cell and the Impedance Probe

assuming the gravitational pressure drop is the dominant pressure drop component;

$$\alpha = \frac{\Delta P_{test}}{\rho_f g l_{test}} \quad (9.2)$$

where l_{test} is the distance between two pressure taps, ρ_f is the liquid density inside the DP line, and g is the gravitational acceleration. Figure 9.2 shows the cross-calibration curve between void fraction measured by DP cell and the dimensionless impedance for each of the impedance probe located along the test section. Imp1 denotes the impedance probe at the lowest location, Imp2 denotes impedance probe at the middle of the test section, and Imp3 denotes the probe at the top of the test section.

It can be seen from Figure 9.2 that the dimensionless impedance G^* gives similar void fraction compared to the one measured by the test section pressure drop up to % 15 of void fraction. However, beyond that point, the discrepancy between two measurement methods increases. The reason is that accelerational and frictional effects in the DP measurement increase with void fraction. This basically results in underestimation of the void fraction. In the analysis of the experimental results, the dimensionless impedance is used as area-averaged void fraction measured at each axial location on the test section.

9.2 Flow Instability Tests

Series of experiments are performed for the different operational conditions in the test facility described in Chapter 8. The following measurements are taken for different tests conditions:

1. Impedance at Three Axial Locations (Imp1, Imp2, Imp3)
2. Absolute Pressure at the Test Section Inlet (Pcell)
3. Differential Pressure across Different Section of the Facility (DP-1, DP-2, DP-3)
4. Volumetric Flow in the Test Section and the Bypass Section (Mag-1, Mag-2)
5. Test Section Inlet and Exit Temperature (Tinlet, Texit)
6. Test Section Heater (MHeater)
7. Preheater (Heater)

The name inside the parenthesis denotes the name tag assigned for each of the instrument.

9.2.1 Experimental Procedure

An experimental procure guide is prepared for the general guideline to be followed during the experiment. Before starting the experiment, impedance circuit and DC power supply are turned on one-hour prior taking data. This is necessary to

Test No:	T_{in} ($^{\circ}\text{C}$)	v_i (m/s)	Q (kW)	N_{sub}	N_{Zu}
1	93	1.2	40	42.1	18.9
2	82	0.8	35	62.1	28.2
3	85.5	0.85	35	54.8	26.5
4	88	0.95	35	49.6	23.3
5	89	0.97	35	48.3	22.4
6	81	0.65	30	64.6	30.7
7	84.5	0.7	30	57	27.5
8	88	0.85	30	50.6	22.1
9	91.5	1.05	30	43.5	17.9

Table 9.1. Test Conditions for the Flow Excursion

overcome the effect of electronic drift exists in the circuitry. Bypass flow is adjusted by using the valve located on the bypass channel to control the fraction of bypass flow in the test facility. The bypass flow is kept much larger (3 times) than the test section flow in order to ensure that most of the flow goes through the bypass section to maintain constant pressure drop boundary condition across the test section. Preheater is used to initial heat-up of the facility from the cold conditions. After reaching the predetermined test section inlet temperature, the test section power is gradually increased. At the same time, the cooling flow rate is adjusted to keep the inlet temperature constant. For given test section power, inlet velocity and inlet temperature, steady-state conditions are maintained. From the analytical study given in Chapter 6 , it has been shown that decrease in the channel inlet velocity is always stabilizing as can be seen from the maps generated on the subcooling number and the zuber number. Therefore, one way to destabilize the system is to gradually decrease the flow velocity via adjusting the pump rotation frequency. Before decreasing the velocity at fixed heater power and inlet temperature, data acquisition system is triggered to take the data for five minuted. The data acquisition frequency is set to 200 Hz.

Table 9.1 summarizes the flow conditions where the flow excursion is observed. The data is plotted on subcooling number and zuber number plane with analytical model prediction for the stability boundary. Figure 9.3 shows the comparison

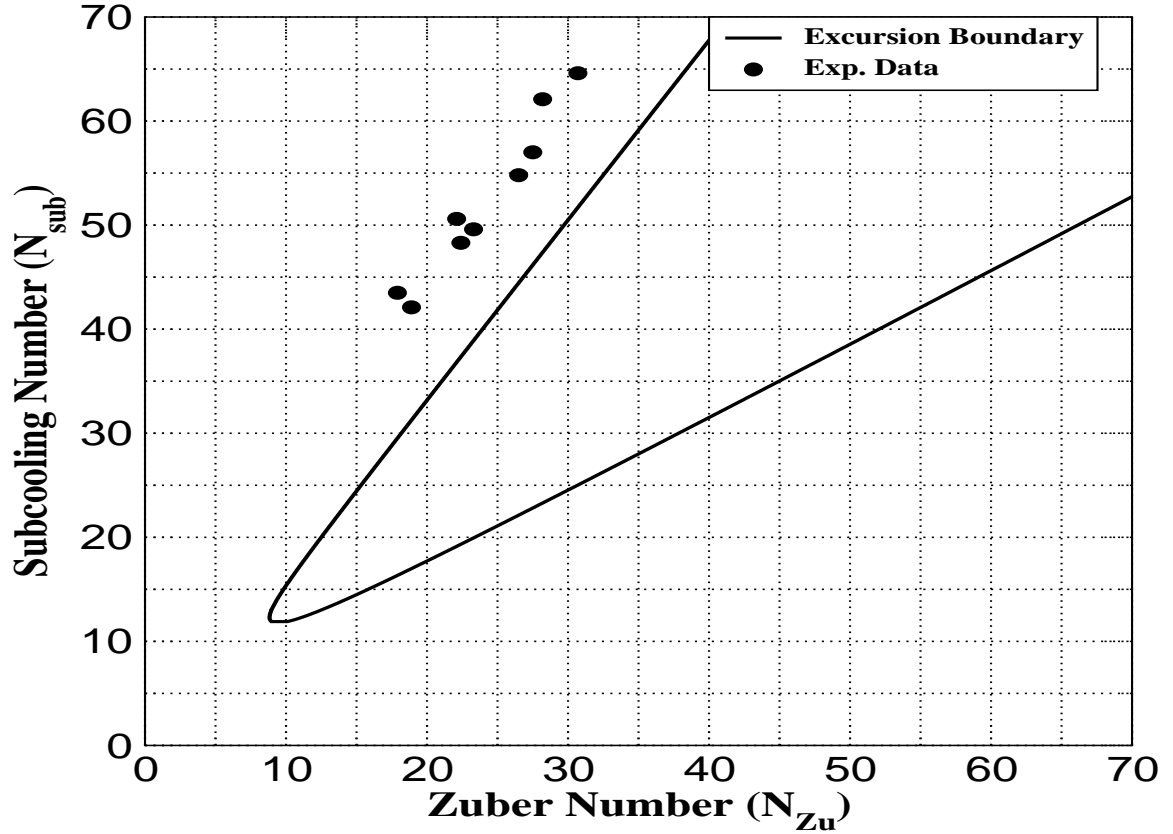


Figure 9.3. Comparison of the Experimental Data and the Model Prediction

between the data and the prediction obtained by solving the dimensionless characteristic equation for the flow excursion. The experimental data also shows that subcooled boiling is major destabilizing effect in two-phase flows as predicted by the analytical model. Therefore, neglecting subcooled boiling non-conservative results in terms of the flow excursion boundary. The discrepancy between the data and the model can be explained as follows;

- i. The characteristic equation derived for the flow excursion in Chapter 6 describes the problem as finding the solution where $\frac{\partial \Delta P}{\partial v_i} = 0$. This equation gives a region inside which pressure drop vs. flow rate curve has negative slope with two lines. Therefore, the first boundary represents the conditions where $\frac{\partial \Delta P}{\partial v_i} = 0$. This point can be crossed by changing the heat flux which moves the curve up and

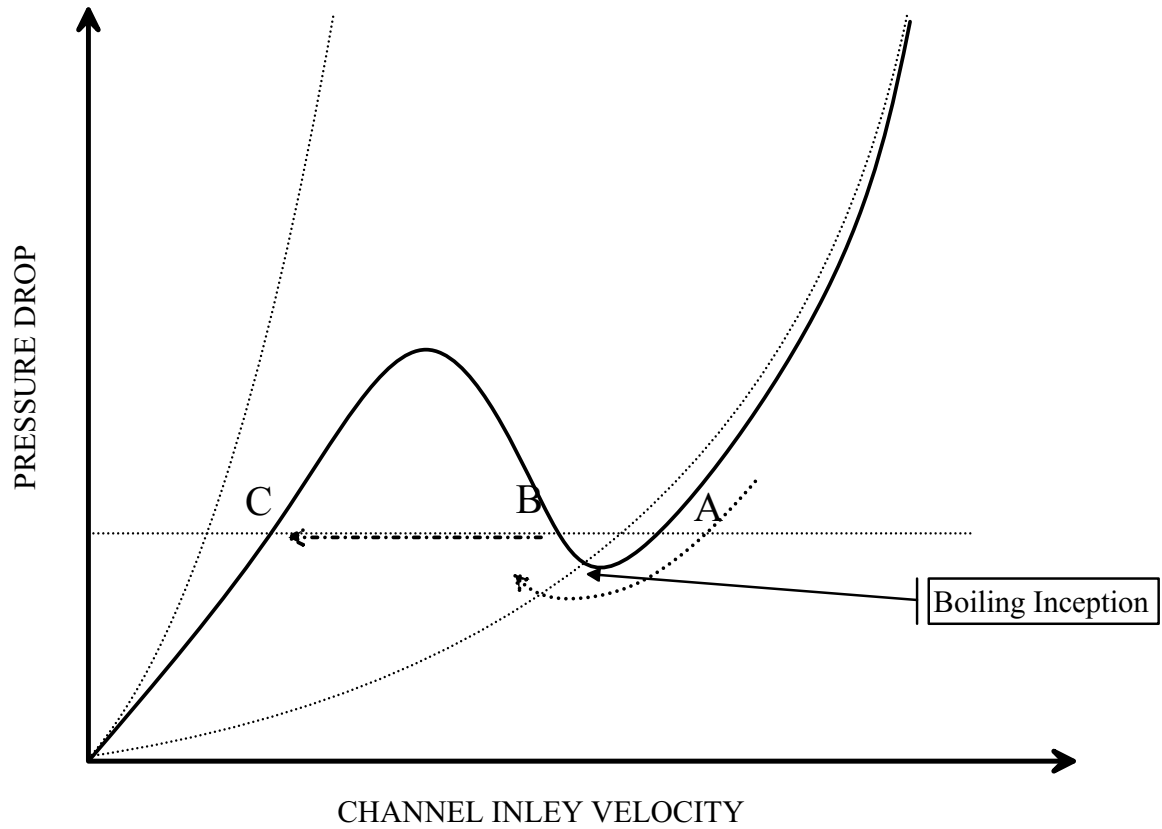


Figure 9.4. Transient Path during the Flow Excursion observed during the Tests

down. However, the channel inlet velocity is decreased gradually until it reaches the flow excursion conditions in the experiments. As referring to Figure 9.4, the flow excursion occurs at point B where the velocity is smaller than the velocity at point A which is predicted by the model. Therefore, the experimental conditions at which the excursion begins correspond to the higher zuber number.

- ii. The other factor that may cause the discrepancy is the validity of the subcooled boiling at low pressure conditions. The experiments performed for subcooled boiling at low pressures indicate that the Saha-Zuber model underestimates the

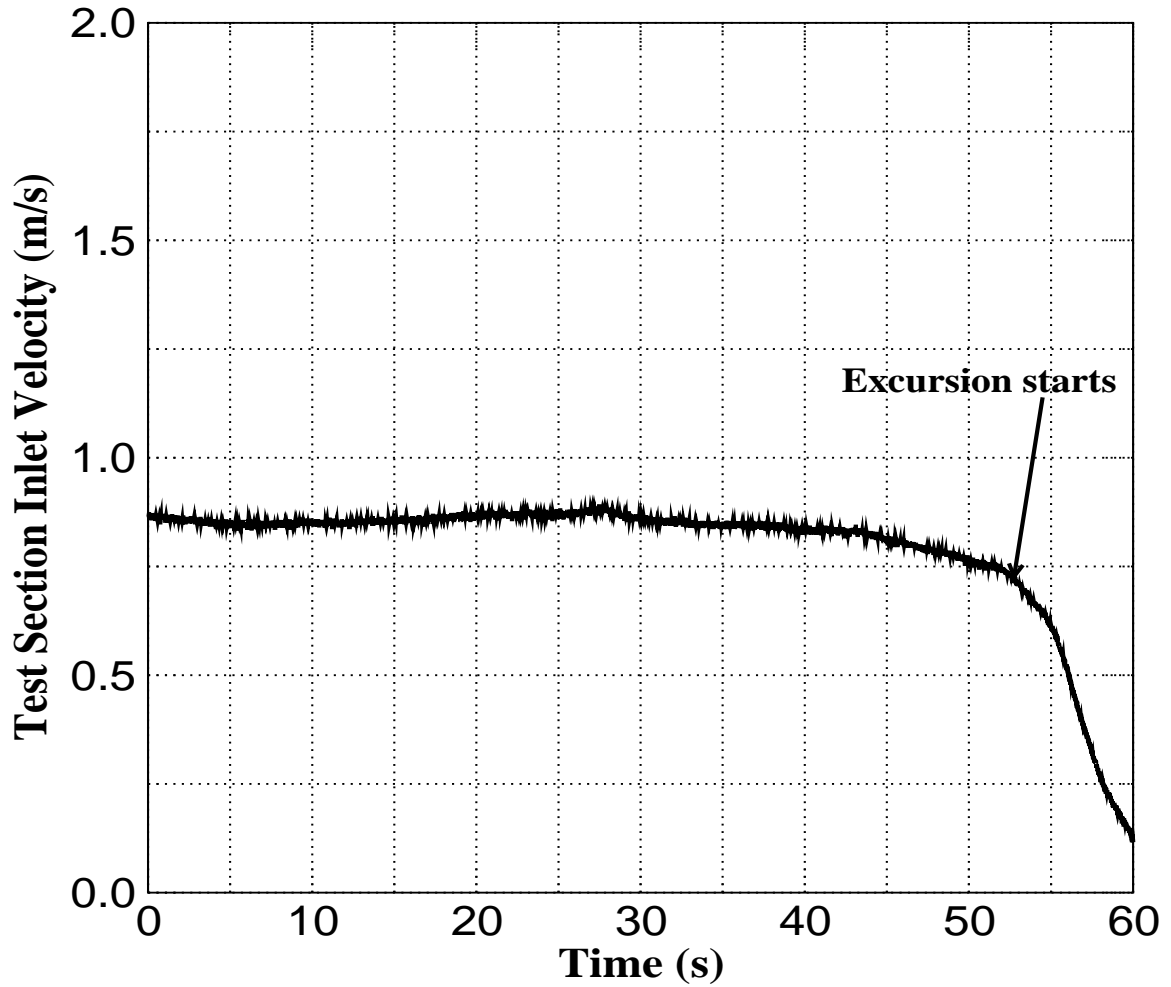


Figure 9.5. Transient in the Channel Inlet Velocity during the Flow Excursion

departure enthalpy at low pressures. In other words, the void-departure starts at lower value of liquid enthalpy than the one predicted by the Saha-Zuber model.

Figure 9.5 shows the typical flow transient during the flow excursion (test no:2). Once the flow excursion boundary reached, there is rapid decrease in the flow. This is the reason that the velocity which is shown with an arrow in the figure is statically unstable. Small decrease in the flow further decelerates the flow until it reaches another stable steady-state solution which corresponds to the high quality two-phase region (point C in Figure 9.4.

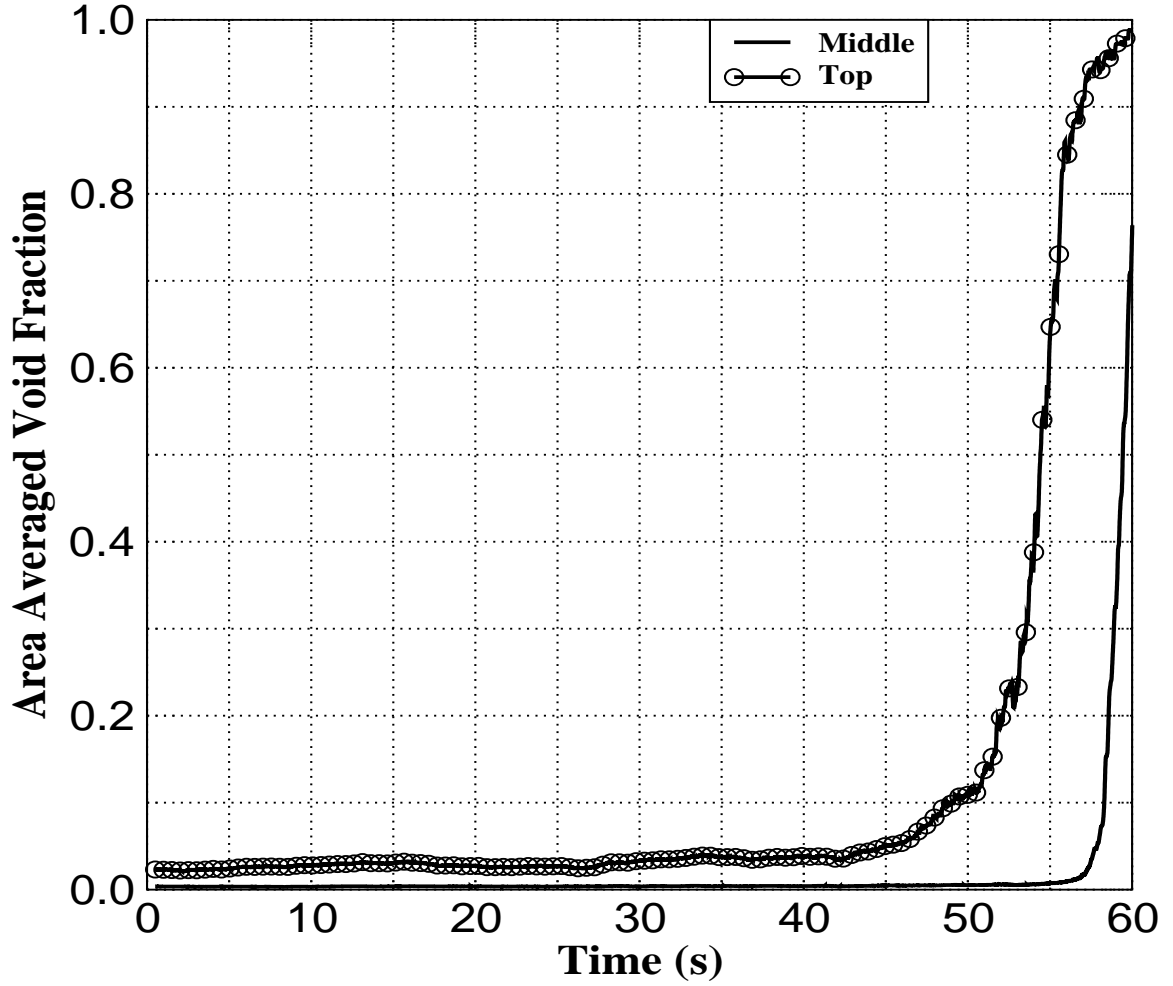


Figure 9.6. Transient in the Channel Void Fraction during the Flow Excursion

Figure 9.6 demonstrates how the void fraction in the channel increases in the channel following the flow excursion. The data shown in the figure corresponds to the dimensionless impedance which can be interpreted as void fraction. Following the excursion, the channel rapidly becomes vapor. In the tests, tests have been terminated at this point. Since high quality conditions may easily reaches the CHF conditions. The flow excursion induced CHF is very important CHF mechanism under natural circulation conditions at low-pressures [7].

However, the flow excursion does not need to yield stable solution at high quality two-phase flow. Especially, at low subcooling, the oscillatory flow might occur due

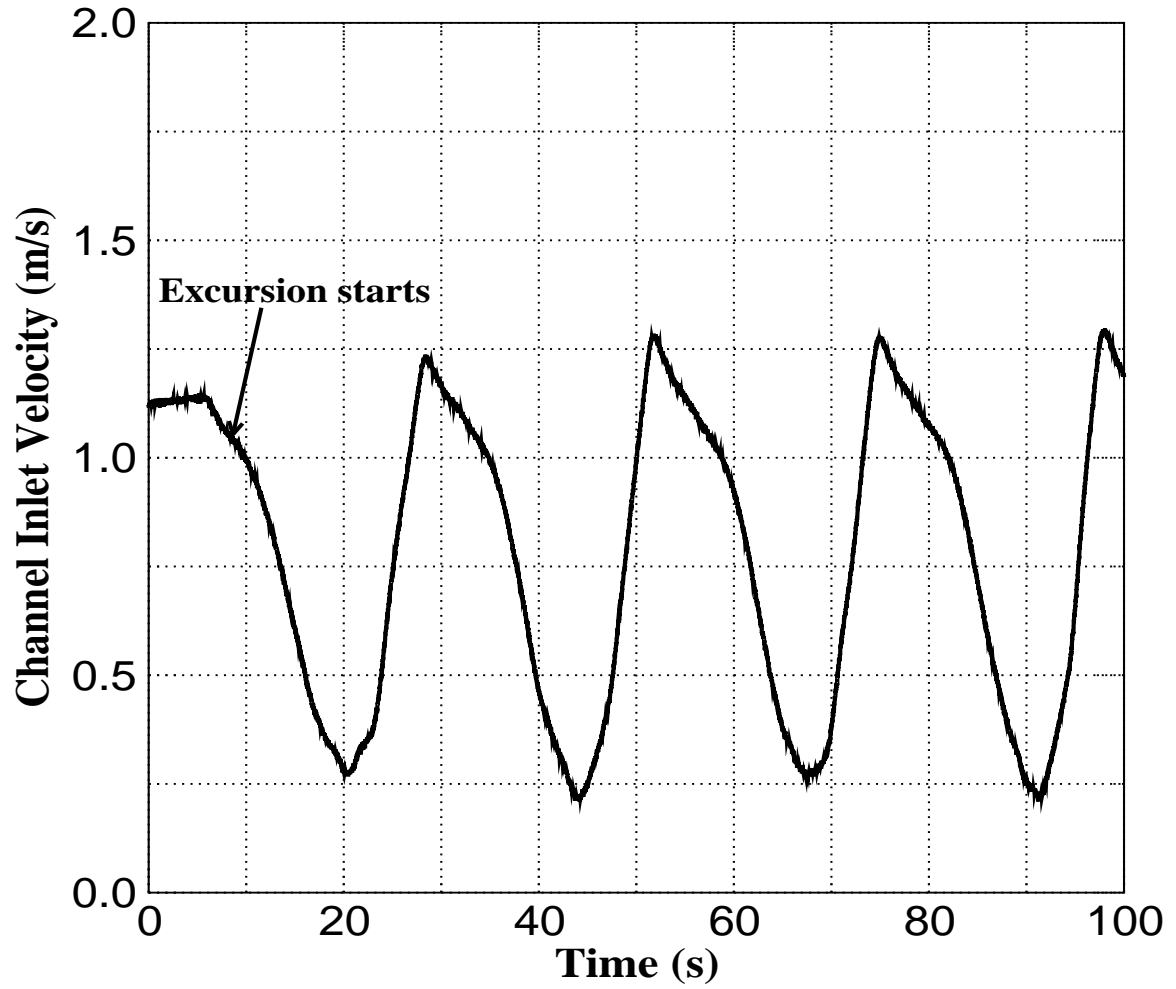


Figure 9.7. Constant Amplitude Oscillations following the Flow Excursion

to interaction between the flow excursion and DWO. For instance, at test no:9, the oscillatory flow occurs in the channel following the flow excursion. Figure 9.7 shows the constant amplitude oscillations following the flow excursion. In this case, CHF is not as certain as in the case shown in Figure 9.5.

Test No:	T_{in} ($^{\circ}\text{C}$)	Q (kW)
10	95	30
11	95	25
12	94.5	27.5
13	96	32.5
14	98	20
15	99	20
16	100	30
17	100	32.5
18	100	35
19	99.5	37.5
20	100	40

Table 9.2. Test Conditions for Flow Oscillations at High Inlet Temperature

Experimental observations demonstrated that the pure flow excursion occurs when the inlet subcooling is high. Series of experiments have been performed at relatively high inlet temperatures where large amplitude, low frequency oscillations are observed. Table 9.2 summarizes the tests conditions in terms of the inlet temperature, and the main heater power.

Figure 9.8 shows the oscillations observed at test no:14. It clearly shows that the channel inlet velocity has phase-shift around 180° respect to the channel exit void fraction. The phase-shift is an indication of the void propagation through the channel. In other words, any disturbance occurs at the channel inlet propagates with the kinematic wave velocity which is close to the vapor velocity and induces disturbance in the two-phase mixture region. Since this process is associated with certain time-lag due to the void-wave propagation, phase-shift occurs between the inlet velocity and the exit void fraction (or two-phase pressure drop). As explained in Chapter 2, when the phase-shift becomes 180° , self-sustained flow oscillations are observed.

Figure 9.9 clearly shows that as the heater power is increased, the oscillations' amplitude becomes larger. However, oscillation frequency is almost same for the test no: 16, 17, 18 and 20.

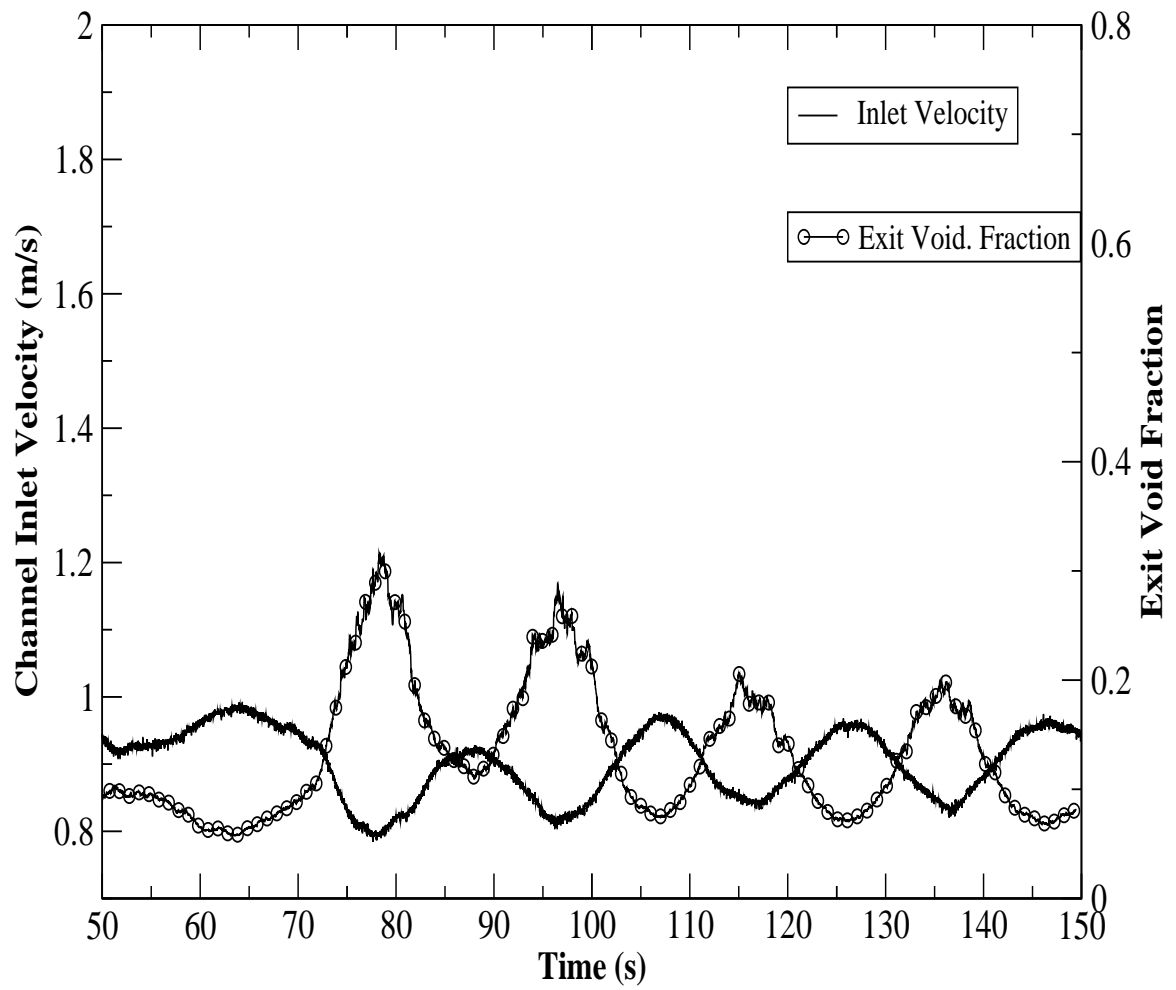


Figure 9.8. Self-sustained Flow Oscillations at Test No:14

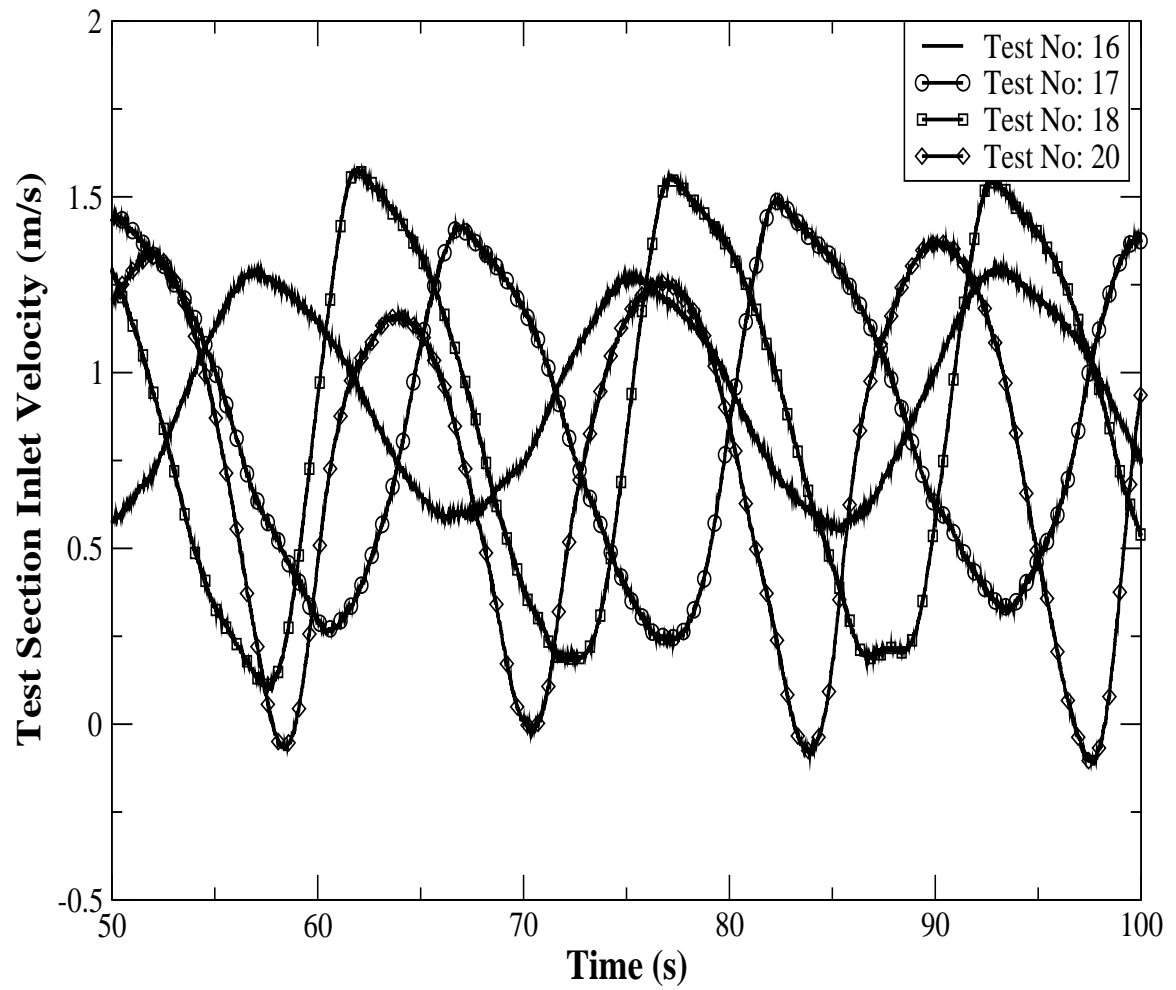


Figure 9.9. Change in the Oscillation Magnitude with the Heater Power

9.3 Void-Reactivity Feedback Simulation

The implementation of the void-reactivity feedback simulation via heater power control program written in LabView is described in this chapter. The simulation considers the time rate of change in the heater power predicted by the point kinetic model and the artificial time delay predicted by the single lumped model derived in Chapter 4. This insures that the actual heat flux to the coolant is well simulated in the electric heater rod such that the overall impact of the nuclear-coupled thermal-hydraulic instabilities can be accurately assessed experimentally.

Figure 9.10 demonstrates the data flow in the facility when simulating the nuclear-coupled instabilities. The instantaneous area-averaged void fraction is measured at three different axial locations along the test section. Along with the other instruments, the impedance circuit outputs are connected to SC-2056 adapter, which feeds the data into the data acquisition computer. The AI-MIO-64E3 DAQ card converts the analog input to the digital format that can be processed via the power control program written in LabView.

Point kinetic equations given by Eqs. (5.5a) and (5.5b) can be solved numerically by introducing the first order implicit Euler method. In this method, time derivatives are approximated as

$$\frac{dn}{dt} \approx \frac{n_{i+1} - n_i}{\Delta t}, \quad (9.3)$$

where Δt is the time step size and i is the time index starting from 0. Implicit methods are favorable since the method is always stable irrespective of the time-step size. However, if the time step size is too large, then the accuracy of the solution is reduced. By means of the implicit Euler method, explicit expressions for new time step values for the neutron amplitude and the precursor concentration can be determined as

$$n_{i+1} = \frac{\frac{\lambda}{\Lambda} \xi_i e^{-\lambda \Delta t} + n_i \left[\frac{1}{\Delta t} + \frac{\lambda \beta \Delta t}{2\Lambda} e^{-\lambda \Delta t} \right]}{\frac{1}{\Delta t} - \frac{\rho_i - \beta}{\Lambda} - \frac{\lambda \beta \Delta t}{2\Lambda}} \quad (9.4a)$$

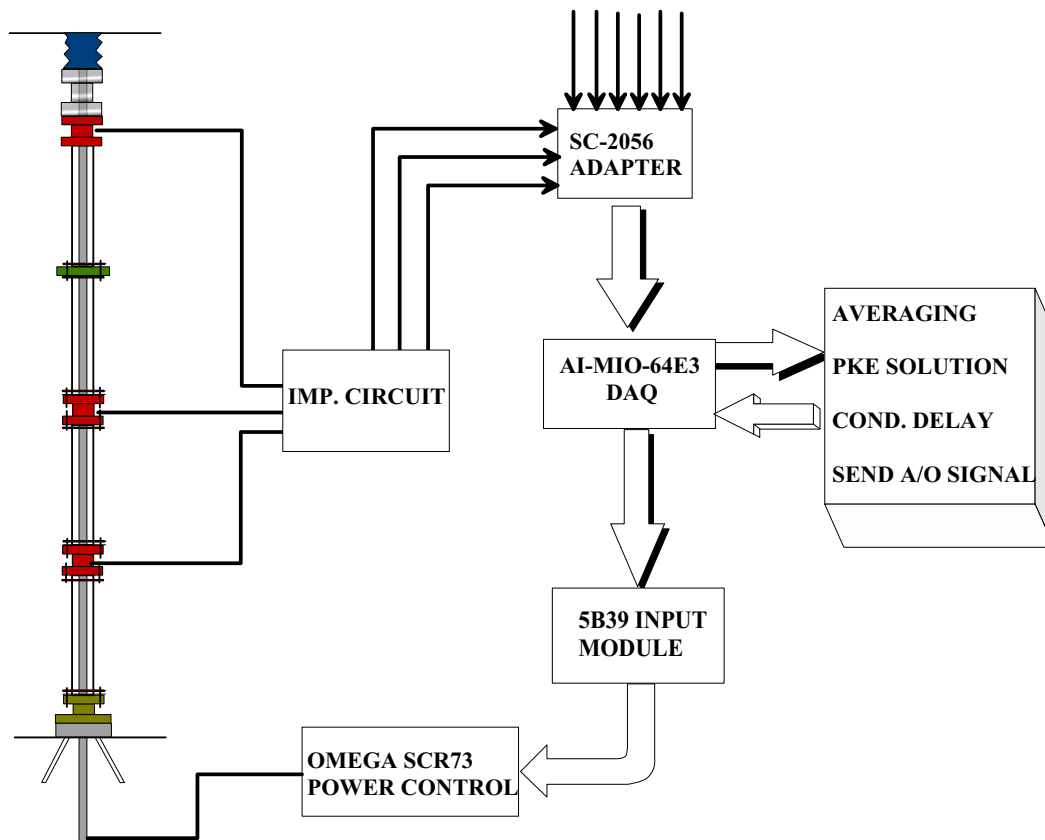


Figure 9.10. Data Flow for Void-reactivity Simulation Experiment

$$\xi_{i+1} = \xi_i e^{-\lambda \Delta t} + \frac{\beta \Delta t}{2} \left[n_{i+1} + n_i e^{-\lambda \Delta t} \right] \quad (9.4b)$$

The scheme is started with $n_0 = 1$ and $\xi_0 = \frac{\beta}{\lambda}$, then Eq. (9.4a) is solved first. With calculated n_{i+1} , Eq. (9.4b) is used to update the value for ξ_{i+1} . The current time is $t = i\Delta t$.

The void-reactivity feedback at time step i is written as follows:

$$\rho_i = \Delta \rho_\alpha(\langle \alpha \rangle_z(t_i), \langle \alpha_o \rangle_z) \quad (9.5)$$

where $\langle \alpha \rangle_z$ represents the axially averaged void fraction from the area- and time-averaged void fraction. The time averaging is performed via moving averaging to remove the high frequency noise in the void signal. The axial averaging is simply the arithmetic mean of the three void fraction values. The void-reactivity given in Eq. (9.5) is calculated by evaluating the integral in Eq. (5.12).

10. CONCLUSIONS

In view of the importance of the nuclear-coupled flow/power instabilities in both conventional and next generation natural circulation BWR system, a detailed analytical modeling study has been carried out to derive the dimensionless groups. The physical processes namely, the fluid flow, fuel heat conduction, and neutron kinetics have been examined in a general two-phase flow systems such that the developed model can be applied to both forced and natural circulation systems.

The flow field formulation based on the one-dimensional drift-flux model has been performed by Ishii [12]. In the present study, the problem formulation given by Ishii has been extended by considering the subcooled boiling via Saha-Zuber [1]. The dimensionless groups that are important for the static and dynamics of the flow are rephrased in this study considering the time-dependent wall heat flux response.

The fuel heat conduction process has been examined for a typical BWR fuel pin consisting of the pellet, gap, and cladding regions. The detailed problem formulation has been performed and a simplified model based on dimensionless numbers are derived. It has been shown that the Fourier number defined by Eq. (4.58) is the most important dimensionless number. The Fourier number is the ratio of the heat transferred and the heat stored. Therefore, it demonstrated the measure of the time-lag due to diffusion of the heat throughout the fuel element. The artificial time-lag that is required to simulate the wall heat flux of a BWR fuel pin in the experimental facility can be determined based on the Fourier number scaling.

The model derived in Chapter 3 has been applied to flow excursion phenomenon in both forced and natural circulation system. It has been concluded that the subcooled boiling is a destabilizing effect. Neglecting the subcooled boiling gives non-conservative results in terms of the stability boundary.

A simple nonlinear dynamics model has been derived for the nuclear-coupled flow/power instabilities for the flow systems described in Chapter 3. The field equations for the fluid flow, fuel heat conduction, and neutron kinetics have been transformed into a set of coupled nonlinear ODEs by means of Galarkin Weighted Residual Method. The problem formulation has been kept general such that any degree of polynomial can be used to simulate the enthalpy wave propagation in the single phase heated section and void wave propagation in the two-phase mixture heated and unheated sections of a flow loop. A sample calculation for a single channel BWR core has demonstrated that limit-cycle oscillations are observed in the unstable region which is predicted via linear frequency domain tools. The model developed in this study can be used to understand the physics of the nonlinear DWO with or without nuclear feedbacks. Therefore, a detailed parametric study can be performed to investigate the effect of the void-reactivity coefficient, fuel heat conduction parameters such as flux depression factor, inlet subcooling, operating pressure/power, localized flow resistances etc.

Based on the detailed scaling study for each process (fluid flow, heat conduction, neutron kinetics), a strategy has been developed to simulate the void-reactivity feedback in the experimental facility introduced in Chapter 8. The nuclear-coupled flow instability experiments are still on-going. The detailed database considering the important parameters described in each process are being generated.

LIST OF REFERENCES

LIST OF REFERENCES

- [1] P. Saha. *Thermally Induced Flow Instabilities Including the Effect of Thermal Nonequilibrium between Phases*. PhD thesis, Georgia Institute of Technology, 1974.
- [2] J.A.Bouré, A.E. Bergles, and L.S. Tong. Review of two-phase flow instabilities. *Nucl. Eng. Des.*, 25:165–192, 1973.
- [3] L.S. Tong and Y.S. Tang. *Boiling Heat Transfer and Two-Phase Flow*. Taylor & Francis, 1997.
- [4] R.T. Lahey Jr. and D.A. Drew. An assessment of literature related to LWR instability modes. Technical report, Nuclear Regulatory Commission, 1980.
- [5] M. Ledinegg. Instability of flow during natural and forced circulation. *Die Warme*, 61(8), 1938.
- [6] J.S. Maulbetsch and P. Griffith. A study of system induced instabilities in forced convection flows with subcooled boiling. Technical Report 5382-35, M.I.T. Engineering Projects Lab Report, 1965.
- [7] M. Ishii and H.K. Fauske. Boiling and dryout behavior in a liquid-metal fast breeder reactor subassembly bundle under low heat flux and low flow conditions. *Nucl. Sci. Eng.*, 84:131–146, 1983.
- [8] R.P. Mathisen. Out of pile channel instability in the loop Skalv. In *Symp. on Two Phase Dynamics*, Eindhoven, Netherlands, 1967.
- [9] F.A. Jeglic and T.M. Grace. Onset of flow oscillations in forced flow subcooled boiling. Technical report, NASA-TN-D 2821, NASA Lewis Research Cntr.,Cleveland,OH, 1965.
- [10] M. Aritomi, T. Nakahasi, M. Wataru, J.H. Chiang, and M. Mori. Transient behavior of natural circulation for boiling two-phase flow experimental results. In *Trans. of the American Nuclear Society*, volume 62, pages 709–711, 1990.
- [11] M. Aritomi, J.H. Chiang, and M. Mori. Fundamental studies on safety-related thermal-hydraulics of natural circulation boiling parallel channel flow systems under startup conditions. *Nucl. Safety*, 33:170–172, 1992.
- [12] M. Ishii. *Flow Instabilities in Two-Phase Mixtures in Thermal Equilibrium*. PhD thesis, Georgia Institute of Technology, 1970.
- [13] M. Ishii. Study on flow instabilities in two-phase mixtures. Technical Report ANL-76-23, Argonne National Laboratory, 1976.

- [14] R.T. Lahey Jr. and F.J. Moody. *The Thermal Hydraulics of a Boiling Water Nuclear Reactor*. American Nuclear Society, second edition, 1993.
- [15] R.T. Lahey Jr. and M.Z. Podowski. *Multiphase Science and Technology*, volume 4, chapter On the Analysis of Various Instabilities in Two-Phase Flows. Hemisphere Publishing Corporation, 1989.
- [16] A.E. Bergles, P. Goldberg, and J.S. Maubetsch. Acoustic oscillations in a high pressure single channel boiling systems. In *Proc. Symp. on Two-Phase Flow Dynamics*, volume 6, pages 525–550. EURATOM Rep., 1967.
- [17] A.A. Bishop, R.O. Sandberg, and L.S. Tong. Forced convection heat transfer to water at near critical temperature and supercritical pressure. Technical Report WCAP-2056, USAEC, 1965.
- [18] A.H. Stenning and T.N. Veziroglu. Oscillations in two-component, two-phase flow. Technical Report CR-72121, NASA, 1967.
- [19] State of the art report on boiling water reactor stability. Technical Report NEA/CSNI/R(96)21, OECD/NEA, 1997.
- [20] J. M. Leuba and J. M. Rey. Coupled thermal-hydraulic and neutronic instabilities in boiling water reactors: A review of state of the art. *Nucl. Eng. Des.*, 145:97–111, 1993.
- [21] R.T. Lahey Jr. and G. Yadigaroglu. NUFREQ, a computer code to investigate thermo-hydraulic stability. Technical Report NEDO-13344, General Electric Company, 1973.
- [22] G.C. Park, M.Z. Podowski, M. Becker, and R.T. Lahey Jr. The development of closed form analytical model for the stability analysis of nuclear coupled density wave oscillations in boiling water reactors. *Nucl. Eng. Des.*, 92:253–281, 1986.
- [23] O. Yokomizo. Time Domain Analysis of BWR Core Stability. *J. Nucl. Sci. Technol.*, 99:41–51, 1987.
- [24] J.H. Chiang, M. Aritomi, R. Inoue, M. Mori and H. Tabata. Thermal-hydraulics during startup in natural circulation boiling water reactor. In *Proc. 5th Int. Topical Meeting on Reactor Thermal Hydraulics(NURETH-5)*, pages 119–126, 1992.
- [25] F. Inada, M. Fruya, and A. Yasuo. Thermohydraulic instability of boiling natural circulation loop induced by flashing (analytical consideration). *Nucl. Eng. Des.*, 200:187–199, 2000.
- [26] S.Y. Lee, M. Ishii. Thermally Induced Flow Oscillation in Vertical Two-phase Natural Circulation Loop. *Nucl. Eng. Des.*, 122:119–132, 1990.
- [27] I. Babelli. *Flow Instabilities under Low-Pressure and Low-Flow Conditions with Application to the Simplified Boiling Water Reactor*. PhD thesis, Purdue University, 1996.
- [28] J. Paniagua, U.S. Rohatgi, V. Prasad. Modeling of thermal hydraulic instabilities in single heated channel loop during startup transients. *Nucl. Eng. Des.*, 193:207–226, 1999.

- [29] P. Saha and N. Zuber. Point of net vapor generation and vapor void fraction in subcooled boiling. In *Proceedings 5th International Heat Transfer Conference*, pages 175–179, Tokyo, 1974.
- [30] Levy, S. Forced convection subcooled boiling–prediction of vapor volumetric fraction. *Int.J. Heat Mass Transfer*, 10, 1967.
- [31] N. Zuber. Flow excursion and oscillations in boiling, two-phase flow systems with heat addition. In *Proc. Symp. Two-Phase Flow Dynamics*, volume 1, page 1071, 1967.
- [32] M. Ishii. *Thermo-fluid Dynamic Theory of Two-Phase Flow*. Eyrols, Paris, Scientific and Medical Publication of France, 1975.
- [33] M. Ishii. One dimensional drift flux model and constitutive equations for relative motion between phases in various two-phase flow regimes. Technical Report ANL-77-47, Argonne National Laboratory, 1977.
- [34] S. Levy. Forced convection subcooled boiling–prediction of vapor volumetric fraction. Technical Report GEAP-5157, General Electric Company, 1966.
- [35] R.W. Bowring. Physical model based on bubble detachment and calculation of steam voidage in the subcooled boiling region of a heated channel. Technical Report Report HPR-10, OECD Halden Reactor Project, 1962.
- [36] P. Griffith, J.A. Clark, and W.M. Rohsenow. Void volumes in subcooled boiling systems. In *paper-58-HT-19*. American Society of Mechanical Engineers, 1958.
- [37] M.F. Lyons, D.H. Coplin, H. Hausner, B. Weidenbaum, and T.J. Pashos. UO₂ Powder and Pellet Thermal Conductivity during Irradiation. Technical Report GEAP-5001-1, General Electric Company, 1966.
- [38] N. Todreas, M.S. Kazimi. *Nuclear Systems I, Thermal Hydraulic Fundamentals*. Taylor and Francis, 1990.
- [39] L.S. Tong and J. Weisman. *Thermal Analysis of Pressurized Water Reactors*. American Nuclear Society, 1970.
- [40] A.M. Ross and R.L. Stoute. Heat Transfer Coefficient Between UO₂ and Zircaloy-2. Technical Report AECL-1152, Atomic Energy of Canada Limited, 1962.
- [41] R.T. Lahey, Jr. and F.J. Moody. *The Thermal Hydraulics of a Boiling Water Nuclear Reactor*. American Nuclear Society, second edition, 1993.
- [42] D.B. Scott. Physical and Mechanical Properties of Zircaloy-2 and Zircaloy-4. Technical Report WCAP-3269-41, Westinghouse Electric Company, 1965.
- [43] F.W. Dittus and L.M.K. Boelter. *Publications on Engineering*, volume 2. University of California, Berkeley, 1930.
- [44] W.H. Jens and P.A. Lottes. Analysis of Heat Transfer, Burnout, Pressure Drop and Density Data for High Pressure Water. Technical Report ANL-4627, Argonne National Laboratory, 1951.

- [45] J.R.S. Thom et.al. Boiling in Subcooled Water during Flow in Tubes and Annuli. In *Proc. Inst. Mech. Eng.*, page 180:226, 1966.
- [46] M. Ishii, S.T. Revankar, Y. Xu, H.J. Yoon, S. Kuran, L. Cheng, X. Sun, M. Lindsey, W. Wang. Thermal-Hydraulic Instability Study for Natural Circulation BWRs in PUMA Facility. Technical Report PU/NE-02-09(Quick-Look-Report), U.S. Nuclear Reagulatory Commission, September 2002.
- [47] F.D. Giust, R.J. Stamm'ler, A. A. Ferri. *HELIOS 1.7 User Guide and Manual*. Studsvik Scandpower, 2001.
- [48] K. Ott and R.J. Neuhold. *Introductory Nuclear Reactor Dynamics*. American Nuclear Society, La Grange Park, Illinois, USA, 1985.
- [49] J.J. Duderstadt and L.J. Hamilton. *Nuclear Reactor Analysis*. John Wiley, New York, 1976.
- [50] J. M. Leuba. Radial nodalization effects on BWR stability calculations. In *International Workshop in Boiling Water Reactor Stability*, pages 232–240. OECD Nuclear Energy Agency, October 1990.
- [51] G.F. Hewitt. *Measurement of Two-Phase Flow Parameters*. Academic Press, New York, 1978.
- [52] S.T. Revankar and M.Ishii. Local interfacial area measurement in bubbly flow. *Int. J. Heat and Mass Transfer*, 87:453–468, 1992.
- [53] N. Miller and R.E.Mitchie. Measurement of local voidage in liquid/gas two-phase flow systems using a universal probe. *J.Br. Nucl. Energy Soc.*, 9:94–100, 1970.
- [54] A.M.C. Chan and S. Banerjee. Design aspects of gamma densitometers for void fraction measurements in small scale two-phase flow. *Nucl. Instr. Meth.*, 190:135–148, 1981.
- [55] C.S. Eberle, W.H. Leung, M.Ishii and S.T. Revankar. Optimization of a one-shot gamma densitometer for measuring area-averaged void fractions of gas-liquid flows in narrow pipelines. *Meas. Sci. Technol.*, 5:1146–1158, 1994.
- [56] D.R. Oliver and A. Young Hoon. Two-phase non-newtonian flow. part-1: Pressure drop and hold-up. *Trans. Instn. Chem. Engrs.*, 46:106–115, 1968.
- [57] J.C. Maxwell. *A Treatise on Electricity and Magnetism*. Clarendon Press, Oxford, 1881.
- [58] M.W.E. Coney. The theory and application of conductance probes for the measurement of liquid film thickness in two-phase flow. *J. Phys. E. Scient. Instrum.*, 6:903–910, 1973.
- [59] P. Andreussi, A. Di Donfrancesco, M. Messina. An impedance method for the measurement of liquid hold-up in two-phase flow. *Int. J. Multiphase Flow*, 6:777–787, 1988.

APPENDIX A. SINGLE AND TWO-PHASE EULER NUMBERS

Integration of momentum equation based on steady-state solution for density and velocity field yields euler number, which is the ratio of pressure and inertial forces.

1. Single Phase Heated Region:

$$N_{Eu,h}^{1\phi} = \left[\frac{1}{2} K_i + \lambda^* \left(N_f + \frac{1}{N_{Fr}} \right) \right] \quad (A.1)$$

2. Two-Phase Mixture Heated Region:

$$\begin{aligned} N_{Eu,h}^{2\phi} = & \frac{K_e}{2} \frac{C_o C_r^*}{1 + C_r^*(C_o - 1)} + \frac{1}{N_{Zu}^2} \frac{C_r^* - 1}{1 + (C_o - 1)C_r^*} \\ & + \frac{1}{N_{Fr}} \left[\frac{C_o - 1}{C_o} (1 - \lambda^*) + \frac{C_o + N_d}{N_{Zu} C_o^2 C_g} \ln(C_r^*) \right] \\ & + C_m N_f \frac{1}{N_{Zu}} \frac{C_o + N_d}{C_g (C_o - 1)} \left[(C_r^* - 1) - \frac{1}{C_o - 1} \ln \left(\frac{1 + C_r^*(C_o - 1)}{C_o} \right) \right] \\ & + N_{Zu}^2 \frac{N_\rho C_o C_r^* (C_r^* - 1)}{[1 + C_r^*(C_o - 1)]^2} \bar{v}_{gj,e}^{*2} \end{aligned} \quad (A.2)$$

where

$$\bar{v}_{gj,e}^* = \frac{N_d}{N_{Zu}} + \frac{C_o - 1}{N_{Zu}} \left[1 + \frac{C_r^* - 1}{C_o} (C_o + N_d) \right] \quad (A.3)$$

3. Two-Phase Mixture Unheated Section: The euler number for unheated section or chimney section

$$\begin{aligned} N_{Eu,uh}^{2\phi} = & l_{uh}^* \left[\frac{1 + C_r^*(C_o - 1)}{C_o C_r^*} N_{Fr}^{-1} + \frac{C_m N_{f,uh}}{D_{e,uh}^*} A_{uh}^{*2} \frac{C_o C_r^*}{1 + C_r^*(C_o - 1)} \right] \\ & + \frac{K_{e,uh}}{2} \frac{1}{A_{uh}^{*2}} \frac{C_o C_r^*}{1 + C_r^*(C_o - 1)} \end{aligned} \quad (A.4)$$

The boiling boundary at steady-state conditions is written in dimensionless form by means of Saha-Zuber model,

$$\lambda^* = \frac{N_{sub}}{N_{Zu}} - \begin{cases} 0.0022 \frac{D_e^*}{\xi_h^*} \frac{1}{a_f^*} \frac{1}{N_{Zu}} & N_{Pe} < 70000 \\ 154 \frac{1}{A_h^*} & N_{Pe} > 70000 \end{cases} \quad (A.5)$$

Parameter C_r^* is the ratio of kinematic wave velocity at the heated section exit and boiling boundary, which is given by

$$C_r^* = 1 + \frac{N_{Zu} C_o C_g}{C_o + N_d} (1 - \lambda^*) \quad (A.6)$$

which is always greater than 1 if boiling starts in heated section.

APPENDIX B. BOILING BOUNDARY DYNAMICS EQUATIONS

Inserting Eq. (7.7) in to the single phase energy equation, the following equation for the residual can be obtained:

$$\mathbb{H}_{1\phi}N_s + 1 = \frac{dN_{sin}}{dt} + \sum_{i=1}^{N_1} \frac{dN_{si}}{z} + v_{fin}(t) \sum_{i=1}^{N_1} \frac{dN_{si}}{i} z^{i-1} + \Omega_{1\phi} \quad (\text{B.1})$$

The wighted functions are given as $1, z, \dots, z^{N_1-1}$. Therefore, N_1 equations can be determined by evaluating the integral Eq. (7.5) over $[0, \lambda(t)]$. In general, M^{th} equation can be written as follows:

$$\sum_{i=1}^{N_1} \frac{\lambda(t)^{i+M}}{i+M} \frac{dN_{si}}{dt} = -\frac{dN_{sin}}{dt} \frac{\lambda(t)^M}{M} - v_{fin}(t) \sum_{i=1}^{N_1} \frac{i}{i+M-1} \lambda(t)^{i+M-1} N_{si}(t) - \frac{\lambda(t)^M}{M} \quad (\text{B.2})$$

By using the boundary condition at $z = \lambda(t)$,

$$N_{sin}(t) + \sum_{i=1}^{N_1} N_{si}(t) \lambda(t)^i = 0 \quad (\text{B.3})$$

The differentiation of Eq. (B.3) respect to time gives the equation for the boiling boundary given by Eq. (7.10). Equation 7.10 together with the system of equation defined via Eq. (7.8) is solved to determine the boiling boundary dynamics and the single phase liquid enthalpy wave propagation.

APPENDIX C. PRESSURE DROP COMPONENTS

The integrating the second term on RHS of Eq. (3.56)) gives the pressure drop due to the convective acceleration. The integration can be modified via using the mixture continuity equation (Eq. (3.37)) as follows:

$$\int_0^{\theta_1} \rho_m v_m \frac{\partial v_m}{\partial z} d\theta = \rho_m v_m^2 \Big|_0^{\theta_1} + \int_0^{\theta_1} v_m \frac{\partial \rho_m}{\partial t} d\theta \quad (C.1)$$

Therefore, the pressure drop due to convective acceleration, $\Delta P_{sa}(t)$ is given as,

$$\begin{aligned} \Delta P_{sa}(t) = & \left(1 + \sum_{i=1}^{N_2} \rho_{mi}(t) \theta_1^i \right) (v_{fin}(t) + \Omega_{2\phi}(t) \theta_1(t))^2 - v_{fin}^2(t) \\ & + v_{fin}(t) \left(\sum_{i=1}^{N_2} \frac{\theta_1^{i+1}}{i+1} \rho_{mi}(t) - \frac{d\lambda}{dt} \sum_{i=1}^{N_2} \rho_{mi}(t) \theta_1^i \right) \\ & + \Omega_{2\phi}(t) \left(\sum_{i=1}^{N_2} \frac{\theta_1^{i+2}}{i+2} \rho_{mi}(t) - \frac{d\lambda}{dt} \sum_{i=1}^{N_2} \frac{i \theta_1^{i+1}}{i+1} \rho_{mi}(t) \right) \end{aligned} \quad (C.2)$$

The total frictional pressure drop in the channel is given as follows:

$$\begin{aligned} \Delta P_{fr}(t) = & N_f \left[v_{fin}^2(t) \left(1 + \sum_{i=1}^{N_2} \frac{\theta_1^{i+1}}{i+1} \rho_{mi}(t) \right) \right. \\ & + 2v_{fin}(t) \Omega_{2\phi}(t) \left(\frac{1}{2} \theta_1^2 + \sum_{i=1}^{N_2} \frac{\theta_1^{i+2}}{i+2} \rho_{mi}(t) \right) \\ & + \left. \Omega_{2\phi}^2(t) \left(\frac{1}{3} \theta_1^3 + \sum_{i=1}^{N_2} \frac{\theta_1^{i+3}}{i+3} \rho_{mi}(t) \right) \right] \\ & + \frac{N_{f,uh}}{A_{uh}} (v_{fin}(t) + \Omega_{2\phi} \theta_1)^2 \left(\rho_{me}(t) l_{uh} + \sum_{i=1}^{N_3} \frac{l_{uh}^{i+1}}{i+1} \rho_{m,uhi}(t) \right) \end{aligned} \quad (C.3)$$

The gravitational pressure drop can be simply obtained via the integration of

the density along the channel. It is given as,

$$\Delta P_{gr} = \frac{N_{Fr}^{-1}}{N_{Zu}^2} \left(1 + \sum_{i=1}^{N_2} \frac{\beta_1^{i+1}}{i+1} \rho_{mi}(t) + \rho_{me}(t) l_{uh} + \sum_{i=1}^{N_3} \frac{l_{uh}^{i+1}}{i+1} \rho_{m,uhi}(t) \right) \quad (C.4)$$

Finally, the pressure loss due to localized flow resistances, K_k , along the channel at locations, z_k , is given by the following equation,

$$\Delta P_{form} = \sum_{k \in 1\phi} \frac{1}{2} K_k v_{fin}^2(t) + \sum_{k \in 2\phi} \frac{1}{2} K_k \left(1 + \sum_{i=1}^{N_2} \rho_{mi}(t) \theta_k^i \right) (v_{fin}(t) + \Omega_{2\phi}(t) \theta_k)^2 \quad (C.5)$$

where $\theta_k = z_k - \lambda(t)$.